

Intact and Damaged DNA and their Interaction with DNA-Binding Proteins: a Single Molecule Approach

Dissertation

**For the award of the academic degree of
Doctor of Natural Science
From the faculty of Biology, Chemistry and Geosciences
University of Bayreuth**

submitted by
Marina Lysetska
born in Uzhgorod, UKRAINE

Bayreuth 2004

Die vorliegende Doktorarbeit wurde in der Zeit von November 1998 bis November 2003 am Lehrstuhl für Physikalische Chemie II der Universität Bayreuth unter der Betreuung von Herrn Prof. Dr. Georg Krausch angefertigt.

Der vorliegende Text ist ein vollständiger Abdruck der Dissertation, die von der Fakultät für Biologie, Chemie und Geowissenschaften der Universität Bayreuth genehmigt wurde.

Promotiongesuch eingereicht am:	17. März 2004
Tag des wissenschaftlichen Kolloquiums:	19. Juli 2004
Erster Gutachter:	Prof. Dr. G. Krausch
Zweiter Gutachter:	Prof. Dr. M. Sprinzl

Meinen Liebsten, Alex und Armin

'The search for truth is more precious than its possession'

-Albert Einstein-

CONTENT

CONTENT	I
LIST OF ABBREVIATIONS	IV
1 INTRODUCTION	1
1.1 STRUCTURE AND FUNCTION OF DNA	2
1.2 DNA DAMAGE	5
1.2.1 UV-Induced DNA damage	5
1.2.2 Cisplatin induced DNA damage	8
1.3 DNA REPAIR	9
1.3.1 Damage recognition in nucleotide excision repair	9
1.3.2 Replication protein A	12
1.3.3 Damage recognition by NER proteins studied with AFM	14
1.4 LEUZINE ZIPPER PROTEIN ORF80	15
1.5 PROBLEMS TO SOLVE IN THIS WORK	17
2 MATERIALS	19
2.1 CHEMICALS	19
2.2 BUFFERS	19
2.3 OLIGONUCLEOTIDES AND DSDNA FRAGMENTS	20
2.3.1 DNA fragments for FCS measurements	20
2.3.2 Intact DNA for AFM investigation	21
2.3.3 Plasmids and DNA ladder	23
2.3.4 DNA fragments that carry specific damage	23
2.4 PROTEINS	23
3 METHODS	25
3.1 BIOCHEMICAL METHODS	25
3.1.1 The hybridization of oligonucleotides	25
3.1.2 Amplification of the dsDNA using polymerase chain reaction	25
3.1.3 Purification of dsDNA on silica-gel particles	26
3.1.4 Determination of DNA concentration, yield and purity via using UV-spectroscopy	26
3.1.5 Radioactive labeling of dsDNA by enzymatic 5'-phosphorylisation with γ -[³² P]-ATP	26

3.2	ELECTROPHORETIC METHODS	27
3.2.1	Agarose gel electrophoresis	27
3.2.2	Polyacrylamide gel electrophoresis	27
3.2.3	Electrophoretic mobility shift assay	27
3.2.4	Detection of unlabeled DNA in gels	28
3.2.5	Detection of radioactive labeled DNA in gels	28
3.3	PREPARATION OF UV-LIGHT DAMAGED DNA	28
3.4	TAPPING MODE AFM IN FLUIDS	29
3.4.1	The principle of AFM TM in liquids	29
3.4.2	Image processing	30
3.4.3	Preparation of mica substrates for AFM measurements in liquids	30
3.5	FLUORESCENCE CORRELATION SPECTROSCOPY	32
3.5.1	The principle of FCS	32
3.5.2	Data evaluation	34
3.5.3	The fluorescent dyes used for labeling	35
4	RESULTS AND DISCUSSION	37
4.1	SURFACE-IMMOBILIZATION OF BIOMOLECULES FOR AFM INVESTIGATIONS IN LIQUIDS	37
4.1.1	Influence of Mg ²⁺ and Ni ²⁺ on DNA immobilization on mica	38
4.1.2	Dynamic investigations of the immobilization of DNA molecules	41
4.1.3	Molecular motions monitored by the time-resolved AFM imaging	44
4.1.4	Immobilization of plasmid DNA, proteins and DNA-protein complexes	48
4.1.5	Study of the influence of Ni ²⁺ , Na ⁺ and H ⁺ on the DNA hydrodynamic properties using FCS and FCCS	51
4.2	INVESTIGATION OF INTACT DNA MOLECULES USING AFM	59
4.2.1	Measurements of L _{DNA}	60
4.2.2	Determination of $\langle R^2 \rangle_{2D}$ and P _{DNA}	65
4.2.3	Structural peculiarities of intact DNA molecules	67
	4.2.3.1 <i>The heights of DNA molecules</i>	67
	4.2.3.2 <i>Double helix</i>	69
4.3	STRUCTURAL AND CONFORMATIONAL MODIFICATIONS INDUCED BY DIFFERENT TYPES OF DNA DAMAGE	71

4.3.1	UV-light damaged DNA	72
4.3.2	Bubble DNA	79
4.3.3	DNA molecules with a single cisplatin modification	81
4.3.4	DNA with a terminal tailed modification	82
4.3.5	Comparison of the conformational changes induced by different types of DNA damage	84
4.4	THE ROLE OF XPC-hHR23B AND HUMAN RPA IN THE INITIAL RECOGNITION OF DNA DAMAGE	87
4.4.1	XPC-hHR23B binding to bubble modified DNA	88
4.4.2	Complexes of hRPA with intact dsDNA	90
4.4.3	Interaction of hRPA with DNA containing a cisplatin adduct and a 6 nt bubble modification	91
4.4.4	Binding of hRPA to UV-light damaged DNA	92
	4.4.4.1 <i>EMSA investigations of hRPA-DNA complexes</i>	92
	4.4.4.2 <i>Human RPA interaction with UV-light damaged DNA studied with AFM</i>	94
	4.4.4.3 <i>Model of hRPA binding to intact and UV-light damaged DNA</i>	96
4.4.5	Phase imaging of biomolecules in liquids	98
4.5	A SINGLE MOLECULE APPROACH TO THE STUDY OF DNA-BINDING PROPERTIES OF ORF80	101
4.5.1	The binding of ORF80 to dsDNA studied with agarose gel electrophoresis	101
4.5.2	Investigation of the ORF80 DNA binding properties with AFM	102
	4.5.2.1 <i>ORF80 studied with AFM</i>	102
	4.5.2.2 <i>AFM investigation of ORF80-DNA complexes</i>	103
	4.5.2.3 <i>Specificity of the ORF80 binding to dsDNA</i>	106
	4.5.2.4 <i>Stoichiometry of the ORF80-DNA complexes</i>	107
4.5.3	FCS investigations of the ORF80 interactions with DNA	111
	4.5.3.1 <i>ORF80 binding to the 36 bp DNA containing a single TTAA-N₇-TTAA motif</i>	111
	4.5.3.2 <i>Unspecific binding of ORF80 to the ss- and dsDNA</i>	114
5	SUMMARY	117
6	ZUSAMMENFASSUNG	120
7	REFERENCES	124
	DANKSAGUNG	141

LIST OF ABBREVIATIONS

$\langle L_{DNA} \rangle$	mean contour length of DNA molecules
$\langle P_{DNA} \rangle$	mean persistence length of DNA molecules
$\langle R^2 \rangle_{2D}$	mean square end-to-end distance of DNA molecules
6-4 PP	pyrimidine(6-4) pyrimidone adduct
A	adenosine
A_{260}	absorption unit at 260 nm
A_{280}	absorption unit at 280 nm
A-DNA	right-handed DNA with a helix pitch of 2.3 nm
AFM	atomic force microscopy
AFM TM	TappingMode atomic force microscopy
APS	ammoniumperoxydisulfate
ATP	adenosine-5'-triphosphate
B-DNA	right-handed DNA with a helix pitch of 3.4 nm
bp	base pairs
BSA	bovine serum albumine
C	cytosine
Cisplatin, cis-DDP	<i>cis</i> -diaminedichloroplatinum
CPD	cyclobutane pyrimidine dimer
DBD	DNA binding domain
DNA	desoxyribonucleic acid
dNTP	mixture of oligonucleotides: dATP, dCTP, dGTP and dTTP
dsDNA	double stranded DNA
DTT	1,4-dithiothreitol
<i>E. coli</i>	<i>Escherichia coli</i>
EDTA	ethylenediaminetetraacetate
EMSA	electrophoretic mobility shift assay
FCCS	fluorescence cross correlation spectroscopy
FCS	fluorescence correlation spectroscopy
G	guanine
H ⁺	proton

List of abbreviations

HEPES	N ['] -(2-hydroxyethyl)piperazin-N ['] -(2-ethansulfoacid)
hHR23B	human homolog of the yeast Rad23B
hRPA, RPA	human replication protein A
K ⁺	potassium ion
kDa	kilo Dalton
L _{DNA}	apparent contour length of DNA molecules
Mg ²⁺	magnesium ion
Na ⁺	sodium ions
NER	nucleotidec excision repair
Ni ²⁺	nickel ions
NMR	nuclear magnetic resonance
nt	nucleotide
PAGE	polyacrilamid gel electrophoresis
PCR	polymerase chain reaction
P _{DNA}	persistence length of DNA molecule
pH	-lg[H ⁺]
rev	revolutions
RNA	ribonucleicacid
<i>S.islandicus</i>	<i>Sulfolobus islandicus</i>
ssDNA	single stranded DNA
T	thymine
TBE	tris borat EDTA
Tris	tris(hydroxymethyl)aminomethan
UV, UV-light	ultraviolet irradiation
UVA	ultraviolet light in the 320-400 nm range
UVB	ultraviolet light in the 290-320 nm range
UVC	ultraviolet light in the 220-290 nm range
v/v	volume fraction
w/v	weight fraction
XP	<i>Xeroderma pigmentosum</i>
XPA	<i>Xeroderma pigmentosun</i> protein A
XPC	<i>Xeroderma pigmentosun</i> protein C
Z-DNA	left-handed DNA with a helix pitch of 4.47 nm

1 INTRODUCTION

Understanding of life on its cellular and molecular level is tightly dependent on advances in the development of new techniques. With the invention of the first light microscope by van Leeuwenhoek in the 17th century it became possible to visualize single cells. From there on the technological progress and the invention of new methods steadily increased the resolution. Nowadays the structure of biomolecules can be observed with *nanometer* resolution.

The enormous experimental effort leads to the successful determination of 3-D structures of nucleic acids, proteins and their complexes. Nevertheless, the detailed knowledge of the *structure* of biological molecules does not provide the information about the *function* of such molecules. Resolving the molecular function demands the development of new techniques, which allow a precise physico-chemical characterization of elementary processes on the level of *individual* biomolecules, which are believed to be the smallest functional units in biological systems.

The structure-function relationship seems to be an important issue in the mechanism of DNA damage recognition by repair proteins (Gunz, 1996; Vassilyev, 1995). Recently, more and more experimental results suggest that repair proteins do *not* recognize chemical lesions *per se*, but structural distortions of the DNA double helix like bending (Husain, 1988; Oh, 1986), unwinding (Bellon, 1990) or unpaired regions (Buschta-Hedayat, 1999; Thoma, 2003; Vasquez, 2002) induced by changes in the bases chemistry. Moreover, different repair components recognize different types of DNA double helix distortion (Missura, 2001). However, the determination of the conformational changes of DNA molecule induced by different damage agents like e.g. UV-light or cisplatin as well as its complexes with repair proteins requires the application of rather sensitive techniques.

The introduction of atomic force microscopy, *AFM*; (Binnig, 1986) opened a possibility to study *single molecules* in ambient conditions avoiding fixation and any type of staining. The further demonstration of AFM operation in liquids (Marti, 1987) made AFM an important methodology for studying the biology of DNA (Bustamante, 1992; Hansma, 1992a; Hansma, 1992b), lipids (Dufrene, 2000; Hansma, 1991), polysaccharides (Abu-Lail, 2003), proteins (Muller, 2002; Thomson, 1999), DNA-protein complexes (Cary, 1997; Pang, 1997b; Schulz, 1998; Smulson, 1998; van Noort, 1999). Moreover AFM gives an unique possibility to *visualize* the dynamic biochemical processes on a single molecular level in *real space* (Bennink, 2003; Bustamante, 1999; Keller, 1998; Shimamoto, 1999). In spite of a number of significant advantages over other types of microscopes, AFM is still a surface technique and visualizes only

molecules *immobilized* on a solid support. The problem of immobilization of biomolecules onto a surface is very important and remains an Achilles' heel of the AFM (Rivetti, 1996).

Complementary to AFM, fluorescence correlation spectroscopy, *FCS* (Medina, 2002), is another *single molecule* technique and gives the unique possibility to trace hydrodynamic properties of single molecules in *bulk solution*. It was successfully applied for the analysis of *dynamic* biochemical processes (Kinjo, 1995; Schwille, 1996; Schwille, 1997a). However, in comparison to AFM it can trace only fluorescent labeled molecules. Due to the advances in solid-phase and enzymatic chemistry the labeling of DNA became relatively simple (Wojczewski, 1999). On the other hand, labeling of proteins with a fluorescence marker proved rather difficult and may affect their biochemical properties.

In this thesis I report about an analysis of the architecture of intact and damaged DNA molecules and its complexes with DNA-binding proteins using a *combination* of AFM and FCS. We developed *reproducible* protocols for the immobilization of *different* classes of biopolymers, - such as linear and circular DNA, different types of proteins and DNA-protein complexes, - for AFM visualization in liquids. The role of cations in the equilibration mechanisms of DNA molecules on a mica surface was studied using both AFM and FCS (4.1). The protocol for the immobilization of biomolecules in liquids was further applied to the structural analysis of *intact* DNA (4.2) and the conformational changes induced by different types of DNA *damage* (4.3). Thereafter we studied the architecture of the *complexes* of repair proteins with intact and damaged DNA (4.4) as well as the DNA-binding properties of the novel leuzine zipper protein ORF80 (4.5).

1.1 STRUCTURE AND FUNCTION OF DNA

Nucleic acids play an essential role in storage and transition of hereditary information from the mother to the daughter organism. Due to the importance of nucleic acids in biological research, they became a focus of interest in AFM imaging.

In April 1953 a short article in *Nature* reported on the structure of the nucleic double helix resolved by X-ray crystallography (Watson, 1953). Watson and Crick investigated DNA in its crystalline state and reported dimensions for the double helix that correspond to B-DNA. Double helical DNA consists of two sugar phosphate strands that wind around each other. The X-ray diffraction pattern indicates that the stacked bases are regularly spaced 0.34 nm apart along the helix axis. The helix makes a complete turn every 3.4 nm, thus there are about 10 base pairs per turn (Figure 1).

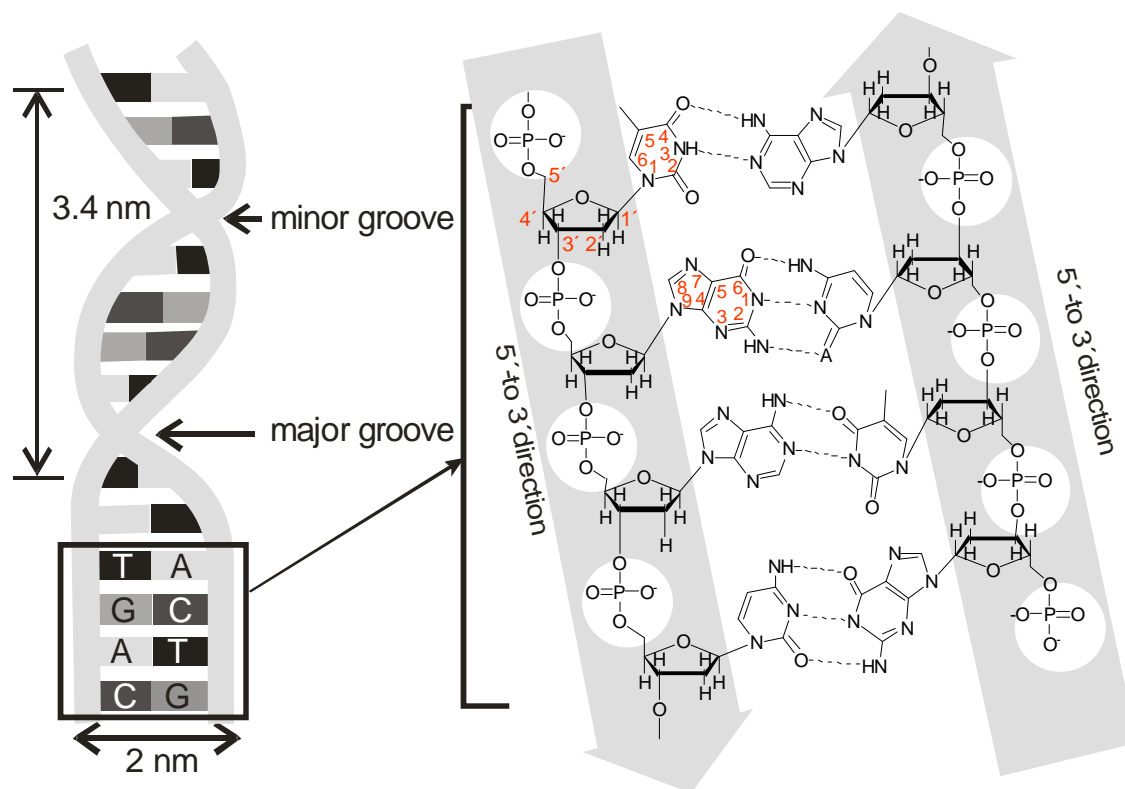


Figure 1. **Schematic structure of a double helix DNA.** The DNA fragment containing four common bases, together with the numbering schemes used for the purine and pyrimidine bases as well as for the ribose residue. The sugar component of a nucleotide is linked between the base and the phosphate group. The nucleotides are linked together by covalent phosphodiester bonds that join the 5' carbon of one group to the 3' carbon of the deoxyribose via a phosphate residue. This directionality has given rise to the convention that polynucleotide sequences are written and read in the 5'→3' direction. The purines - A and G - pair with the pyrimidines - C and T - via hydrogen bonds, which are indicated with dashed lines.

The base pairs are stacked in between the strands. They are held together by hydrogen bonds to the complementary base pairs on the antiparallel strands and by hydrophobic interaction to adjacent base pairs. The complementarity of A with T and C with G imposes a rule to the self-assembly of a DNA molecules. The bases are planar and form planar pairs. Additionally, the hydrophobic and van der Waals interactions between adjacent base pairs in the stack contribute significantly to the overall stability of the double helix. Due to its structure (Figure 1), the dsDNA molecule is no more flexible, but semi-flexible.

The visualization of DNA with AFM requires an immobilization of the molecules on a solid support. Efficient immobilization of the molecules for AFM investigations correlates with the resolution of AFM. An example of high resolution imaging of DNA in propanol (Hansma *et al.*, 1995) renders the pitch of the DNA double helix visible. The immobilization of DNA molecules in aqueous environment is more problematic, but also more challenging.

In water, the presence of negatively charged phosphate groups within the DNA results in a negative charge on its sugar phosphate backbone (Figure 1). It was proposed to use positively charged ions in order to immobilize DNA on a negatively charged mica surface (Bezanilla, 1995; Bustamante, 1992; Guthold, 1994). It has been shown that the values of the cationic radii and their concentrations influences the immobilization of DNA on the mica surface (Hansma, 1996a).

The AFM gives a possibility to size the DNA molecule, namely its apparent contour length and its end-to-end distance. Using those parameters a persistence length of the DNA molecule can be determined (Rivetti, 1996), that is commonly used to describe the global bending rigidity of polymers. For DNA molecules that are immobilized in 2-D it can be calculated using the following equation:

$$\langle R^2 \rangle_{2D} = 4P_{DNA}L_{DNA} \left(1 - \frac{2P_{DNA}}{L_{DNA}} \left(1 - e^{-\frac{L_{DNA}}{2P_{DNA}}} \right) \right) \quad (1),$$

where is $\langle R^2 \rangle_{2D}$ is the mean square end-to-end distance, P_{DNA} is the persistence length and L_{DNA} is an apparent contour length of the DNA molecules measured in the AFM images.

The analysis of the equilibration of DNA molecules on a surface from the AFM images has been the subject of a systematic study of Rivetti *et al.* (Rivetti, 1996). In their experiments they obtained a persistence length of 52.3 ± 0.3 nm that is in agreement with the 45 ± 15 nm obtained by ligase-catalyzed DNA cyclization method and the 53.4 ± 2.3 nm calculated by force spectroscopy (Bustamante, 1994; Taylor, 1990b). According to Rivetti *et al.* a reduction of the persistence length means trapping (Rivetti, 1996) of the molecules on the surface. However, in the experiments of Hansma *et al.* where nickel ions were applied for the immobilization of 500 bp DNA molecules onto a mica surface, a persistence length of 30 nm was measured (Hansma, 1996a). Note, that those molecules were found to move on the surface that reduced the quality of AFM imaging.

During the last decade AFM was often used for structure-function analysis. Pang *et al.* (Pang, 2000) demonstrated that a linear dsDNA poly d(A-T) fragment has an increased number of molecules with enlarged ends in comparison to linear poly d(G-C) dsDNA fragments, suggesting a terminal melting of pyrimidine rich regions of dsDNA. A statistical analysis of dsDNA molecules containing pyrimidine regions of varying length (Rivetti, 1998) demonstrates that the base sequence influences the dsDNA mechanics. An efficient immobilization of DNA on a lipid bilayer in aqueous environment allowed the visualization of the DNA double helix (Mou, 1995). In literature one finds additional studies about the influence of alkaline earth metal ions on the equilibration of DNA on a surface (Zheng, 2003), peculiarities of DNA immobilization on a cold

surface (Feng, 2000), the impact of the DNA sample drying (Sanchez-Sevilla, 2002), about conformational changes upon spermidine binding (Fang, 1998), observation of DNA G-wires (Marsh, 1995), etc.

1.2 DNA DAMAGE

Nucleic acids are rather compact (Figure 1) and stable molecules that can withstand a variety of external factors such as drying, low temperatures and a large variety of other environmental instabilities. However they are not fully inert and can be damaged by certain physical and chemical agents both from inside cells and from the environment. In fact, UV components of the sunlight and various chemical compounds introduce structural changes in the bases that affect the function of the DNA and subsequently may induce genetic mutations and cell death (Alberts, 2003; Berg, 1994; Ichihashi, 2003; Mitchell, 1989). Possible factors that can induce DNA modifications were and still are a high priority in molecular biological and biochemical research. In this chapter we provide a short overview on DNA damage types induced by UV-light and via interaction with cisplatin.

1.2.1 UV-Induced DNA damage

Direct adsorption of UV-light by the bases leads to the formation of the following types of DNA damage: cyclobutane pyrimidine dimers (Beukers, 1960; Setlov), pyrimidine (6-4) pyrimidone photoproducts (Lippke, 1981; Rycyna, 1985), 8,8-adenine dehydrodimers (Gasparro, 1986), purine photoproducts (Gallagher, 1989), and photoproducts at A-T sequences (Bose, 1984). The most abundant and best characterized are photolesions induced by UVC at 254 nm (close to the adsorption maximum of DNA): cyclobutane pyrimidine dimers (CPDs) and pyrimidine (6-4) pyrimidone photoproducts (6-4 PPs). They compose up to 95% of all DNA photolesions and are the major source of mutations and cancer (Bourre, 1987; Brash, 1988; Cleaver, 1988; Mitchell, 1989; Smith, 1993; Spivak, 1988). CPDs are the major photoproducts induced by UV light (~ 60% of all photoproducts), which can be split up into TT (Figure 2, A), TC/CT (Figure 2, B), and CC in the ratio 5:4:1 (Mitchell, 1992). The schematic structure of CPD is presented in Figure 2 A and B. As a result of UV-light irradiation two adjacent pyrimidines can produce a *cis-syn* cyclobutan thymine dimer (Figure 2, A) or a *cis-syn* cyclobutan thymine-cytosine dimer (Figure 2, B). Ultraviolet radiation affects the pyrimidines by activating the C₅-C₆ double-bond leading to its saturation and dimerization.

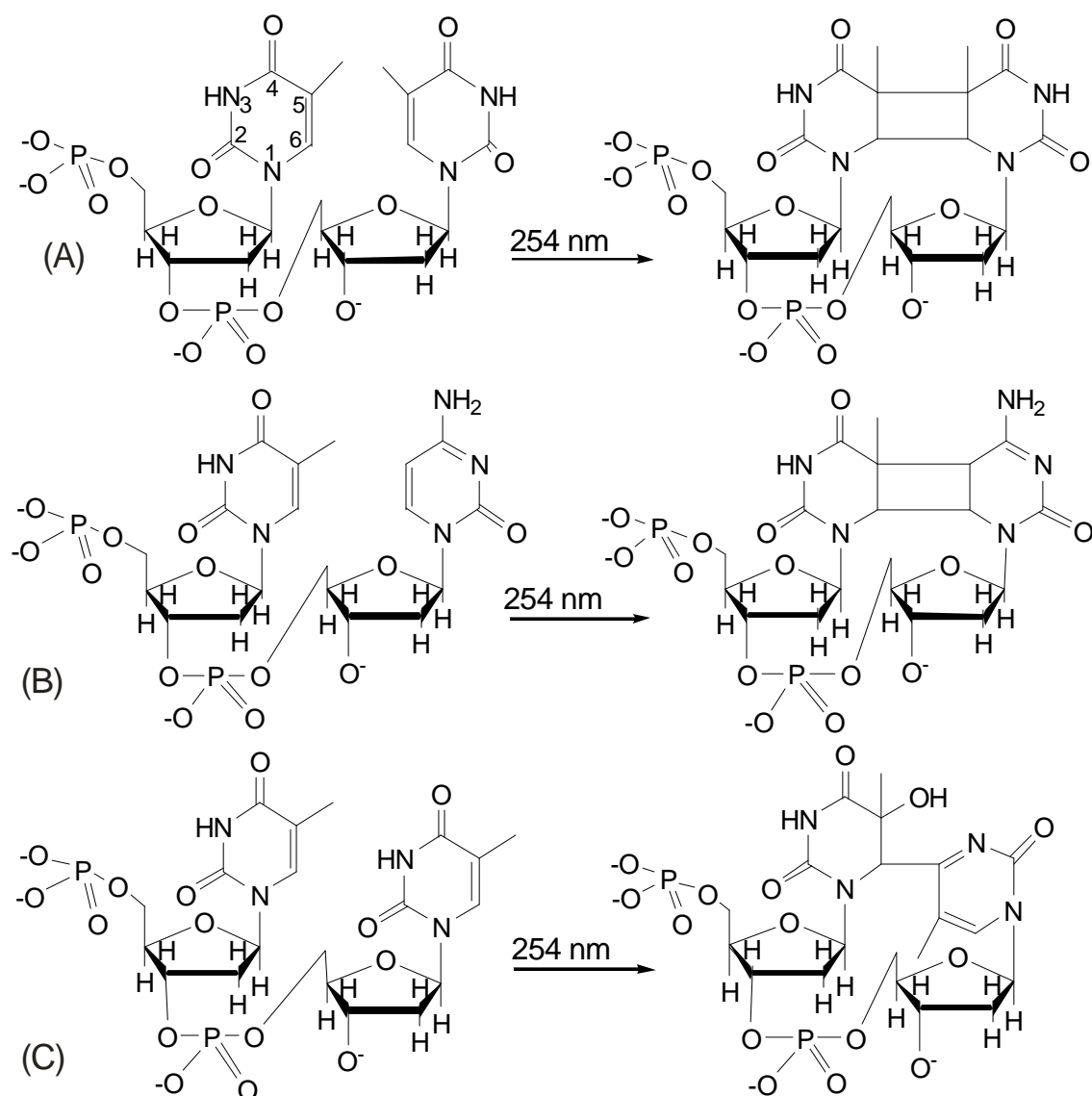


Figure 2. **Formation of the CPD and 6-4 PP as a consequence of UV-light irradiation.** Dimers can form between two adjacent pyrimidines: (A) thymine–thymine cyclobutane–pyrimidine dimer, (B) thymine–cytosine cyclobutane–pyrimidine dimer and (C) 6-4 PP (Sinha, 2002).

Similarly, 6-4 PPs are formed between the 5-prime 6 position and the 3-prime 4 position of two adjacent pyrimidines (Figure 2, C). 6-4 PP is known to have a higher ability to cause mutations than the CPD (Horsfall, 1994).

Both CPDs and 6-4 PPs induce a bend or kink of 7–9 degrees and 44 degrees, respectively (Kim, 1995b; Kim, 1995d; Wang, 1993). An electron microscopy study showed that the presence of repetitive thymine dimers introduces a bend of the DNA molecule (Husain, 1988). NMR measurements of solution state 6-4 PP (Kim, 1995b; Kim, 1995c) and fluorescence resonance energy transfer measurements in the presence of a single 6-4 PP on a DNA molecule (Mizukoshi, 2001) revealed a small unwinding of the dsDNA helix at the damage site.

The UV induced photodamages are distributed irregularly along the DNA chain. This phenomenon was first described by Benzer *et al.*, who observed hotspots and coldspots of mutagenesis (Benzer, 1961). At some sites of the DNA they arise very often, so called hot spots of mutagenesis, while at other sites, i.e. at cold spots of mutagenesis they never arise (Parris, 1994). It has been shown that the frequency of mutation is dependent on two parameters: the sequence of the DNA in the immediate vicinity of the photoproduct, and the flexibility of the DNA at the site of the photoproduct (Becker, 1989; Kim, 1995b; Taylor, 1990a). The origin of these effects is not quite clear.

It was also shown that exposition of nucleic acids to UV-light induces single strand breaks in the DNA molecule (Cadet, 1992). The appearance of ssDNA breaks could not be explained by direct UV-light absorption by the sugar phosphate moiety, because its maximum lies at a shorter wavelength range. The ssDNA and dsDNA breaks are a typical damage type caused by the shortwave UV component of sunlight (Chadwick, 1994; Murakami, 2000b; Pang, 1996; Pang, 1997a; Pang, 1997b). In many cases the mechanism of action of UV-light involves the generation of free radicals (Adam, 1999) that attack DNA and produce a variety of lesions, including sugar and base modifications, strand breaks, and cross-links (Cadet, 1992). One of the most important radicals is the hydroxyl radical (OH \cdot) not only because it is one of the most reactive species, but also due to its relative abundance. The hydroxyl radical is generated with radiation by the hydrolysis of water. The hydroxyl (OH \cdot) is a common radical linked to genetic mutation, aging, and DNA strand breakage (Scharffetter-Kochanek, 2000). Experiments about the UVC influence on the plasmid pUC19 showed that it results mostly in the presence of ssDNA breaks (Wirths, 1972). Note, that vacuum dried DNA samples were two to three times less sensitive to UVC irradiation (Wehner, 1995). That fact gives a hint to an indirect UV-light influence. Moreover, the liberation of free bases has been observed as a consequence of UV-light exposure, probably caused by labialization and rapture of the N-glycosidic bonds (Dodonova, 1993).

To the best of our knowled there have been no investigations so far about the structural peculiarities of long DNA molecules that carry multiple photodamages, neither by electron microscopy nor by AFM. The investigation of ssDNA revealed its appearance as a globular structure (Hansma, 1996b) in AFM images, suggesting intrastrand hydrogen bonding. Additionally, Rivetti *et al.* (Rivetti, 1998) performed an AFM study using an interesting DNA construct containing a single stranded region in the middle of the DNA molecule. They demonstrated that in AFM images the 'ssDNA domain' within a dsDNA chain also appeared as a globular feature usually combined with a distinct DNA bent in the middle. Murakami *et al.* demonstrated the presence of double strand breaks as a consequence of radiation damage and a transition from circular to linear DNA using AFM (Murakami, 2000a).

1.2.2 Cisplatin induced DNA damage

In 1969, Rosenberg *et al.* reported that cisplatin (Figure 3) was found to have an anti-tumor property (Rosenberg, 1969).

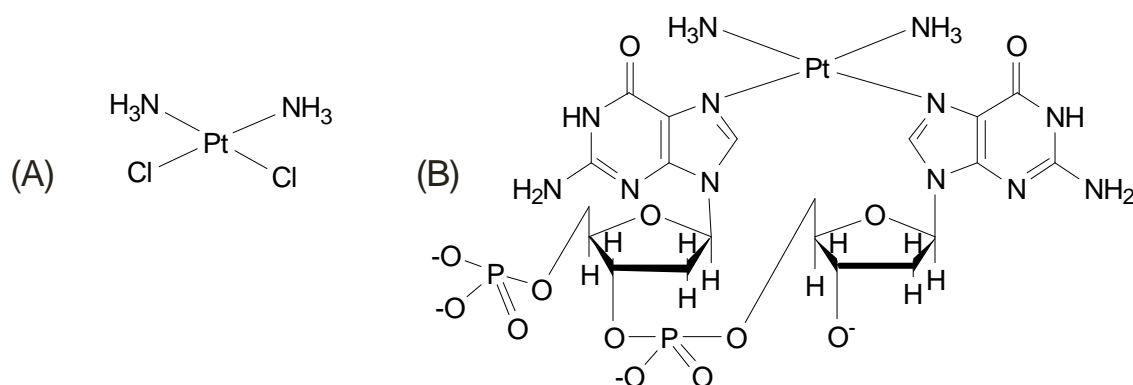


Figure 3. **Cisplatin and its binding to two adjacent purines.** The nucleotides are linked together by covalent bonds that join the 7' nitrogen of the purine base via a cisplatin residue to the 7' nitrogen atom of the next base, forming a d(GpG) cisplatin intrastrand crosslink.

After penetration into the cell the drug enters the low chloride medium of the cytoplasm and one or both chlorides are exchanged with water. Due to that transformation cisplatin becomes a reactive aqua species (Monjardet-Bas, 2003), that can react with DNA (Mansy, 1973), binding preferentially to the N₇ of the guanine base (Eastman, 1985; Fichtinger-Schepman, 1985). A schema of the intrastrand cisplatin binding to two adjacent purines is presented in Figure 3.

The d(GpG) intrastrand cisplatin crosslink appeared to account for 50-60% of bound platinum adducts (Fichtinger-Schepman, 1985). The distortions of the DNA double helix induced by the presence of a single intrastrand cisplatin adduct have been studied using several approaches (Malinge, 1999), including transmission electron microscopy studies (Revet, 1984) gel electrophoretical studies (Bellon, 1990), NMR (den Hartog, 1983; den Hartog, 1985; Gelasco, 1998; Huang, 1995; Kaspárková, 1996; Paquet, 1996), crystallographic studies (Coste, 1999; Takahara, 1995) and molecular dynamic simulation (Elizondo-Riojas, 2001). It has been shown that cisplatin binding to two N₇ atoms of adjacent purines causes local unwinding and bending of the dsDNA towards the major groove with a widening and flattening of the minor groove opposite to the cisplatin adduct. Already the presence of a single adduct leads to an overall helix bend angle between 55 and 81 degrees. However local base pairing around the adduct remains intact.

A few attempts of mapping the structural changes introduced by *multiple* cisplatin lesions have been performed with AFM. An investigation of dsDNA upon cisplatin

binding was performed using linear poly d(T-A) and poly d(G-C) fragments (Pang, 1996; Pang, 2000) and circular DNA molecules (Onoa, 1998; Onoa, 2002; Rampino, 1992). They both found significant conformational changes, shortening and compaction of the dsDNA as a consequence of *numerous* cisplatin lesions. The results obtained with AFM are in a good agreement with the similar studies performed using electron microscopy (Revet, 1984).

1.3 DNA REPAIR

DNA continuously undergoes different types of damage. It occurs during DNA replication and recombination or is induced by physical and chemical agents both from inside a cell and from the environment. To protect this Achilles heel, the cell has devised ingenious mechanisms for recognition and repairing the damage (Thoma, 2003). A failure of these mechanisms can lead to serious diseases, such as *Xeroderma pigmentosum*, hereditary nonpolyposis colon cancer, cocaine syndrome, cutaneous malignant melanoma and some forms of breast cancer. In addition to these specific diseases, it is considered that 80-90% of all human cancers may result, in part, from unrepaired DNA damage (Doll, 1981). Changes in the DNA lead to an altered double helix structure that is a target for the repair proteins. The most extensively studied and most important repair system removing the damage types introduced by UV-light and cisplatin is nucleotide excision repair.

1.3.1 Damage recognition in nucleotide excision repair

In the human cells nucleotide excision repair, *NER*, (Batty, 2000b; de Laat, 1999; Sancar, 1996; Wood, 1997) is the main pathway for removal of DNA lesions caused by UV light (1.2.1) and a variety of other bulky helix-distorting lesions caused by chemical mutagens, like cisplatin (1.2.2). *NER* is a complex process in which basically the following steps can be distinguished: 1) DNA damage recognition, 2) dual incisions of damaged DNA strand at sites some distance away from the lesion, 3) removal of the oligomer containing the DNA damage, and finally 4) filling up the gap using the intact opposite strand as a template with a subsequent ligation of a completely restored DNA sequence. The importance of *NER* in humans is clearly seen in patients with a rare genetic disease *Xeroderma pigmentosum*, *XP*, who have 1000-fold higher predisposition to skin cancer (Kraemer, 1989).

Although many details of *NER* have been elucidated, the mechanisms by which DNA damage is recognized remain to be fully determined (Thoma, 2003; You, 2003).

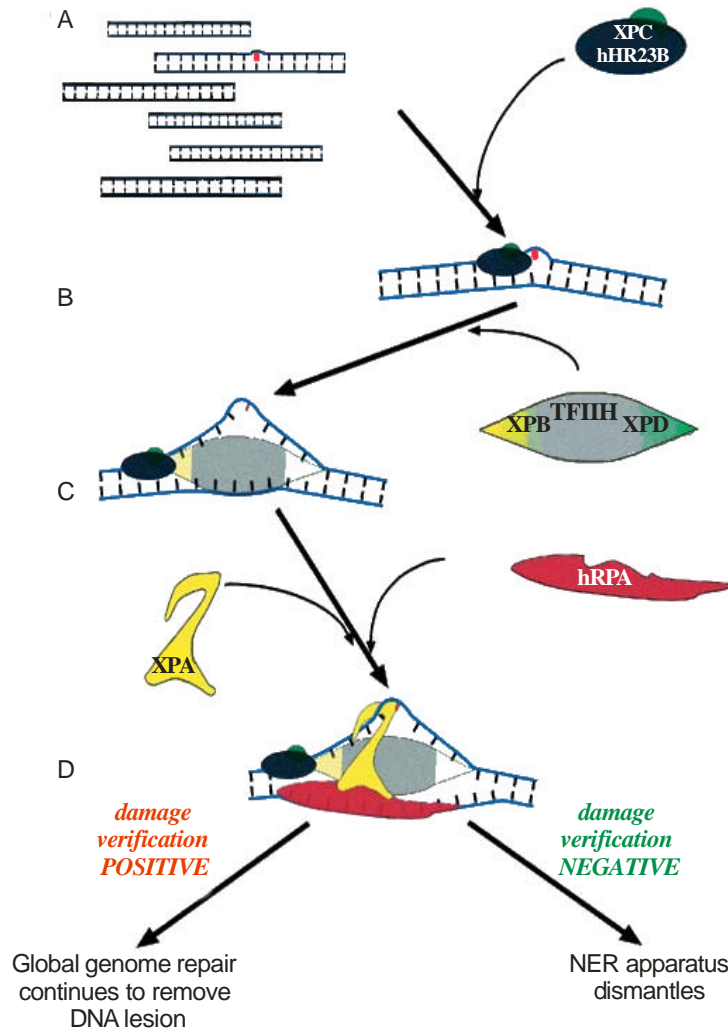


Figure 4. **Model for DNA damage recognition in the global genome repair subpathway of NER.** (A) A single region of DNA, among many unaltered DNA sequences, displays an alteration that is a departure from the normal Watson-Crick double helix (Figure 1). (B) XPC-hHR23B recognizes and binds to the region near the noncanonical DNA sequence. The interaction of XPC-hHR23B with the DNA at the 5[′]-double-stranded/single-stranded junction induces the formation of a rigid kink in the DNA helix. (C) TFIIH is recruited to the DNA by XPC-hHR23B and the TFII H-associated helicases XPB and XPD unwind the DNA duplex <10 nucleotides. The partially unwound DNA helix contains a rigidly kinked region around the DNA alteration and a single-stranded, flexible region on the complementary strand. (D) XPA and hRPA are recruited to the partially opened DNA helix and interact with the kinked and single-stranded portions of the DNA, respectively. Human RPA opens the DNA further and the presence or absence of DNA damage is verified by XPA. If DNA damage is present, then repair proceeds (red), or if XPC-hHR23B has identified an undamaged region of DNA, then the NER machinery will dismantle (Thoma, 2003).

The initial step of the damage recognition in NER is a rate-limiting step and involves certain proteins: XRA, hRPA, XPC-hHR23B and TFIIH (Batty, 2000b; Lee, 2000; Sancar, 1996; Wood, 2000).

It has been shown that each of these proteins shows an increased affinity to damaged DNA in comparison to undamaged DNA. The fact that NER proteins recognize a

variety of DNA lesions that do not share obvious chemical similarity suggests that they do not recognize chemical lesions *per se*, but structural distortions of the DNA double helix like bending (Husain, 1988), unwinding (Bellon, 1990) or unpaired regions (Buschta-Hedayat, 1999; Gunz, 1996; Thoma, 2003; Vasquez, 2002) induced by changes in the bases chemistry. Moreover, recent reports provide information that damage recognition in NER by repair proteins/protein-complexes occurs in an ordered, multistep fashion (Thoma, 2003; You, 2003). Figure 4 presents a model of the XPC-hHR23B and XPA-hRPA interplay in the damage recognition step in the global genome repair.

The human *Xeroderma pigmentosum A*, XPA, is a 40 kDa zinc-metalloprotein, an important member in NER that recognizes and removes a large variety of bulky dsDNA lesions. The XPA gene is absolutely required for both global genome repair and transcription coupled repair. It has been shown recently, that the rate of XPA binding to dsDNA lesions correlates to the rate of bends in the damaged DNA duplexes (Missura, 2001) and the degree of distortions in the DNA helical backbone (Vasquez, 2002). It has been shown that in human NER, XPA interacts with hRPA forming a tight protein-protein complex that may have a double check function for the verification of further NER processing (Li, 1994; Missura, 2001; Nocentini, 1997; Park, 1994). Note, that the XPA-hRPA complex demonstrates a greater affinity and specificity to damaged dsDNA in comparison to intact DNA (Lao, 2000).

The XPC-hHR23B is another important NER component that consists of a 106 kDa XPC protein associated with hHR23B, a 43 kDa homolog of the yeast Rad23B. XPC-hHR23B can discriminate between distorted DNA and a canonical Watson-Crick structure (Figure 1) (Kusumoto, 2001; Sugasawa, 1998; Sugasawa, 2001), although it shows only two to tenfold higher affinity to damaged DNA in comparison to intact DNA (Batty, 2000a; Hey, 2002b; Sugasawa, 1998; Sugasawa, 2001). However, recent experiments have shown that XPC-hHR23B can discriminate between intact and damaged DNA: its affinity to UV-light damaged DNA increased at least a factor of 10 when an undamaged DNA competitor was added (Sugasawa, 2001; Volker, 2001). Both *in vitro* and *in vivo* data suggest that XPC-hHR23B may be the first NER factor to respond to DNA damage in global genome repair (Sugasawa, 1998; Volker, 2001). Binding of XPC-hHR23B to DNA lesion induces further bending of the DNA (Janicijevic, 2003; Sugasawa, 1998), that may enhance the binding of other NER components, especially recruiting of TFIID (Drapkin, 1994), which is known to promote an opening of the DNA helix in the vicinity of a lesion.

The XPC-hHR23B is responsible for the initial damage recognition only in global genome repair, which is probably followed by a further binding of the XPA and hRPA complex to the XPC-DNA complex (Figure 4). It has been shown that XPC-hHR23B

has a higher affinity to damaged DNA in comparison to XPA-hRPA (Hey, 2002a; Thoma, 2003). Evans *et al.* and Sugasawa *et al.* proposed a hypothesis of recognition-verification interplay of the XPC-hHR23B with the XPA-hRPA complex, where XPC-hHR23B recognizes the damage, whereas XPA-RPA verifies the presence of a DNA lesion. Without verification by XPA-RPA, NER will not commence (Evans, 1997; Sugasawa, 1998). Recently it has been shown that initial damage recognition is realized by XPC complexed to hHR23B, which enhances the XPC binding to the DNA (You, 2003). The XPA-hRPA complex displaced the XPC-hHR23B on the DNA, suggesting a multi-step process of damage recognition.

Structural measurements of XPC-hHR23B binding to DNA have been already accomplished using AFM (Janicijevic, 2003). By direct sizing of a 812 bp dsDNA fragment containing a defined cholesterol lesion it was shown that XPC-hHR23B recognizes a single DNA lesion and causes a defined bend in the DNA as a result of the XPC-hHR23B DNA complex formation.

1.3.2 Replication protein A

The human replication protein A (RPA) is a single stranded DNA (ssDNA) binding protein that is a necessary factor in almost every form of human DNA metabolism, and RPA has emerged as a critical link between DNA damage repair and cell cycle control (Iftode, 1999; Wold, 1997).

The heterotrimeric RPA is highly conserved in all eukaryotes and contains subunits (Figure 5, A) that have been named according to their molecular mass as RPA70, RPA32 RPA14 and. The three-dimensional structure of all RPA subunits have been successfully solved with the help of NMR and x-ray crystallography (Bochkarev, 1997; Bochkarev, 2004; Bochkareva, 2002; Brill, 1998; Philipova, 1996). The presence of three ssDNA binding domains, DBD-A, DBD-B and DBD-C, have been identified on RPA70 (Figure 5, A). The role of the different DBD's in ssDNA recognition varies. An NMR chemical shift perturbation analysis showed, that DBD-A has a 5 to 10-fold higher affinity to ssDNA than the neighboring DBD-B (Arunkumar, 2003). However, a tandem binding of both DBD-AB showed a 100 fold higher affinity than the isolated domains. These findings support a sequential model of RPA binding to ssDNA in which DBD-A binds first to the majority of DNA and a subsequent participation of DBD-B is facilitated by the linkage effect.

The presence of a Zn binding motif located on the RPA 70 subunit (Figure 5, A) was found to be important for an efficient DNA binding (Bochkareva, 2000; Dong, 1999; Park, 1999). An additional ssDNA binding domain, DBD-D, was found on RPA 32 (Bochkarev, 1999; Bochkareva, 1998; Brill, 1998).

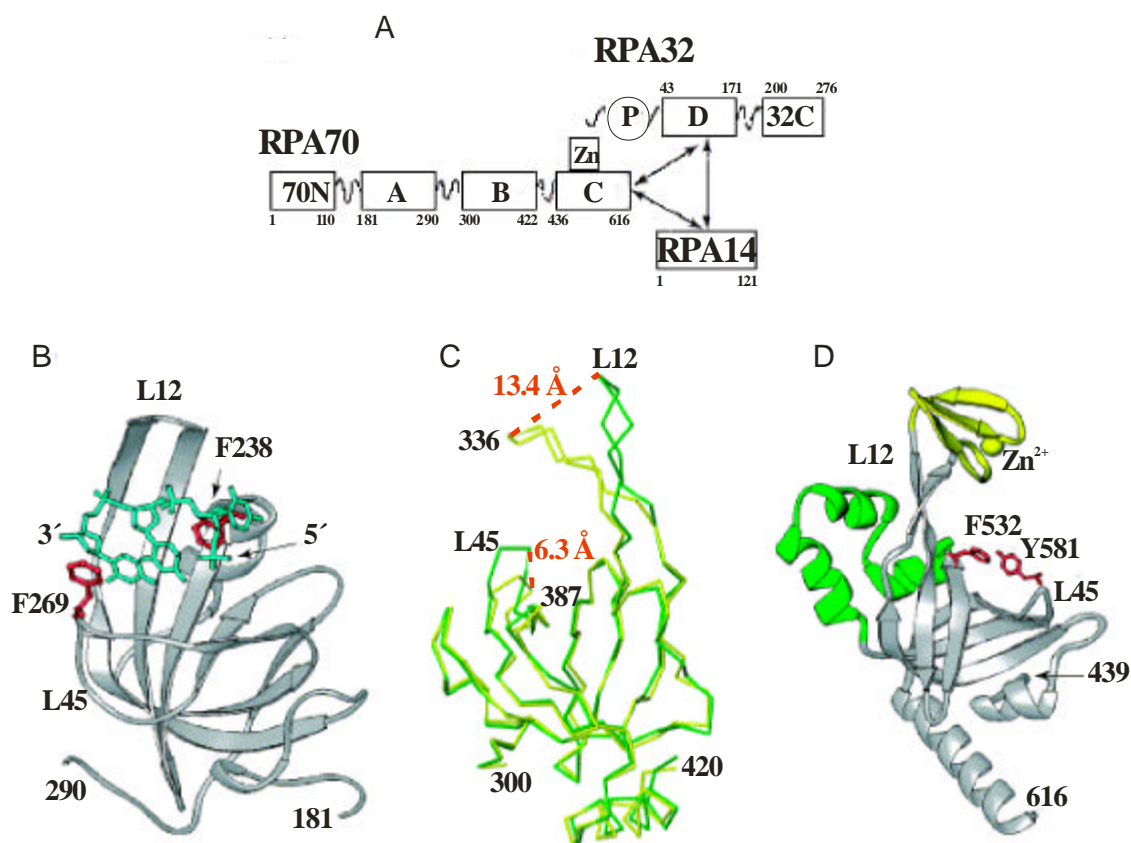


Figure 5. **Structural organization of hRPA subunits.** (A) Schematic showing the domain structure of hRPA. Domains are represented as boxes; their boundary residues are indicated. Zn, zinc ribbon; P, unstructured, phosphorylated N terminus of subunit hRPA32. (B) Structure of RPA70 DBD-A (ribbon diagram) bound to ssDNA. Two conserved aromatics are shown in red. (C) Flexible nature of the L12 and L45 loops; superposition of ssDNA-bound (yellow) and unbound (green) DBD-B. The maximal shifts of the L12 and L45 loops are indicated with dashed lines, and the size of the shift is indicated. (D) Structural inserts, zinc ribbon (yellow) and 3HB (green), in DBD-C (Bochkarev, 2004).

RPA binds tightly with high affinity and low cooperativity to ssDNA (Kim, 1994; Kim, 1995a; Mitsis, 1993; Schubert, 2003). Its apparent ssDNA association constant of 10^9 - 10^{11} M^{-1} is at least three orders of magnitude higher as the one to dsDNA (Kim, 1992; Kim, 1994). Moreover, it binds with a 50 to 100-fold higher affinity to polypyrimidine over polypurine sequences (Kim, 1992). Binding of a hRPA heterotrimer to ssDNA proceeds in three steps. Initial weak interaction occurs with the 8-10 nt (Blackwell, 1994) of the 5' end of ssDNA (Kolpashchikov, 2001). This initial binding is most likely mediated by an initial binding of DBD-A with a subsequent DBD-B linkage (Arunkumar, 2003). This is followed by an intermediate 13-14 nt binding step, and, finally, a more stable binding mode occurs, in which RPA covers about 30 nt (Kim, 1992; Kim, 1994; Lavrik, 1999) and all four DBDs are involved. As a consequence of the binding to the DNA hRPA undergoes conformational changes (Figure 5, C) that have been shown by biochemical methods (Gomes, 1996), transmission electron

microscopic (Blackwell, 1996) and NMR studies (Bochkareva, 2001). Such changes can be explained by the participation of hRPA timerisation core in DNA binding (Bochkareva, 2001; Bochkareva, 2002).

A transmission electron microscopy study of RPA binding to linear dsDNA showed that hRPA unwinds long regions of the dsDNA. The authors attribute that effect to the known affinity of hRPA for poly-A and poly-T homonucleotides (Eckerich, 2001; Treuner, 1996). They suggest an initial (preferential) binding of RPA to polypyrimidine rich ('breathing') regions in dsDNA and then induces separation of adjacent base pairs and an unwinding of the long dsDNA molecules. Moreover, an electron microscopy study also shows that hRPA does not bind at random sites, but preferentially at the dsDNA ends. At an equimolar ratio of DNA and protein only terminal binding of hRPA to linear dsDNA molecules was monitored only (Eckerich, 2001; Treuner, 1996).

A high affinity of hRPA to dsDNA lesions, such as UV photoproducts and cisplatin (1.2) *versus* undamaged DNA suggests that hRPA participates in the damage recognition step in NER (Burns, 1996; He, 1995; Hey, 2001; Lao, 2000; Patrick, 1999; Wakasugi, 1999; Wood, 1999). It was shown that the RPA32 subunit is phosphorylated (Figure 5, A) as consequence of UV-irradiation (Oakley, 2001). Since the chemical nature of a DNA lesions recognized by hRPA is diverse, it is believed that hRPA binds to unpaired regions created at the sites of DNA damage. Moreover, for the full opening around the lesion, NER requires hsRPA (Evans, 1997). The size of the fully opened repair intermediate is ~30 nt. Human RPA was also shown *in vitro* to be involved in the repair of dsDNA double strands breaks (Grandi, 2001; McIlwraith, 2000). Recently it has been shown that hRPA binds to intact ssDNA in the place of damage (Zou, 2003).

Additionally, hRPA is crucial for the coordination of NER proteins. Interactions were demonstrated with XPG ERCC1-XPF (Bessho, 1997; de Laat, 1998; He, 1995; Matsunaga, 1996), DNA polymerase (Braun, 1997), XPA (He, 1995; Matsuda, 1995) It had been shown that hRPA and XPA have a striking cooperativity in binding to dsDNA photolesions (Wang, 2000).

1.3.3 Damage recognition by NER proteins studied with AFM

In comparison to electron microscopy DNA-protein complexes can be imaged by AFM without application of contrast agents. This advantage of AFM makes this method suitable to study the DNA repair complexes with AFM. Additionally, visualization with AFM can be performed in liquids with varying salts conditions and DNA molecules of any arbitrary size can be used. Finally, in comparison with other single molecules visualization methods, AFM enables the visualization of the molecules 'at work' at almost physiological conditions.

The interaction of photolyase, the repair protein responsible for the light induced removal of photodamages on DNA, with intact dsDNA was studied by van Noort *et al.* (van Noort, 1998). A time-resolved AFM study revealed a protein sliding along the intact dsDNA chain. Such 1-D diffusion may indicate the mechanisms of localization of the DNA damage site. An AFM study of photolyase complexed with UV-light damaged DNA revealed a DNA bending of 36 degrees whereas no bending is observed in complexes with intact DNA (van Noort, 1999).

Analysis of the architecture of the damaged DNA with prokaryotic NER repair proteins was performed using electron microscopy (Shi, 1992) and atomic force microscopy (Verhoeven, 2001). Electron micrograph of the prokaryotic NER showed that UvrA binds to the UV-light damaged DNA with a high affinity and does not bend DNA. But in complexes with UvrB DNA was found to be severely kinked. Direct sizing of the DNA molecules from the AFM images of UvrB-DNA complex demonstrates that the bend derives from the wrapping of the DNA molecules around protein (Verhoeven, 2001). Additionally, AFM studies by Verhoeven *et al.* clarified the question of the stoichiometry of the repair in *E.coli*. Volume measurement from AFM images of DNA-UvrB complexes clearly indicated the presence of two UvrB promoters (Verhoeven, 2002). However, DNA was found to wrap around one promoter. Addition of the UvrC induces the release of one of UvrB promoters.

AFM have been successfully applied for the investigation of the elucidating of the details of the reactions of DNA containing single cholesterol lesion with XPC-hHR23B repair. Measurements of the apparent contour length from the AFM images revealed that XPC-hHR23B did not wrap DNA upon binding or damage recognition. It have been found that XPC-hHR23B binding to the damaged and intact DNA shows different bending of 39 and 49 degrees respectively (Janicijevic, 2003).

1.4 LEUZINE ZIPPER PROTEIN ORF80

Plasmid pRN 1 (Keeling, 1996) from the acidophilic thermophilic archaeon *S. islandicus* shares three highly conserved open reading frames with the others members of the plasmid family pRN1. One of the open reading frames, namely *ORF80*, encodes a 9.5 kDa protein that consists of 80 amino acids. Recombinant ORF80 has been first overexpressed in *E. coli* and characterized by Lipps *et al.* (Lipps, 2001).

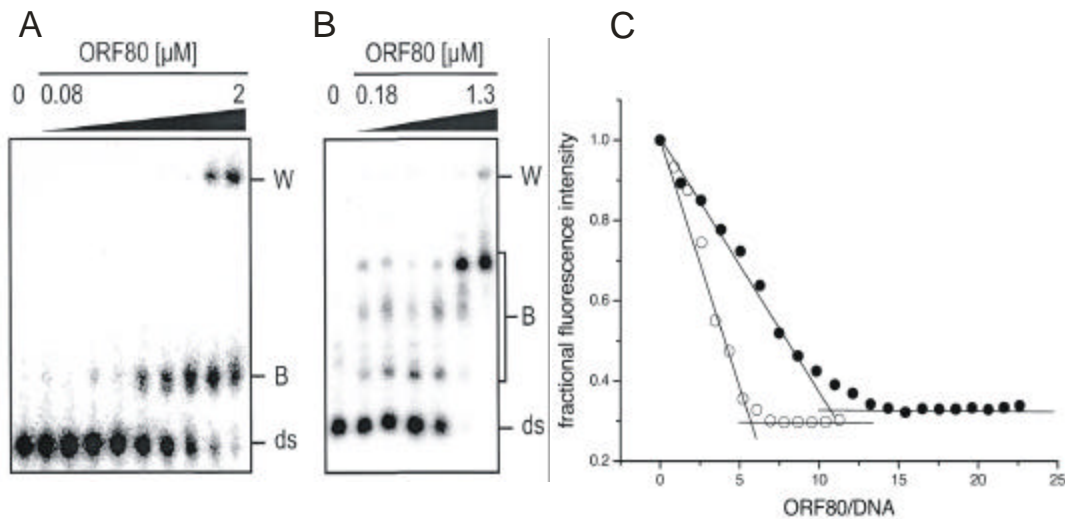


Figure 6. **Analysis of the ORF80 DNA binding properties.** (A) Binding to 31 bp DNA containing single binding site. The radioactive probe (5 nM) was incubated with 0, 0.08, 0.12, 0.18, 0.26, 0.40, 0.59, 0.89, 1.33 and 2 μ M ORF80. (B) Binding to a 149 bp DNA fragment containing both binding sites. The radioactive PCR fragment (\sim 5 nM) was probed with 0, 0.18, 0.26, 0.40, 0.59, 0.89 and 1.33 μ M ORF80]. **Ds** represents unbound double-stranded DNA, **B** is bound DNA and **W** stands for bound and aggregated DNA that remained in the wells of the gels. (C) Stoichiometric titration with 0.5 μ M Texas Red-labeled 36bp DNA (filled circles) and with 20bp DNA (open circles) that carry one full or half of the ORF80 binding site (Figure 7). Stoichiometric equivalence was reached at protein/DNA ratios of about 12 and 6, respectively (Lipps, 2001).

According to a footprinting and gel-shift analysis ORF80 specifically recognizes two consensus motifs TTAA-N₇-TTAA, that lies in upstream of its own gene and are separated by 60 base pairs (Figure 7). Both gel-shift experiments (Figure 6, A and B) and fluorescence titrations (Figure 6, C) show a distinct stoichiometry of the DNA-ORF80 complexes. According to Lipps *et al.* (Lipps, 2001) a single TTAA motif binds six ORF80 monomers (Figure 6). Besides its specific binding to the dsDNA, PAGE experiments demonstrate a high affinity of ORF80 to the ssDNA (Lipps, 2001).

The function of ORF80 in a cell is undefined yet. Since it forms a large protein-DNA complex ORF80 could have a specific structural role, i.e. forming a distinct structure which might be necessary to recruit the replication initiation machinery (Lipps, 2001).

1.5 PROBLEMS TO SOLVE IN THIS WORK

AFM provides an unique possibility to visualize single biomolecules that are immobilized on a solid support under near physiological conditions. Therefore our primary task was to develop a *reproducible* protocol of controlled immobilization of *different* types of biopolymers on a mica surface for AFM visualization in aqueous environment. We studied the influence of different components within the proposed AFM deposition buffer on the conformation of the DNA molecules by applying a combination of AFM and the complementary FCS. The growing interest of biologists to study the dynamics of the protein-DNA interaction with AFM (1.1) requires immobilization conditions where both DNA and protein molecules are not firmly fixed to a surface, but can diffuse in the surface plane. Therefore, our task was to optimize the immobilization conditions in order to suite such a requirement. The experimental results on this subject are presented in [chapter 4.1](#). The developed protocol of the immobilization of biomolecules on mica was used throughout this work.

An analysis of the conformation of intact DNA molecules was performed by utilizing high resolution AFM experiments as described in [chapter 4.2](#). Under investigation were intact DNA molecules of different lengths and under different preparation routines. These experiments were used as reference for measurements on DNA molecules that carry lesions.

The conformational changes of the DNA molecules induced by an altered chemistry of the DNA seem to be an important feature that attracts repair proteins (1.3). In [chapter 4.3](#) we report about the influence of different damage types , like a UV-light, a single cisplatin and a 6 nt bubble modification, - that are suggested to be subject for NER (1.3). There we report about the *first* morphological study of UV-light damaged DNA molecules. It demonstrates the peculiarities of the molecular architecture of long dsDNA molecules, which carry photoproducts at *random* sites. A possible explanation of the observed structures is discussed. Our AFM results are compared with those obtained by FCS and gel-electrophoretical measurements.

The knowledge of the conformation of intact (4.2) and damaged DNA molecules (4.3) in AFM images gives the possibility to analyze and compare the architecture of their complexes with repair proteins. In [chapter 4.4](#) we report about an AFM study of conformational analysis of intact and damaged DNA complexes with those proteins, which are responsible for the initial damage recognition in NER. There we report about the *first* AFM study of hRPA binding to DNA. A systematical analysis of the architecture of RPA complexes with intact and damaged DNA reveals peculiarities of their architecture and stoichiometry. A model of hRPA binding to DNA is proposed. Using the hRPA-DNA system we demonstrate that recording of a *phase image in*

liquids may provide important additional information to the AFM height image, especially when different types of biomolecules are under investigation.

In comparison to the repair proteins, ORF80 is a small protein with undefined physiological role (1.4). A footprint analysis showed a site-specific binding to dsDNA. The fluorescence titration and gel electrophoretical studies showed that ORF80 binds to dsDNA in distinct stoichiometries, requiring six or even twelve ORF80 monomers for a binding to a dsDNA fragment that carries one or two ORF80 binding motifs, respectively (1.4). In [chapter 4.5](#) we report about our experiments concerning the ‘puzzling’ DNA-binding behavior of ORF80 using a combination of AFM and FCS.

2 MATERIALS

2.1 CHEMICALS

Cy5	Amersham Pharmacia, Germany
Rodamin 6G	Lambda Physics, Germany
γ -[³² P]-ATP, 500 Ci/mmol	Hartmann, Braunschweig
Chlorotrimethylsilane	Fluka AG, Switzerland

2.2 BUFFERS

AFM deposition buffer*	10 mM HEPES·KOH pH 8.0, 2 mM KCl, 2 mM MgCl ₂
RPA/DNA binding buffer	25 mM HEPES·KOH pH 7.8, 100 mM KCl, 5 mM MgCl ₂ , 0.25 mM EDTA, 1 mM DTT, 0.01 % (v/v) Nonidet P40, 10% (v/v) glycerol
PAGE running buffer, TBE	90 mM Tris/boric acid, 1 mM EDTA, pH 8.3
Loading buffer for PAGE	20 mM EDTA, 0.2% (v/v) xylene cyanol, 0.2% (w/v) bromophenol blue in formamide
XPC assay buffer*	20 mM Tris·HCl pH 7.4, 2 mM MgCl ₂ , 50 mM NaCl, 1 mM DTT, 10% glycerol, 1 mM EDTA
XPC-dilution buffer*	25 mM HEPES·KOH pH 7.9, 1 mM DTT, 0.3 mM KCl, 0.2 μ g/ μ L BSA, 50% glycerol, 1 mM EDTA
DNA hybridization buffer*	buffer 4, New England Biolabs, Beverly, MA
FCS standard buffer*	20 mM Tris·HCl pH 7.5, 0.01% Tween 20, 100 mM KCl
Buffer pH 3	Citrate/hydrochloric acid (Merck, Germany)
Buffer pH 4	Citrate/hydrochloric acid (Merck, Germany)
Buffer pH 5	Citrate/sodium hydroxide (Merck, Germany)
Buffer pH 6	Citrate/sodium hydroxide (Merck, Germany)
Buffer pH 7	di-sodium hydrogen phosphate/potassium dihydrogenophosphate (Merck, Germany)
Buffer pH 8	Borate hydrochloric (Merck, Germany)
Buffer pH 9	Borate hydrochloric (Merck, Germany)

*solutions were prepared using Milli-Q ultra pure water (Millipore, USA) and were purified using 3 kDa centrifugal filters (Amicon Centriprep; Millipore Corp.) at 4000 rev/min. The purified solutions were stored at -20°C.

2.3 OLIGONUCLEOTIDES AND DSDNA FRAGMENTS

2.3.1 DNA fragments for FCS measurements

For FCS measurements oligonucleotides labeled on their 5'-ends were purchased from MWG-Biotech AG (Ebersberg, Germany). For the investigation of the ORF80/DNA binding properties oligonucleotides with different fluorescence labels (3.5.3, Table 2) were hybridized (3.1.1) with their complementary oligonucleotides in order to obtain double strand DNA with one or two fluorescent labels. The 36 bp fragments obtained contained either one full or no ORF80 binding site (Table 1).

N	Fluorophore	Sequence	Fluorophore
I	AlexaFluor488	5' -AAACAGTAT TTAATA AAAGCG TTAAT CCTACCTCCACC-3'	-
	-	3' -TTTGT CATAAATT ATTT CGCAATT AGGATGGAGGTGG-5'	Cy5.5
II	AlexaFluor488	5' -AAACAGTAT TTAATA AAAGCG TTAAT CCTACCTCCACC-3'	-
	-	3' -TTTGT CATAAATT ATTT CGCAATT AGGATGGAGGTGG-5'	-
III	-	5' -AAACAGTAT TTAATA AAAGCG TTAAT CCTACCTCCACC-3'	-
	-	3' -TTTGT CATAAATT ATTT CGCAATT AGGATGGAGGTGG-5'	Cy5.5
IV	Cy3	5' -AAACAGTAT TCGATA AAAGCG TACAT CCTACCTCCACC-3'	-
	-	3' -TTTGT CATAGCT ATTT CGCATGT AGGATGGAGGTGG-5'	Cy5.5
V	Cy3	5' -AAACAGTAT TCGATA AAAGCG TACAT CCTACCTCCACC-3'	-
	-	3' -TTTGT CATAGCT ATTT CGCATGT AGGATGGAGGTGG-5'	-
VI	-	5' -AAACAGTAT TCGATA AAAGCG TACAT CCTACCTCCACC-3'	-
	-	3' -TTTGT CATAGCT ATTT CGCATGT AGGATGGAGGTGG-5'	Cy5.5

Table 1. List of the sequences of the 36 bp DNA fragments that were used in FCS measurements. The bases in bold letters indicate sites of ORF80 binding. Bases in italic bold letters indicate modifications in the ORF80 binding site.

For the FCCS investigation of the unspecific binding of ORF80 to ssDNA we used a 1:1 mixture of the oligonucleotides of the same sequence:

5' -AAACAGTAT**TTAATA**AAAGCG**TTAAT**CCTACCTCCACC-3' either labeled with Alexa Fluor 488 or Cy5 on its 5'-end.

2.3.2 Intact DNA for AFM investigation

- 41_{Hybr} produced by R. Beinoraviciute-Kellner (LS Biochemie II, Universität Bayreuth) by hybridizing the following oligonucleotides:
5'-TAATGCATCATTCTATACTGTCATTCTGAACGAGGCGCGC-3'
3'-ATTACGTAGTAAGATATGCACAGTAAGACTTGCTCCGCGCG-5'
- 231_{ARS} prepared by R. Beinoraviciute-Kellner (LS Biochemie II, Universität Bayreuth) (Beinoraviciute-Kellner, 2002) by cutting pUC19-ARS16 (2.3.3) with a restriction enzyme XbaI from *S. cerevisiae* (Dank, 1997).
- 231 PCR fragment synthesized by R. Beinoraviciute-Kellner using pUC19-ARS16 plasmid as a template and the following oligonucleotides:
PCR_A: 5'-AGCGGAGGTGTGGAGACAAATGGTG-3' as a forward and
PCR_T: 5'-TTCCTGTACAATCAATCAAAAGCCAAATG-3' as a reverse primer (Beinoraviciute-Kellner, 2002)
- 368 PCR product was prepared by H. Dong (LS Biochemie II, Universität Bayreuth)
- 392 PCR product prepared by H. Dong (LS Biochemie II, Universität Bayreuth)
- 440_{Cy5} generated by PCR (3.1.2) using plasmid pUC-pRN1 (2.3.3) as a template (pos. 325-765 in Figure 7) and the following oligonucleotides
80footfor: 5'-cy5-CCACGAAATCACAAC-3' as forward primer and
p80footrev: 5'-GGTTGAGCTCGAGTCACAGGAGTTCGTCACGGC-3' as a reversed primer. The 440_{Cy5} DNA fragment was used for both for AFM and FCS experiments
- 538 generated by PCR (3.1.2) using plasmid pUC-pRN1 as a template (pos: 240-765 position in Figure 7) and the following primers:
bind.for: 5'-CGCCACTTGGCGAGAAATTTGCTCAAAG-3' as a forward primer and the same reversed primer (p80footrev) as for the 440_{Cy5} DNA fragment (Figure 7)
- 1060 generated by T. Hey (LS Biochemie, Universität Bayreuth) using pUC19 plasmid as template and the following oligonucleotides
5'-GCGCGTCAGCGGGTGTGGCGGG-3' as forward and
5'-GAGCGAACGACCTACACCGAACTG-3' as reversed primer

2 MATERIALS

```

-----bind.for----->
AAAATTCTCGCCACTTGGCGAGAAATTTGCTCAAAGTAGTGAAACAATATGAAAAAGAA
230 +-----+-----+-----+-----+-----+-----+----- 289

-----80footfor---->
AGAGAACAATCACAGATATGATTAAACTGCTGCATGCAGCCACGAAATCACAACATATGAT
290 +-----+-----+-----+-----+-----+-----+----- 349

TATGCAGTCCATATGTTAATCCTGGTCGGATCCGCAAATTTTAGTTATAAGAGTTAGCT
350 +-----+-----+-----+-----+-----+-----+----- 409

AACACGATAAGGCAAAACAGTATTAATAAAGCGTTAATCCTACCTCCACCGTGTATTATTAG
410 +-----+-----+-----+-----+-----+-----+----- 469

CTAACTTTTTGCACGCCAAAAGATATTTAACAGTCTGTTAATCCTACTTTACATGGGATC
470 +-----+-----+-----+-----+-----+-----+----- 529

CCATATGAGTGATCTGAAGGAAAAGCTAACTCTAACTCAACTAATCCTGATTCGGCTATC
530 +-----+-----+-----+-----+-----+-----+----- 589

AAAATCTTGTCAAACCCTGGAAGAGTTAGAACGATATACAGGTGCAAACAGAAATGTACT
590 +-----+-----+-----+-----+-----+-----+----- 649

TCTCGTTACCTTGACACGACTCCATAAAAAAGGCATAATCTACAGGAAATGGCGTAGGTT
650 +-----+-----+-----+-----+-----+-----+----- 709

<---p80footrev -----
TGCGGTAGGAAGTATAGAGAATATTGTTTGAAAAGCCGTGACGAACTCCTGTGAAACTC
710 +-----+-----+-----+-----+-----+-----+----- 769

CCCAGTTTACCGTTATTATTGATACATATCGATACATAATGATACATATGCACACATAAT
770 +-----+-----+-----+-----+-----+-----+----- 829

```

Figure 7. Details of the nucleotide sequence of the plasmid pUC-pRN1: position 230-829. The arrows mark the sequences of forward and reversed primers used for the amplification of the dsDNA fragments using PCR (3.1.2). Bold letters mark a 36 bp sequence that was used in FCCS measurements of the ORF80/DNA binding experiments. The ORF80 binding site is marked with italic letters.

2.3.3 Plasmids and DNA ladder

pUC19-ARS ₁₆	plasmid construct synthesized by Dank (Dank, 1997), which contains 16 ARS1 fragments and consists of 6392 bp
pUC-pRN1	plasmid from a pRN1 family (Keeling, 1996). Sequence of the position 230-829 is presented in Figure 7
DNA size marker	1kb-ladder (Gibco, Eggenstein)

2.3.4 DNA fragments that carry specific damage

1000 _{bubble}	1000 bp DNA fragment, which carries a single 6 nt mismatch modification prepared and purified by T. Hey (Hey, 2002a). The mismatch site lays asymmetrically (~30% of the DNA contour length from the DNA end)
368 _{cis-DDP}	368 bp dsDNA fragment, which carries a single platinated site prepared by H. Dong (LS Biochemie, Universität Bayreuth)
392 _{cis-DDP}	392 bp dsDNA fragment, which carries a single platinated site prepared by H. Dong (LS Biochemie, Universität Bayreuth)
274 _{85-tail}	274 bp dsDNA fragment with an unpaired 85 nt region on one end was produced by H. Dong (LS Biochemie, Universität Bayreuth).

2.4 PROTEINS

XPA	overexpressed in <i>E.coli</i> and purified by H. Dong (LS Biochemie, Universität Bayreuth)
XPC-hHR23B	generous gift from the lab of Prof. K. Sugasawa and F. Hanaoka (Japan)
hRPA	overexpressed in <i>E.coli</i> and purified by T. Hey (Hey, 2002a)
ORF80	overexpressed in <i>E. coli</i> and purified by G. Lipps <i>et al.</i> (Lipps, 2001)

3 METHODS

3.1 BIOCHEMICAL METHODS

3.1.1 The hybridization of oligonucleotides

For AFM and FCS measurements short dsDNA fragments were produced via hybridization of synthetic oligonucleotides. 1:1 mixtures of complementary oligonucleotides in a hybridization buffer (2.2) were annealed in a Personal Cyclor (Whatman Biometra, Göttingen) using the following temperature profile: 2 min at 95°C, 6 min at 65°C, followed by cooling to 25°C at 1.2°C/min.

For the FCS measurements we used oligonucleotides that carry fluorescence labels (Table 1). For the preparation of the dsDNA fragments with one fluorescence label a complementary unlabeled strand was added in a slight excess (10%). In order to avoid bleaching of the fluorophores, hybridization of the nucleotides that carry fluorescent labels was accomplished without the first denaturation step at 95°C.

3.1.2 Amplification of the dsDNA using polymerase chain reaction

A polymerase chain reaction, *PCR*, was used for a synthesis of long dsDNA fragments. The reaction components were mixed to the following final concentrations: 1 µM of both forward and reversed primers, 0.2 mM of dNTPs, 5 ng of the template DNA, 2 U/100 µL DNA polymerase in a reaction buffer containing 2.5 mM of Mg²⁺ and 1 mg/mL of BSA. Amplification of the DNA was performed using a Personal Cyclor (Whatman Biometra, Göttingen). The mixture is heated for 5 minutes to 95°C to separate the strands of the double-stranded template DNA containing the target sequence. Then it is cooled down to the primer-specific temperature of 55°C for 20 seconds, which allows the primers to recognize and bind to their complementary sequences on the separated strands. A subsequent increase of the temperature to the enzyme-specific temperature of 72°C for 30 seconds stimulates DNA polymerase to extend the primers into new complementary strands. Repeated heating and cooling cycles multiply the target DNA exponentially, since each new dsDNA fragment becomes a template for further synthesis and so on. After 30 cycles the reaction mixture was cooled down to 4°C. A purification of the PCR dsDNA fragments from proteins, template DNA, residual bases and primers was accomplished by adsorption of the dsDNA onto silica-gel particles (3.1.3). The purity of the PCR products was checked by

agarose gel electrophoresis (3.2.1) with a subsequent ethidiumbromide staining (3.2.4). Concentration of the PCR fragment was determined by UV-spectroscopy (3.1.4).

3.1.3 Purification of dsDNA on silica-gel particles

Double stranded DNA fragments generated by PCR were subsequently purified using a spin-column technology (MinElute PRC Purification Kit, Qiagen). During the dsDNA deposition step, unwanted primers and impurities, such as salts, enzymes, unincorporated nucleotides, unused primers and dyes do not bind to the silica membrane, but flow through the column. After removal of the contaminants, the dsDNA was collected from the membrane using a provided elution buffer that was additionally purified with 3 kDa centrifugal filters (Amicon Centriprep; Millipore Corp.) at 4000 rev/min. Alternatively, for the elution of the purified dsDNA we also used AFM deposition buffer (2.2).

3.1.4 Determination of DNA concentration, yield and purity via using UV-spectroscopy

The yield of a PCR product was determined by measuring the concentration of DNA by its absorbance at 260 nm using a Beckman DU 640 Spectrophotometer. Absorption at 260 nm, A_{260} , of 1 has been assumed to correspond to a DNA concentration of 50 $\mu\text{g}/\text{mL}$. Water should be used as reference when measuring DNA concentrations, since the relationship between absorbance and concentration is based on extinction coefficients calculated for nucleic acids in water. Additionally, the measurement of the absorbance in the range of 220-330 nm may indicate the presence of an additional contamination. The ratio of the absorbance at 260 nm and 280 nm (A_{260}/A_{280}) provides an estimation of the DNA purity with respect to contaminants that absorb UV-light.

3.1.5 Radioactive labeling of dsDNA by enzymatic 5'-phosphorylation with γ -[^{32}P]-ATP

The purified 538 bp fragment was labeled at its 5'-ends using T4 polynucleotide kinase (PNK) (Fermentas, St. Leon Rot) and γ -[^{32}P]-ATP (5000 Ci/mmol; Hartmann Analytics, Braunschweig, Germany). For this 3 μL of 538 bp PCR fragment (3.1.2) at a concentration of 340 nM, 1 μL of PNK 10x buffer, 0.5 μL of PNK enzyme (5 units) and 0.5 μL γ -[^{32}P]-ATP (10 units/mL) 10 $\mu\text{Ci}/\mu\text{L}$ were mixed together. The final volume was adjusted with ddH₂O to 10 μL and incubated for 30 min at 37°C. Before purification 90 μL of the TE binding buffer (MinElute PRC Purification Kit, Qiagen) was added to the 10 μL of the labeling mixture and purified as described in 3.1.3. The

yield of the enzymatic 5'-phosphorylation reaction was checked using 4% denaturing PAGE (3.2.2).

3.2 ELECTROPHORETIC METHODS

3.2.1 Agarose gel electrophoresis

To check the efficiency of the PCR and to investigate the ORF80 binding properties to the 538 bp DNA fragment we used 1% agarose gel electrophoresis. For the preparation of 100 mL of a 1% agarose solution, 1 g agarose was added to 100 mL 1x TBE (2.2) and microwaved until the agarose was dissolved and the solution became clear. After cooling to about 55°C the solution was poured into a form (15x10x0.5cm) and solidified for about 20 minutes at room temperature. To run a gel it was placed in an electrophoretic chamber and covered (just until the wells are submerged) with electrophoresis buffer (the same buffer as for the agarose preparation). Together with standard DNA the samples were loaded into the gels and exposed to 65 mA in 0.5xTBE- buffer for approximately 20 minutes. The detection was performed as described in 3.2.4.

3.2.2 Polyacrylamide gel electrophoresis

To analyse the DNA mobility in a constant electric field we used 4% or 8% polyacrylamide gel electrophoresis, *PAGE*. For the preparation of 40 mL gel we took 8 mL/ 4 ml of acrylamid and adjusted the volume to 80 or 40 mL, subsequently added 40/20 µL of tetramethylthyamid and 120/60 µL of ammoniumpersulfate. After at least one hour of polymerization, a denaturing loading buffer was loaded into the loading pockets and electrophoresed for 15 min at 4°C and 30 mA. Electrophoresis of the DNA probes was performed for 2-4 hours at 4°C at 40 mA. As a dsDNA size standard we used a 5'-labeled DNA ladder (2.3.3). Detection of the dsDNA lanes was performed by using autoradiographs (3.2.5) or ethidiumbromide staining (3.2.4).

3.2.3 Electrophoretic mobility shift assay

To verify a complex formation between hRPA and dsDNA prior and after UV-light exposition an electrophoretic mobility shift assay, *EMSA*, have been applied. 1 ng aliquots of intact and UV-light damaged (3.3) 538 bp (2.3.2) radioactive labelled DNA (3.1.5) were preincubated with the indicated amounts of hRPA in 10 µL of hRPA buffer (2.2) for 10 minutes at room temperature. Samples were loaded on native polyacrylamide gels (3.2.2) after addition of loading buffer either following fixation of the complexes by a 5 min incubation with 0.1% (w/v) glutaraldehyde or without further

treatment of the sample. Electrophoresis was carried out in 0.5xTBE (2.2) as running buffer for 3 hours at 10 V/cm and 4°C. The gels were analyzed by electronic autography (3.2.4)

3.2.4 Detection of unlabeled DNA in gels

The detection of the DNA in PAGE (3.2.2) and agarose gels (3.2.1) was performed by ethidiumbromide staining (at a concentration of 5 µg/mL), which makes DNA visible to UV light at 312 nm. The gels were submerged in ethidiumbromide solution for 10 min, rinsed in ddH₂O water and visualized using a UV-Transilluminator (Bioblock Scientific, Illrich).

3.2.5 Detection of radioactive labeled DNA in gels

The gels were analyzed by electronic autoradiography using an Instant Imager (Canberra Packard).

3.3 PREPARATION OF UV-LIGHT DAMAGED DNA

DNA molecules that contain UV-light damage sites were prepared by exposition of purified, 30 nM DNA solutions in AFM buffer to four germicidal lamps (G8T5, 15W, Sankyo, Japan) at 254 nm. DNA solutions were always kept on ice and at the same distance of approximately 10 cm from the UV-light source. Exposition of the DNA solution in a quartz cuvette was performed in a start volume of 200 µL and each time after a certain UV-light exposition 30 µL of the DNA solution were removed using a Hamilton microliter syringe (Bonadus, Switzerland).

Alternatively, the DNA solutions were exposed to UV-light in a row of UV-resistant Eppendorf tubes with opened lids. Each tube contained 30 µL of DNA solution. After fixed intervals of UV-light exposition time the Eppendorf tubes with the DNA solutions were removed one after another from the UV-light source.

3.4 TAPPING MODE AFM IN FLUIDS

3.4.1 The principle of AFMTM in liquids

The principle of tapping mode AFM in liquids is the same as in air (Knoll, 2003). An oscillating sharp tip mounted to a flexible cantilever tracks the surface of the sample (Figure 8). The cantilever is excited to its resonance oscillation frequency with a piezoelectric driver. The deflection of the cantilever is detected with very high sensitivity by a four-segmented photodiode. The oscillation amplitude is used as a feedback signal that enables the piezoelectric scanner to keep the tip at a constant interaction. The AFM controller supplies the signal for the spatial movement of a piezoelectric positioner with sub-nanometer accuracy resulting in a precise tracking of the sample by AFM scanning tip (Binnig, 1986).

There are advantages to operate AFM with the sample and cantilever immersed in a fluid. To begin with, it fully eliminates impact of the capillary forces and reduces Van der Waals' forces (Hartmann, 1991; Israelachvili, 1997; Weisenhorn, 1989) . For this reason it enables the application of very soft cantilevers with a spring constant of typically 0.1 N/m (compared to tapping mode in air where the cantilevers in the range of 1-100 N/m are used). In our experiments we used oxide sharpened tips with a spring constant of ~0.3 N/m. The cantilevers were purchased from NanoProbesTM (Digital Instruments, Inc., Santa Barbara, CA).

An important disadvantage of AFM operation in liquids is the difficulty of a direct excitation of the cantilever. The piezo is attached to the liquid cell which causes an oscillation of the entire fluid cell in order to couple the oscillation to the cantilever. This is different from the tapping or non-contact operation in air or vacuum where the cantilever is directly attached to the piezoelectric driver. Since the whole cell vibrates, resonances of the entire setup are excited and transduced to the cantilever, which results in the detection of multiple peaks, often referred to as 'forest of peaks'. In order to find the actual resonance peak of the cantilever, we analysed the Fourier transform of its thermal noise spectrum approximately 1 mm above the surface, which shows a distinct peak at the cantilever's resonant frequency. Subsequently the drive frequency was set to the resonance frequency and the phase zero was adjusted approximately 20 nm above the surface.

On the other hand, imaging in a fluid medium damps the cantilever's oscillation. In our experiments the drive frequencies ranged from 3.4 to 34 kHz. When an appropriate frequency is selected, the amplitude of the cantilever decreases when the tip begins to tap the sample, similar to TappingMode operation in air.

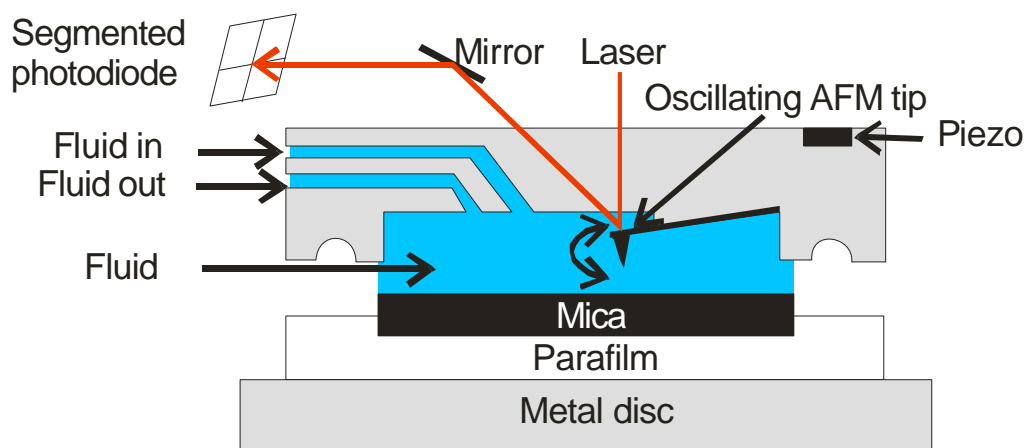


Figure 8. **Schema of the MultiMode fluid cell.** The cantilever is fixed to the fluid cell with the help of a golden wire. The piezoelectric drive is imbedded into the fluid cell matrix. The position of the tip is recorded by a segmented photodiode tracing the laser reflection from the back side of the cantilever. Scanning of the sample in x,y,z is realized by a piezo-scanner located below the sample. The whole volume of the fluid cell is filled with liquid (approximately $50\ \mu\text{L}$). An addition or exchange of small amounts of liquid was possible using the ‘in’ and ‘out’ channels.

For the AFM measurements we used a commercial AFM MultiMode (Nanoscope III, Digital Instruments Inc., Santa Barbara, CA) equipped with a $12\text{-}\mu\text{m}$ scanner and a provided fluid cell (Figure 8). Before use, the fluid cell was cleaned with a dish cleaner, gently rinsed with water, ethanol, low warm water and, finally, with Milli-Q ultra pure water (Millipore, USA).

3.4.2 Image processing

All AFM height images presented in this thesis were recorded using the AFMTM. The images were processed using Nanoscope software and home-written software ‘Look’ (A. Knoll, LS Physikalisches Chemie II Universität Bayreuth) with a special function of easy flattening of numerous DNA images. The DNA contour length was evaluated using DnaCalc6, which works with inverted TIFF bitmap files. The algorithm automatically recognizes a DNA chain between manually marked ends of the DNA molecule. For the end-to-end distance measurements we used Image Jv1.2, which also works with TIFF files and the ends of the molecules should be marked manually, too. Statistical analysis of the contour and persistence lengths was performed using Origin 7G.

3.4.3 Preparation of mica substrates for AFM measurements in liquids

When operating in liquid the problem of possible spillage of liquid onto the expensive electronics should be considered. Different methods were proposed to overcome this

problem: usage of a silicon ring supplied with the liquid cell by DI (MultiModeTM SPM Instruction Manual, 1999) that seals the liquid cell environment, usage of mica sheets glued onto Teflon (Muller, 1999a), etc.

In our work we developed a routine to fix mica sheets onto a metallic disc with the help of parafilm (American National CanTM). To this extend the Parafilm is stretched onto the metal disc and is heated with the mica sheet on top shortly to approximately 100°C. After the Parafilm melts, the mica sheet should be gently pressed into the Parafilm matrix. After cooling down to room temperature the discs are ready for use.

The solidified Parafilm layer holds the mica sheet good enough to be used in the AFM investigations avoiding any undesirable movement. Cleavage of the mica was performed always just before the solution for the AFM investigation is deposited. If the size of the mica sheet is chosen significantly smaller than the parafilm covered disc area, a water drop will reside on the mica surface (Figure 8). In that way prepared mica substrates allow operation of AFM in liquids omitting a usage of a silicon ring. The hydrophobic Parafilm layer protects spillage of the liquid onto the scanner. Additionally this method enables the injection of small amounts of liquid into the AFM liquid cell during scanning without danger of leakage onto the scanner. Omitting the usage of the ring enables free movement of the sample with respect to the tip and therefore increases the resolution of the AFM. And last but not least, such preparation routine allows a multiple usage of the assembled discs.

3.5 FLUORESCENCE CORRELATION SPECTROSCOPY

3.5.1 The principle of FCS

The diffusion properties of molecules in a liquid environment are size dependent. FCS traces the diffusion of single molecules in solution when they pass the small volume element determined by the focus of a microscope objective (confocal volume). To this extend the fluorescence of a fluorophore that is anchored to the molecule is monitored in time by an ultra sensitive detection device such as a photo multiplier. FCS is sensitive to complex formation whenever the latter is accompanied by a significant increase in the hydrodynamic volume (Bacia, 2003; Meseth, 1999).

The principles of FCS was introduced in the early 80ies (Ehrenberg, 1974; Magde, 1972; Magde, 1974). The fluorescence fluctuations are analyzed by calculating the autocorrelation function of the fluorescence signal detected with high temporal resolution:

$$G(\mathbf{t}) = \frac{\langle I(t) \cdot I(t+\mathbf{t}) \rangle}{\langle I \rangle^2} \quad (2)$$

where: $I(t)$ is the monitored intensity at time t and $I(t+\mathbf{t})$ is the intensity at a time interval \mathbf{t} later.

Alternatively, the potential reaction partners can be labelled with two different fluorophores. In this case, a complex formation leads to a correlation between the fluorescence fluctuations of the two dyes, which can be detected in what then is referred to as a 'cross correlation' FCS (FCCS) experiment.

All FCS measurements were performed on a Confocor 2 (Confocor2, 2001). The details of the setup are described elsewhere (Foldes-Papp, 2001; Jankowski, 2001; Meseth, 1999; Schwille, 1997b).

FCCS experiments were conducted at a excitation wavelenghts of 488nm (Argon laser) and 633 nm (HeNe-laser). The laser beams were focused into the sample by means of an 40x C-Apochromat objective (N.A. 1.2). The fluorescence was detected via the same optics and the fluorescence signal was separated from the excitation light by a dichroic mirror and a band pass filter at 550-600 nm (in the blue channel) and a long pass filter at 650 nm (in the red channel), respectively (Figure 10). The pinhole in the blue channel was adjusted with Rhodamin 6G (3.5.3) and the red channel – with Cy5 (3.5.3). The structure parameter and the size of the confocal volume of each channel were determined by measurements of the free diffusion of the two dyes. For the blue channel we reveal a waist radius of 149 nm and for the red channel we find 158 nm. To avoid photobleaching of the fluorophores we used ~5-15 μ W laser power for excitation.

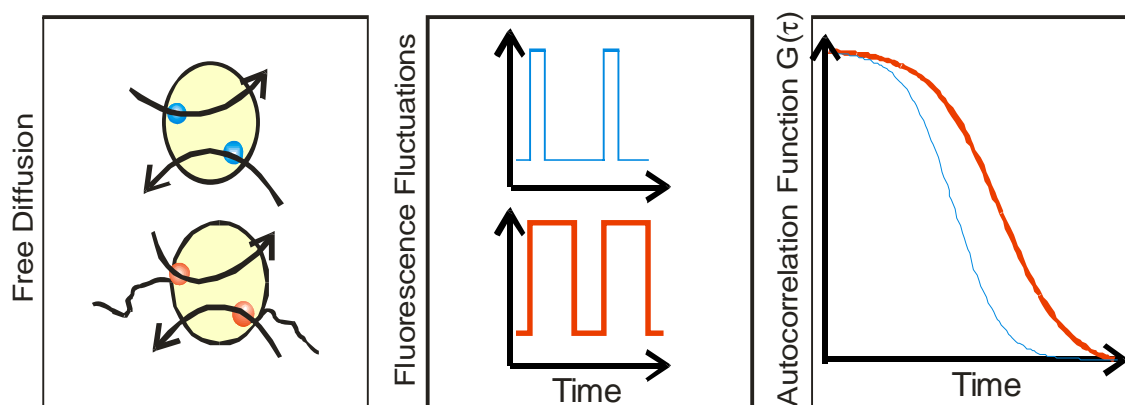


Figure 9. **The principle of the FCS.** The yellow circle represents a confocal volume. The blue molecules are small and the time of their residence in the confocal volume is short, indicated by the short peaks in their fluorescence fluctuations. As a consequence their autocorrelation function drops at short times. The red dye is anchored to big molecules and therefore stays longer in the confocal volume producing wider fluorescence fluctuation peaks. This results in a drop of the autocorrelation function at a later time.

FCS measurements were performed on cover glass (0.14 mm thickness, Marienfeld, Germany) or in a home-made closed chamber (made by H. Zettl and F. Schubert, LS Physikalische Chemie II, Universität Bayreuth).

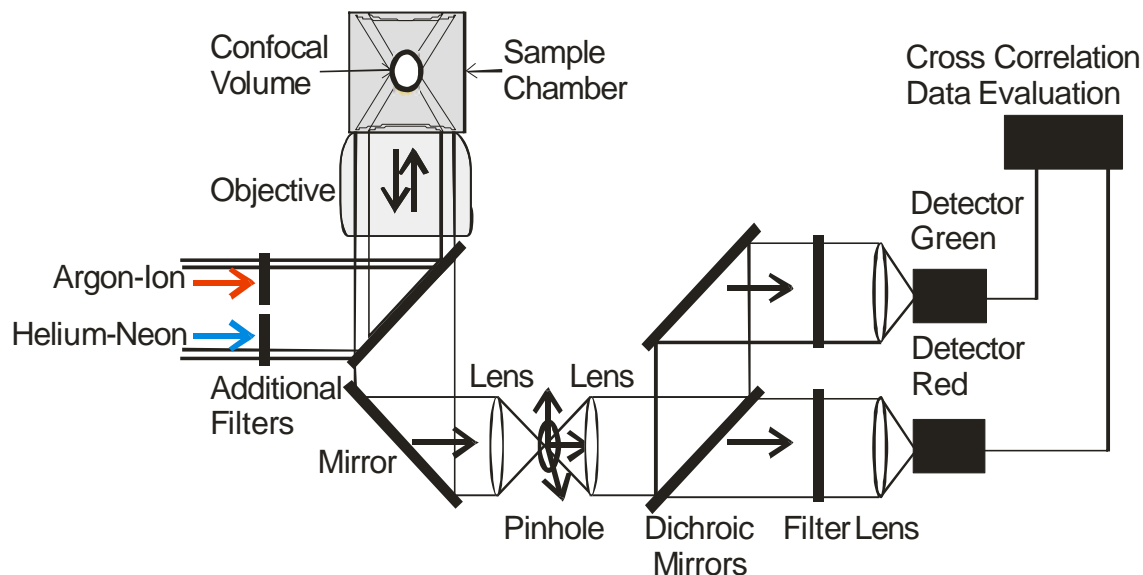


Figure 10. **Scheme of the ConfoCor 2 beampath.** Two parallel laser beams pass through a water-immersion objective in an epi-illumination arrangement resulting in two superimposing spots in the sample, forming a confocal volume element. A reduction of the fluorophore bleaching due to the reduction of the laser intensity was achieved by mounting additional filters in the laser path. The emitted fluorescence light is collected by the microscope objective, separated from the excitation light by a dichroic mirror and focused onto a pinhole by a lens. The pinhole with an adjustable diameter is located in the image plane of this lens and can be adjusted along the x - y - z axes. Fluorescence emission is parallelized, separated by a dichroic mirror into a green and red fraction and refocused on two photodiodes (Kettling, 1998).

3.5.2 Data evaluation

An evaluation of the diffusion time of the particles from FCS data was performed by fitting of the experimental data to the free diffusion model including triplet transition:

$$G(t) = \frac{1 + \frac{T}{1-T} e^{-\frac{t}{t_{tr}}}}{N} \left(\sum_{i=1}^K \frac{f_i}{1 + \frac{t}{t_i} \sqrt{1 + \frac{t}{S^2 t_i}}} \right) + 1 \quad (3)$$

where T is the fraction of fluorescent molecules that are in the triplet state with the lifetime t_{tr} , N is the average number of fluorescent molecules in the detection volume, f_i is the fraction of the i^{th} component and S is the structure parameter which describes the shape of the sample volume. The characteristic diffusion time of the i^{th} component t_i is the mean time a particle spends in the illuminated volume (Confocor2, 2001).

The experimental data of the FCCS measurement were fitted using a single particle model:

$$G(t) = \frac{1}{N} \cdot \frac{1}{1 + \frac{t}{t_{Diff}}} \cdot \frac{1}{\sqrt{1 + \frac{t}{t_{Diff} \cdot S^2}}} + 1 \quad (4),$$

The diffusion time depends on the size of the excitation volume and the diffusion coefficient:

$$t = \frac{w_{xy}^2}{4 \cdot D} \quad (5)$$

where w is the radius of the volume element in xy direction element and D is the diffusion coefficient:

$$D = \frac{k \cdot T}{6\pi \cdot \mathbf{h} \cdot r} \quad (6)$$

where k is the Boltzmann constant $1.38 \cdot 10^{-23} \text{ J/K}$, T – absolute temperature, \mathbf{h} – viscosity, r – hydrodynamic radius of the molecule. For spherical and globular molecules:

$$r = \sqrt[3]{M \cdot \frac{3N_A}{4\rho \cdot r}} \quad (7)$$

where N_A is Avogadro's number $6.023 \cdot 10^{23} \text{ mol}^{-1}$ and ρ is a mean density of the molecule (1.2 g/cm^3 and 1.8 g/cm^3 for proteins and nucleic acids respectively) (Confocor2, 2001).

From the equations 2-4 it is clear that for the same system the diffusion time is proportional to the molar mass of the object, when the structure parameter, temperature,

viscosity and density stay constant. The calculation of the theoretical diffusion times of the ORF80 complexes with dsDNA were performed assuming a globular shape of the complex.

3.5.3 The fluorescent dyes used for labeling

Fluorescence can be simply defined as the molecular absorption of light energy (photons) at one wavelength and its re-emission at another, usually longer, wavelength. However, only fluorescent markers that have high fluorescence quantum yield, high photobleaching resistance and low probability of excitation of the triplet state are suitable for FCS. Cy-DyeTM is a brand name for a range of fluorescence dyes, so called as they evolved from a dye class called the cyanines. They are often used for FCS. The main fluorescence characteristics of the fluorescence markers used in this thesis are presented in Table 2.

Dye	MW	Absorbance [nm]	Emission [nm]	Quantum yield
Cy3	767	552	570	0.13
Cy5*	535	643	667	0.2
Cy5.5	635	675	694	0.3
Alexa Fluor 488	643	494	517	0.5

Table 2. The fluorescent characteristic of dyes used as markers in FCS experiments.

4 RESULTS AND DISCUSSION

4.1 SURFACE-IMMOBILIZATION OF BIOMOLECULES FOR AFM INVESTIGATIONS IN LIQUIDS

The AFM (Binnig, 1986; Hansma, 1988) provides the unique opportunity to image and size individual biological molecules in their natural hydrated state (Hansma, 1993; Hansma, 1995; Hansma, 1988; Marti, 1987). Thereby artifacts caused by washing, drying and contrast enhancement techniques are avoided. AFM provides topographical information about biomolecular structures that are adsorbed at a solid-liquid interface (3.4); therefore immobilization of the molecules on the solid support is mandatory.

When the molecules are in solution they can have all possible conformations accessible within the range of their thermal energy. During deposition onto the surface the molecules undergo a transition from three to two dimensions. The loss of one degree of freedom introduces conformational changes, especially significant for long molecules, such as DNA. It can lead to two extreme cases of the molecules-surface interaction. In the first case the molecules approach the surface and re-equilibrate in two dimensions achieving the lowest energy conformation before they are captured in a particular conformation. In the second case the molecules adhere without being equilibrated on the substrate and their conformation reflects the history of their approach to the surface (Rivetti, 1996).

An immobilization of biomolecules for an AFM investigation in air is relatively simple, since after drying of the sample all molecules from a bulk solution are immobilized on the surface. However, drying of the sample may induce changes in the biomolecular conformation (Rivetti C, 2001) and fully prohibits the possibility of a time-resolved measurements using AFM. Therefore, we were looking for an immobilization strategy, which would allow the visualization of the biomolecules in liquids. There are two different approaches for the immobilization of biomolecules in liquids, which differ according to the nature of the interaction between the molecules and the surface. They can be either covalent or non-covalent (Shlyakhtenko, 1999; Wagner, 1998). A chemical modification of the solid support and, especially, of the biomolecules, which is needed for a covalent immobilization, can cause undesirable changes in their biological functions. Additionally, the covalent immobilization leads to a firm fixation of the biomolecules on the surface and, as a consequence, makes time-resolved AFM measurements problematic.

In contrast to the covalent strategy of immobilization, the non covalent immobilization is based on a physisorption of the biomolecules at the surface. This approach does not require any functionalization steps. Since the DNA's sugar-phosphate backbone carries

a negative charge it was proposed to use positively charged ions in order to fix DNA on the negatively charged mica surface (Bezanilla, 1995; Bustamante, 1992; Guthold, 1994). Additionally, it was found that the nature of the ions, the value of their ionic radii, the charges and concentration of the ions affect the adsorption and the conformation of DNA molecules on the mica surface significantly (Hansma, 1996a). In our experiments we used magnesium and nickel ions for the non covalent immobilization of DNA molecules. Both Mg^{2+} and Ni^{2+} are physiologically important ions. Magnesium ions play a pivotal role in nucleic acid biochemistry, enzyme activation, and many other biological processes (Ebel, 1980; Saris, 2000). Ni^{2+} is known to occur as a cofactor in some enzymes (Volbeda, 1996). Besides, Ni^{2+} was shown to have a cancerogenic activity (Kawanishi, 2002; Sunderman, 1983; Zienolddiny, 2000), because of its possible interaction with DNA (Huq, 2000; McLachlan, 1996; Moldrheim, 1998; Muller, 1999b; Subirana, 2000).

Recently, a few reports about successful time-resolved AFM investigations of DNA-protein interactions were published (Guthold, 1999; Kasas, 1997; Rippe, 1997; van Noort, 1998). From the first experiments it became clear that the surface-immobilization of biomolecules for dynamic AFM imaging is a major issue. Immobilization of biomolecules for such experiments requires the resolution of an apparent paradox. On one hand, it requires the immobilization of biomolecules on the surface *stable* enough to be visualized with a scanning tip and, on the other hand, *loosely* enough in order to diffuse in 2-D (in the mica surface plane) and to participate in the molecular interactions (Argaman, 1997; Bustamante, 1997; Lal, 1994). Naturally, the biomolecules should be attached to the surface without losing their biological functions.

Because of the fact that AFM visualizes only molecules that are immobilized on the surface, the way of deposition is very important (Hansma, 2000; Rivetti, 1996; Wagner, 1998). Therefore, the study of the deposition of the biomolecules for AFM investigation in liquids and an improvement of the protocols for their immobilization were our primary tasks.

4.1.1 Influence of Mg^{2+} and Ni^{2+} on DNA immobilization on mica

For the immobilization of negatively charged DNA molecules on a negatively charged mica surface we used divalent ions in low osmotic strength HEPES buffer (2.2). In our experiments we did not apply any rinsing, washing, short-time drying or any other additional treatment of the samples.

In order to avoid kinetically trapped DNA molecules (Rivetti, 1996) and to establish conditions when molecules are only loosely bound to the surface, i.e. are pinned to the

surface at few sites along the DNA chain, a series of experiments with different immobilization protocols were performed. We examined in details three cases, when (a) Ni^{2+} ions were premixed with the DNA solution before its deposition onto the mica surface, when (b) Ni^{2+} was added immediately after the sample deposition and (c) one minute after the sample deposition onto the mica surface. Solutions of 538 bp DNA (2.3.2) with a concentration of 1-3 nM in AFM deposition buffer (2.2) were used in these experiments.

Direct sizing of DNA molecules from the AFM images (Figure 11, A-C) shows that different Ni^{2+} concentrations do not influence the contour length, $L_{\text{DNA}} = 172 \pm 19$ nm, of the linear 538 bp DNA fragment. This value is in excellent agreement with the theoretically calculated value of 182 nm for 538 bp long fragments of B-DNA assuming a length of 0.34 nm per base pair. This level of precision of the AFM sizing seems reasonable considering the potential error introduced by the finite size of the AFM tip. This error is particularly relevant when short molecules are investigated (Figure 24, B).

A persistence length, P_{DNA} , is an important statistical parameter that describes the stiffness of a DNA molecule (1.1, equation 1). With AFM it is inherently impossible to distinguish between an intrinsic conformation of a DNA molecule and a conformation induced by the surface adsorption process. Nevertheless, the comparison of the theoretical values of $\langle R^2 \rangle_{2\text{D}}$ and P_{DNA} with those determined from AFM images indicates the state of equilibration of the DNA molecules on the surface (Rivetti, 1996).

Our AFM results indicate that both $\langle R^2 \rangle_{2\text{D}}$ and P_{DNA} are dependent on nickel ions concentration as well as on the way of their addition (Figure 11). Premixing (Figure 11, A) or immediate addition (Figure 11, B) of Ni^{2+} to the DNA samples deposited onto the mica surface leads to rather low values for both $\langle R^2 \rangle_{2\text{D}}$ and P_{DNA} (Figure 11, D a, b). According to Rivetti *et al.* (Rivetti, 1996) such low values indicate that DNA molecules are trapped on the surface and the conformation of the DNA molecules reflects the history of their surface approach. Our AFM study of DNA molecules immobilization clearly shows that the highest $\langle R^2 \rangle_{2\text{D}}$ and P_{DNA} values were obtained when the DNA samples were placed onto the mica surface and Ni^{2+} was added one minute later (Figure 11, D c). At these Ni^{2+} concentrations the DNA molecules were immobilized on the mica surface good enough to be visualized by AFM (Figure 11, C).

It is important to note that an increase of the delay time before Ni^{2+} injection to more than one minute has no influence on both $\langle R^2 \rangle_{2\text{D}}$ and P_{DNA} .

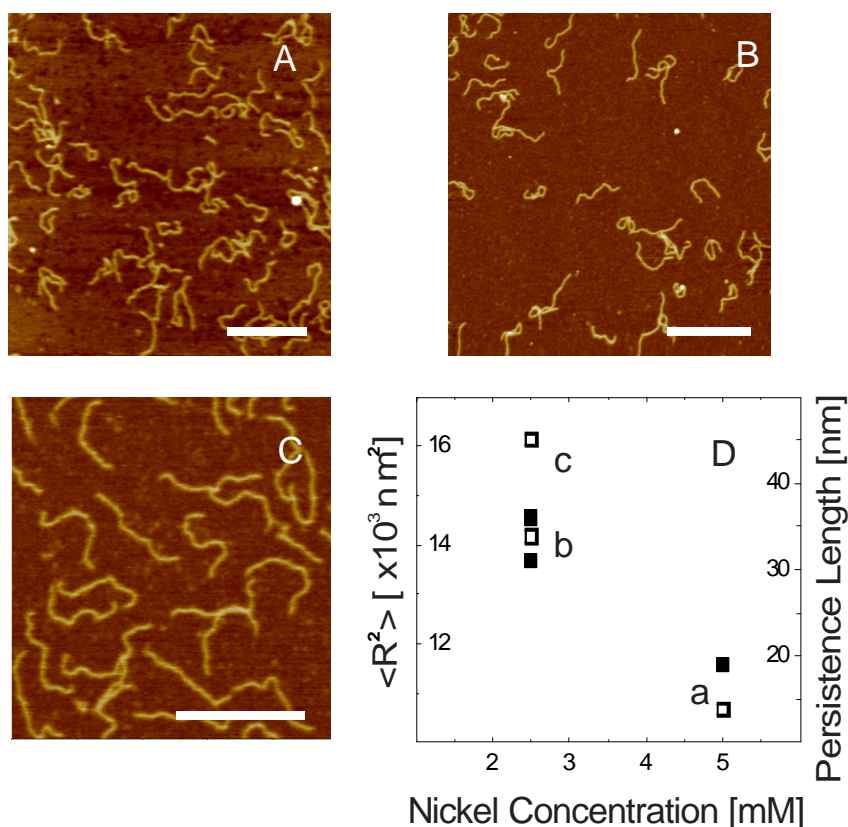


Figure 11. **Influence of the nickel ions concentration and the way of its addition on the conformation of dsDNA molecules studied with AFM.** AFM images of the DNA when (A) nickel chloride (concentration of 5 mM) was premixed with DNA solution and afterwards deposited onto freshly cleaved mica; (B) Ni²⁺ solution (concentration of 2.5 mM) was added to the DNA sample immediately after its deposition; (C) the same as in (B), but Ni²⁺ was added to the DNA sample that have been kept on mica for one minute. A-C AFM height images obtained in buffer. The scale bar corresponds to 200 nm, z range is 10 nm. Graph D shows the dependence of the persistence length (filled symbols) and the mean square end-to-end distance (empty symbols) on the concentration and the way of the Ni²⁺ addition determined from the corresponding AFM images (marked with small letters).

This result is in good agreement with the results of Rivetti *et al.* (Rivetti, 1996), who analyzed the relation of the polymer length with the time needed for its equilibration in 2-D. They found that for DNA molecules shorter than 5000 bp less than one minute is needed for the equilibration in 2-D.

and, as a consequence, reproducible AFM imaging using 1 mM of Ni²⁺ ion concentration (data not shown) as reported by Hansma *et al.* (Hansma, 1996a).

In summary, our study of the DNA deposition for the AFM experiments shows that addition of Ni²⁺ does not influence the L_{DNA} of the 538 bp DNA fragment. Nevertheless, both $\langle R^2 \rangle_{2\text{D}}$ and P_{DNA} of the 538 bp DNA fragment are sensitive to the presence of Ni²⁺. Addition of Ni²⁺ at a concentration of 2.5 mM to the DNA sample after one minute of its equilibration on the mica surface gives the highest values of both $\langle R^2 \rangle_{2\text{D}}$

and P_{DNA} . This procedure for the immobilization of DNA molecules for AFM investigation was used throughout this work.

4.1.2 Dynamic investigations of the immobilization of DNA molecules

In order to study a mechanism of the DNA molecules immobilization we performed dynamic AFM experiments. For this purpose we scanned a mica surface in an AFM deposition buffer (2.2) environment before addition of the DNA sample. The AFM height image depicted in Figure 12 A shows the very flat mica surface, with a mean roughness of ~ 0.1 nm.

However, when a DNA solution was injected into the liquid cell during scanning, the AFM height images of the same spot of the sample surface are significantly different (Figure 12, B) in comparison to the bare mica surface (Figure 12, A). We suppose that the change is due to the presence of DNA molecules in the vicinity of the surface. But under these conditions the DNA molecules are not efficiently immobilized on the mica surface to be clearly visualized with AFM. Probably, the mobility of the DNA molecules beneath the scanning tip is responsible for the low quality of the AFM imaging. Similar results were reported by Hansma *et al.* (Hansma, 1996a). They also found that application of Mg^{2+} ions for the immobilization of the DNA molecules for the AFM imaging in liquids was inefficient. In their experiments the DNA molecules were visible with AFM only after rinsing and drying of such samples.

For efficient immobilization of DNA molecules on the mica surface an addition of nickel ions was necessary in our experiments. It immediately reduces the movement of the DNA molecules beneath the scanning tip. As depicted in Figure 12 C, soon after Ni^{2+} addition (marked with a green arrow in Figure 12, C) the imaging of the DNA molecules improves significantly within one scan area. The DNA molecules are clearly visible in the top half of the image (Figure 12, C). Figure 12 D presents the AFM image of the same spot as in Figure 12 C, but recorded from top to bottom. The comparison of Figure 12 C and Figure 12 D shows that the DNA molecules are not firmly attached to the surface and are still able to change their conformations under the applied conditions (see marked places in Figure 12, C and D).

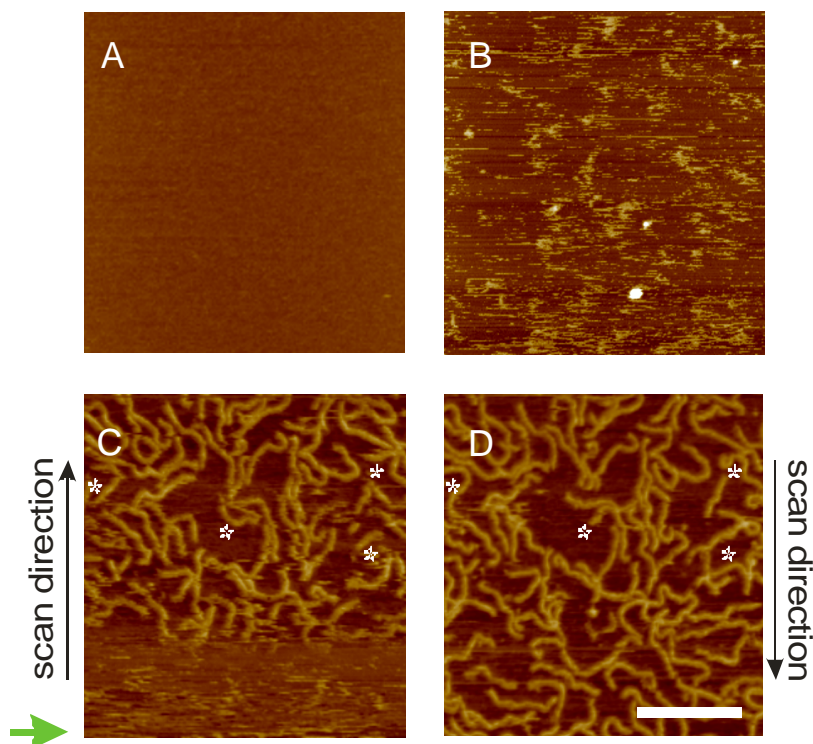


Figure 12. **Sequence of AFM images showing the events of the DNA molecules attachment.** AFM height image of the mica surface (A) scanned in AFM deposition buffer; (B) AFM image of the same place after addition of the DNA solution - the loosely bound molecules are highly movable under the scanning tip and a clear AFM imaging is not possible. In C the addition of a 2.5 mM NiCl_2 solution (marked with the arrow) leads to a better attachment of the molecules to the surface and reduces the movement of the DNA molecules on the mica surface making single DNA molecules visible (scan up direction); in D – the same as C but scan direction down, where the displacements of single DNA molecules are visible (pointed with asterix in C and D). The scale bar corresponds to 250 nm, the z range is 10 nm.

Our AFM experiments on the immobilization of DNA molecules showed a clear difference in the immobilization properties of the divalent cations Ni^{2+} and Mg^{2+} (Figure 12). Magnesium belongs to the earth-metal group with p electrons in its outer shell, which explains its rather low tendency to form complexes. Nickel, though, is a divalent transition metal cation with d electrons in its outer shell, which significantly increases its tendency to form complexes in solution. As a result, Ni^{2+} forms complexes with other ligands as water as well.

It is well known that divalent ions participate in the stabilization of the DNA double helix, since they have an affinity to the negatively charged DNA chain.

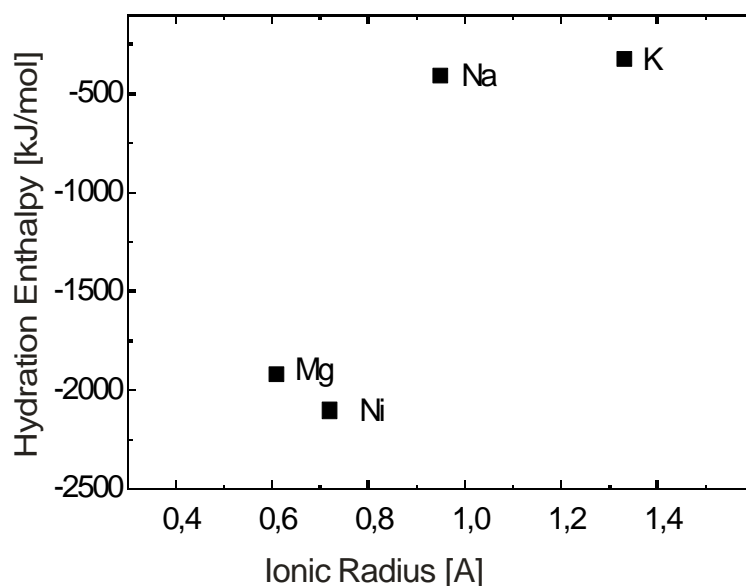


Figure 13. **Dependence of the hydration enthalpies of the divalent ions versus their ionic radii.** (Bockris, 1977; Cotton, 1972) Minus means exothermic reaction.

X-ray crystallography and the melting temperature assay showed that Mg^{2+} binds preferentially to the DNA sugar-phosphate backbone and thereby stabilizes the DNA double helix structure (Barton, 1980; Saenger, 1984; Soler-Lopez, 1999). However, the atomic-resolution of the B-DNA crystal structure reveals that the role of magnesium ions is not limited to merely interacting with backbone phosphate groups. It was also found to be present in the minor and major grooves of the DNA duplex with the preferential location next to either a phosphate group or terminal hydroxyl groups (Minasov, 1999). It was also shown that Ni^{2+} has a higher affinity to the DNA bases than Mg^{2+} (Barton, 1980; Saenger, 1984).

On the other hand, an AFM study of the DNA binding properties to a mica surface showed a clear correlation of the binding strength with the cationic radii (Hansma, 1996a). After cleavage a plane of the mica surface is composed of hexagonal arranged oxygen tetrahedra with Al^{3+} or Si^{4+} in the middle. Such structures form cavities with a spacing of $\sim 0.5 \text{ \AA}$. A comparison of the ionic radii presented in Figure 13 shows that Ni^{2+} and Mg^{2+} fit better than Na^{+} and K^{+} into these cavities on the mica surface and therefore bind the DNA molecules more efficiently on the mica surface.

The ability of Mg^{2+} and Ni^{2+} to fix DNA molecules at the surface correlates very well with the values of their hydration enthalpies (Figure 13). Such ions like Na^{+} and K^{+} are strongly hydrated (with primary water) and the changes in hydration free energy (required for contact adsorption) are too large, therefore the transition to the liquid-solid interface is not energetically favourable. Ions which are sufficiently hydrated do not contact-adsorb (Bockris, 1977). Hydration is dependent on the radius of the ions; see, e.g. a plot of hydration enthalpy versus ionic radius in present in Figure 13. Such ions

like Mg^{2+} and Ni^{2+} have approximately equal values of the hydration enthalpies. Mg^{2+} presumably retains some of its water of hydration (Israelachvili, 1997) when interacting with mica and DNA. Mg^{2+} builds longer and therefore mobile bridges between the negatively charged sugar-phosphate backbone of the DNA and the mica surface, which explains its lower immobilization efficiency in comparison to Ni^{2+} .

The dynamic experiment of DNA molecules immobilization (Figure 12) may also explain the importance of the delay time for the re-equilibration of the DNA molecules (Figure 11, C). We believe that even without addition of Ni^{2+} the DNA molecules in the AFM deposition buffer are already located in the vicinity of the surface and have time for the primary re-equilibration from their 3-D to their 2-D conformation. The immediate adsorption is probably enhanced by the low osmotic strength of the AFM deposition buffer (2.2) and, additionally, by the presence of small quantities of divalent Mg^{2+} from the AFM deposition buffer, which are known to enhance the adsorption of DNA on the charged mica surface (Hansma, 1996a). A subsequent addition of Ni^{2+} enhances fixation of the DNA molecules on the mica surface.

We conclude that the DNA molecules adsorb to the surface prior to Ni^{2+} addition, which indicates that the conformations found after Ni^{2+} addition under concentrations below 3 mM reflect the conformation of the DNA irrespective of Ni^{2+} . We suppose that the higher efficiency of the DNA immobilization on the mica surface is explained by both the size and the higher complex-forming property of Ni^{2+} in comparison to Mg^{2+} . Additionally, Ni^{2+} binding to DNA is not restricted by interactions with the phosphate backbone, but ligation with the DNA bases is also not excluded. The optimized Ni^{2+} concentration ($c=2.5$ mM) merely stabilizes the already adsorbed molecules, which enables imaging by AFM, but not fully freezes the conformation of the DNA molecules and they are still able to change their conformations (Figure 12, C and D).

4.1.3 Molecular motions monitored by the time-resolved AFM imaging

A very challenging application of AFM is the direct tracing of dynamic interactions of biomolecules. Since the invention of the AFM researches have steadily progressed towards imaging biological samples in an aqueous environment and monitoring biochemical processes at a nanometer resolution in real time.

For such time-resolved AFM measurements of molecular interaction the immobilization of the biomolecules at the surface is the most important and the most critical point. Our next task was to prove if the established procedure for the immobilization of the biomolecules (4.1.1) enables diffusion of the molecules on the substrate and is suitable for time resolved AFM investigations. For this purpose, we trace time-resolved displacements of the biomolecules with AFM.

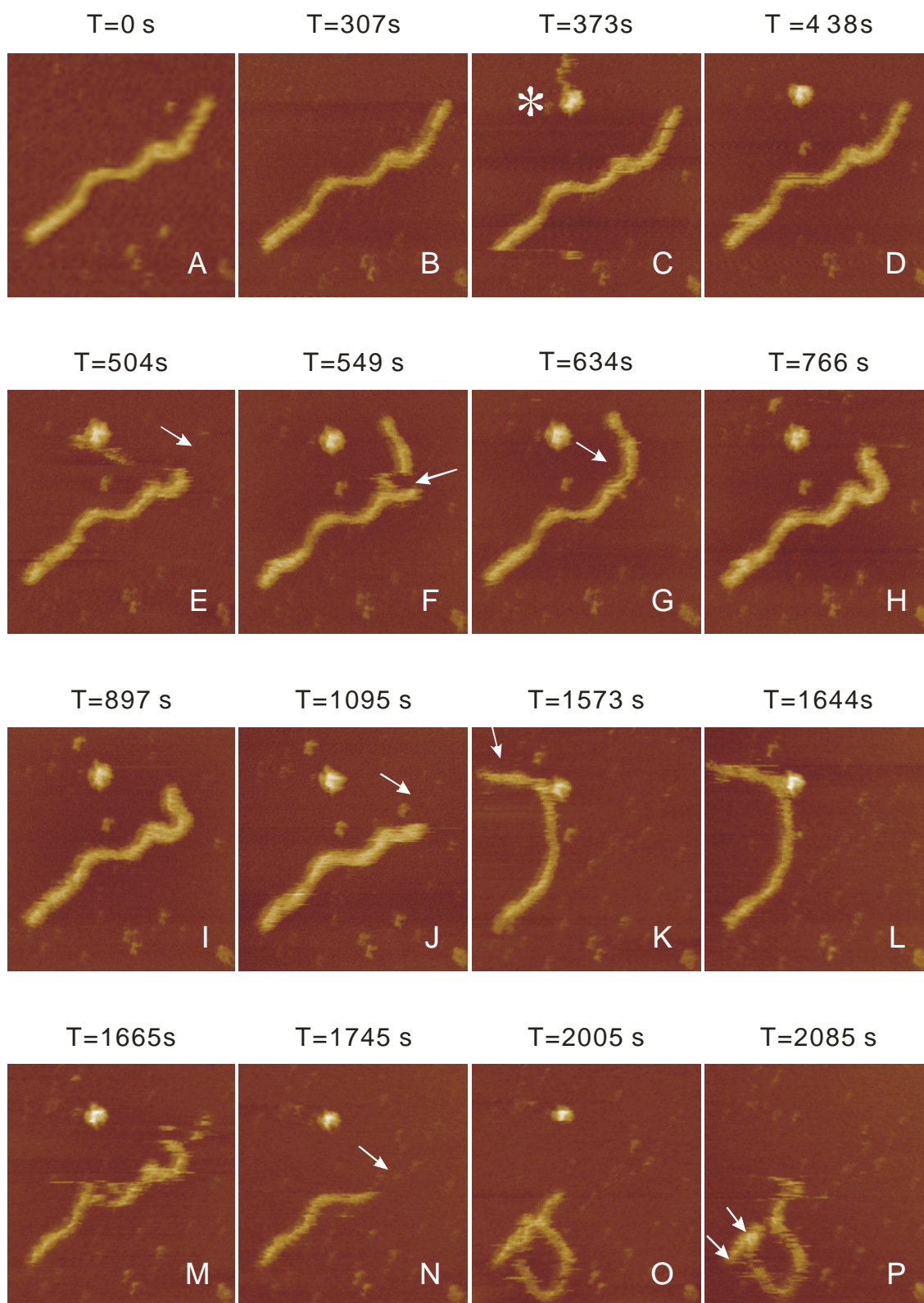


Figure 14. **Sequence of AFM images of a single 362 bp DNA molecule containing defined platinum adduct with a single protein subunit.** Scan of the same spot for 2085 seconds. The AFM images (A-P) show movements of the single linear DNA molecule and its interaction with the protein. A hRPA subunit appears in the second image (marked with asterisk in C), stays fixed to the surface in all images in the sequence up to O and disappears in the last image of the sequence. The scan size is 120 nm, z range is 10 nm.

Figure 14 presents a time-resolved measurement of the interaction of a DNA molecule containing a single cisplatin modification (2.3.4) with RPA. From the sequence of AFM images we can clearly see the movements of the single DNA molecule on the mica surface. In the third image in the sequence (Figure 14, C) a globular object (marked with asterix) appears beside the stretched DNA molecule, which was not present before (Figure 14, A and B).

Taking into account the shape and the size of the globular object, we assume that it derives from the hRPA sample and could be a single subunit of a hRPA protein. With the appearance of the protein subunit the DNA molecule starts to move. It is important to note that the movements of the DNA molecule presented in Figure 14 took place only after the appearance of the globular object in the third image (Figure 14, C). Continuous scanning (~5 minutes) of the same molecule before this event did not reveal any conformational changes of the stretched DNA chain (Figure 14, A and B).

After a few changes of its conformation the DNA chain partially leaves the surface (see arrows in Figure 14, E and J), reducing its apparent contour length by up to 20 nm. It is clearly visible that the movements of the DNA molecule below the scanning tip induce a poor quality of the AFM image (Figure 14 F, M-P). The same effect of the mobility of DNA molecules beneath the scanning tip was responsible for the low quality of the AFM imaging when the molecules were attached to the surface only via magnesium ions (Figure 12 B). After 1573 seconds of investigation the DNA makes a 'jump' to the protein, stays at the place of the protein (Figure 14, K and L) and afterwards returns to approximately the primary position (Figure 14, M).

In Figure 14 N the DNA molecule appears significantly shorter in comparison to the same DNA molecule in the adjacent images in the sequence, what may be explained by the detachment of the part of the molecule from the mica surface. 1599 sec after the start of the experiment the DNA returns back to the mica surface but the conformation of the molecule is no longer stretched (Figure 14, O). In the last image of the sequence (Figure 14, P) the protein subunit fully disappears from the scanning area. During this time-resolved AFM measurement only one part of about 20 nm has not moved (between the arrows in Figure 14, P), i.e. was firmly pinned to the substrate surface) and 100 nm of the DNA chain was rather free to move and interact with the other molecule. Our time-resolved measurements with AFM shows that the application of a 2.5 mM Ni²⁺ solution achieves only partial attachment of the DNA molecules on the surface and the molecules are still able to change their conformation. Moreover, our results show that the DNA motion appears as a consequence of the proximity to a protein and are oriented in the direction of the protein.

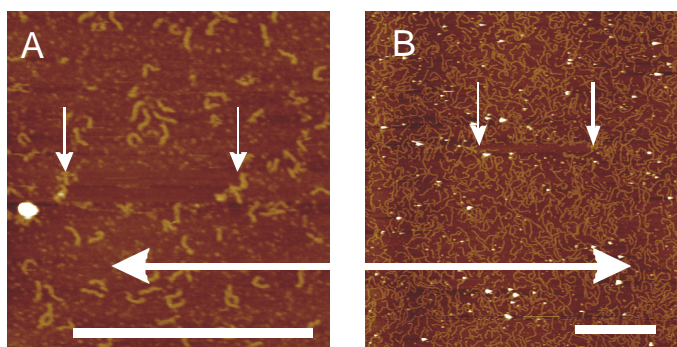


Figure 15. **Tip induced movements of the biomolecules on the mica surface.** (A) Zoomed out AFM image of the ARS1 DNA, scale bar corresponds to 750 nm, z data scale 10 nm. (B) AFM image of the undamaged 538 bp DNA with RPA, scale bar corresponds to 750 nm, z range is 10 nm. White arrows indicate the edges of the area where the DNA molecules have been moved aside due to the tip movement. The direction of the tip movement is marked with a horizontal arrow.

The attachment of the DNA molecule on the mica surface can be explained by the interaction of the multiple binding sites along the DNA chain with the binding sites on the mica surface. Under the applied immobilization conditions the strength of the interaction per contact is low and/or the number of contacts is not high, since the mobility of the DNA chain is still visible and a partial terminal desorption of the DNA molecule is still possible. However, the full detachment off the surface is not favourable.

This time-resolved experiment shows that the diffusion of the DNA molecules in 2-D under the applied immobilization conditions is still slow enough; therefore changes of the conformation of the DNA molecules within one scan time are negligibly small. This fact allows us to perform a statistical analysis of the dimensions of the DNA molecules from the AFM images. However, the detection of the molecular movements in the time-resolved AFM experiment when 5 mM Ni^{2+} was used for the DNA immobilization was unsuccessful. Definitely, an application of such a high Ni^{2+} concentration leads to the firm attachment of the DNA molecules on the mica surface (data not shown), increasing the number of the DNA-mica contacts.

Of course tip-induced molecular movement during the AFM scan cannot be excluded. For instance, if wrong parameters for the AFM imaging are used (drive frequency, amplitude set point, etc) and the forces of the tip-sample interaction are too high (Weisenhorn, 1989) we can see in the ‘zoomed out’ picture an imprint of the previous scan area (Figure 15). In this case the molecules are definitely moved due to the movement of the tip. Large lateral forces are created which easily sweep away all molecules encountered. In Figure 15 A the scan area of 450 nm in width (between the arrows in Figure 15, A) free from molecules is seen in the zoomed out image. The DNA molecules are moved to the edges of the previous scan area (see arrows in Figure 15,

A). In such cases the width of the clean area coincides exactly with the width of the previous scan. The same effect is visible in the Figure 15 B where a 3x3 μm AFM image of DNA-hRPA complexes is presented. On this zoomed out image we clearly see a rectangular-shaped space free from biomolecules. The distance between the arrows coincides exactly with the scan size ($\sim 1 \mu$) of the previous scan area. Additionally, in both images (Figure 15, A and B) the orientation of the moved molecules coincides exactly with the direction of the movement of the tip (marked with horizontal arrow) and the width of the area free from molecules corresponds exactly to the previous scan area.

In summary, it is evident that the applied immobilization method allows the visualization of single DNA and protein molecules in real time. Under these conditions the biomolecules are still able to diffuse in the plane of the mica surface. Further dynamic investigations using AFM open challenging opportunities of the visualizations of the biomolecules' function under physiological conditions and would definitely open new insights into the structure-function relationship.

4.1.4 Immobilization of plasmid DNA, proteins and DNA-protein complexes

In the next step the question about the applicability of the developed immobilization protocol for plasmid DNA, different classes of proteins and DNA-protein complexes arose. The experiments showed that an AFM investigation of plasmid DNA might be problematic using the immobilization protocol described above (4.1.1). Plasmid DNA is a rather long, circular molecule and tends to coil.

It has been already shown that plasmid DNA appears in the supercoiled state, when measured with AFM *in situ* (Cherny, 2001; Lyubchenko, 1997). In the Figure 16, A the molecules of plasmid pUC19_{ARS16} (2.3.3) are looking like globular objects.

The 'relaxation' of the plasmid DNA on the mica surface improved significantly after the application of a temperature equilibration for 3-4 hours at room temperature (Figure 16, B and C) or a short heating up to 60°C (Figure 16, D) before its deposition on mica. As it is evident from Figure 16 B-D, an additional treatment of plasmid DNA is important for its relaxation from the coiled state (Figure 16, A).

When working with high dilutions of the proteins (down to nM concentration), one should keep in mind that a protein can stick to the surfaces of the reagent tubes, pipettes' tips, etc.

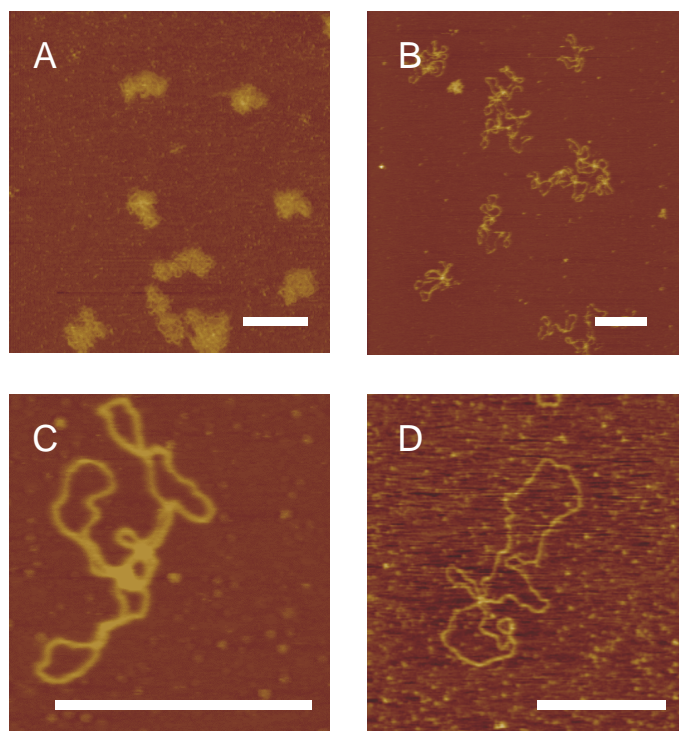


Figure 16. **AFM images of plasmid DNA deposited according to different immobilization protocols.** Plasmid pUC19_{ARS16} (**A**) immobilized on the mica surface; the same plasmid DNA immobilized on the mica surface after temperature equilibration (**B**, **C**); plasmid DNA deposited on mica after short preheating to the 60°C (**D**). The scale bar corresponds to 400 nm, the z data scale is 10 nm.

Therefore, both the protein and the DNA-protein complex solutions were prepared on Parafilm sheets. Additionally, application of silanized pipettes tips and Eppendorf tubes were found very helpful.

Since the proteins are polyelectrolytes and have on their surface positive and negative charges (amino- and acidic groups), the pH value of the deposition buffer influences the surface charge of the protein. If the proteins are in a buffer which has a lower pH as the isoelectric point of the proteins, the protein carries a resulting positive charge on its surface and can be directly immobilized on the partially negative charged mica surface. So, an attachment of the protein on the freshly cleaved mica surface is possible without application of divalent ions. For instance, ORF80 carries a positive charge in the AFM deposition buffer and an application of Ni²⁺ for the molecules immobilization on the surface is not necessary (Figure 17, A).

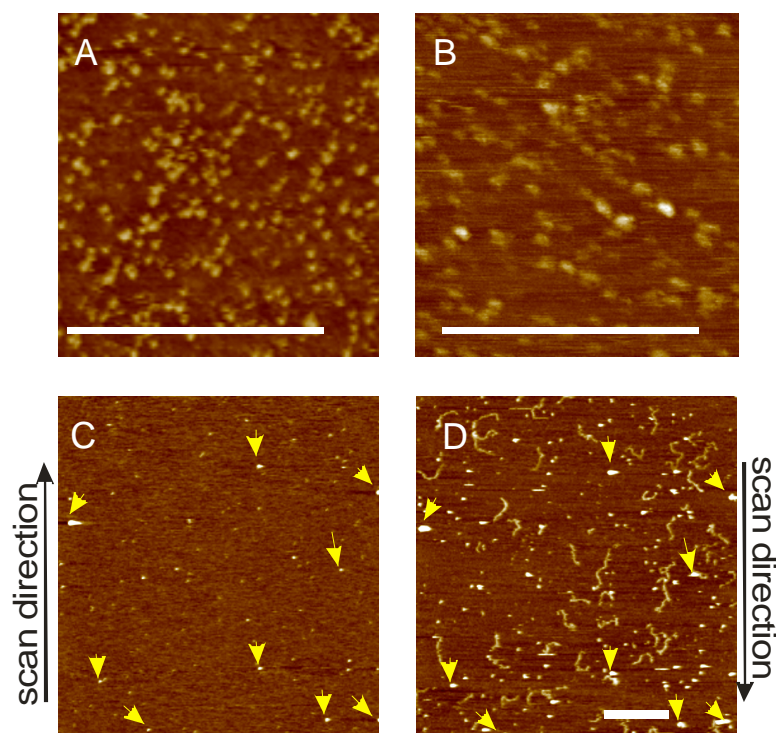


Figure 17. **AFM images of the protein and protein DNA complexes immobilized on mica.** ORF80 (A) and XPA (B) on the mica surface. In the AFM image of the DNA and RPA complex in the AFM deposition buffer globular objects are visible on the mica surface when no Ni^{2+} was added (C); after Ni^{2+} addition additional to the DNA molecules one can still see (D) the same objects as in C (the same places are marked with arrows in C and D), The scale bar corresponds to the 400 nm, the z data scale is 10 nm.

Human RPA (2.4) and XPA (2.4) (Miura, 1991) (Figure 17 B), in contrary, have an isoelectric point below 8 and therefore require Ni^{2+} addition to the protein solution in the AFM deposition buffer (pH=8) to achieve immobilization of the proteins on the mica surface. It is important to note that the compositional purity of our material favoured good imaging.

From the AFM images (Figure 17 A) the dimensions of the protein molecules can be measured (4.5.2.1). It has been shown recently that the buffer conditions applied for the visualization of the protein molecules in liquids have a dramatic influence not only on the AFM resolution, but also on the measured heights of the molecules (Rossell, 2003). In order to compare the dimensions of the proteins and the DNA protein complexes all measurement described in this thesis were performed under the same buffer environment, namely AFM deposition buffer (2.2).

The investigation of the DNA protein immobilization mechanism showed that DNA/protein complexes are present in the vicinity of the mica surface even without addition of Ni^{2+} . For the immobilization of the pre-incubated DNA-protein complexes the same protocol as for DNA molecules alone (4.1.1) was used. In Figure 17 C an image of the DNA/protein sample before Ni^{2+} addition scanned in AFM deposition

buffer is presented. The same objects are present in the next scan of the same place after Ni^{2+} addition (Figure 17 D). Addition of Ni^{2+} improved the resolution of the AFM imaging so that DNA and protein molecules could be clearly visualized with AFM. Here we observed the same effect as in experiments presented in Figure 12.

4.1.5 Study of the influence of Ni^{2+} , Na^+ and H^+ on the DNA hydrodynamic properties using FCS and FCCS

In contrast to AFM, FCS and FCCS (3.5) give the possibility to track changes of DNA molecules in bulk solution that may happen as a consequence of the Ni^{2+} , Na^+ and H^+ addition. We analysed the dependence of the diffusion time of fluorescence labeled DNA on the concentration of those ions.

For these experiments we chose DNA fragments of two different lengths. One rather long fragment of 440 bp modified with Cy5 on one end (2.3.2) and a short 36 bp DNA modified with two different fluorescence labels on both 5' ends (fragment I, Table 1).

The experiments with the 440 bp DNA fragment showed that the diffusion times decreased with increasing laser power indicating bleaching of the fluorophore. Therefore it was necessary to reduce the intensity of the laser. Reduction of the laser power down to 68 nW was achieved by inserting an additional filter into the laser beam path (Figure 10).

Using FCCS for the experiments with the 36 bp DNA molecules (2.3.1) fully excludes the influence of the free dye and unhybridized ssDNA strands labeled with the fluorophore, tracing only the hydrodynamic properties of dsDNA. The influence of the Ni^{2+} addition on the hydrodynamic properties of the 440_{Cy5} and 36 bp DNA fragments studied with FCS and FCCS is presented in Figure 18. Our results show that an addition of Ni^{2+} influences not only the diffusion time of the molecules, but also the number of DNA molecules in the confocal volume (Figure 18). As we see from Figure 18 B the diffusion time of the 36 bp fragment stays constant up to a Ni^{2+} concentration of 3.8 mM at a value of its diffusion time in AFM deposition buffer ($\tau_0=232\pm 14 \mu\text{s}$). However, a further increase of the Ni^{2+} content up to 9 mM leads to a significant decrease in the diffusion time of the 36 bp DNA fragment (up to 40 % of the initial diffusion time). On the other hand, the increase of Ni^{2+} concentration from 3.8 mM to 9 mM leads to a decrease of the number of DNA molecules in the focus down to 70 % and 34 % of the initial value, respectively (Figure 18 C).

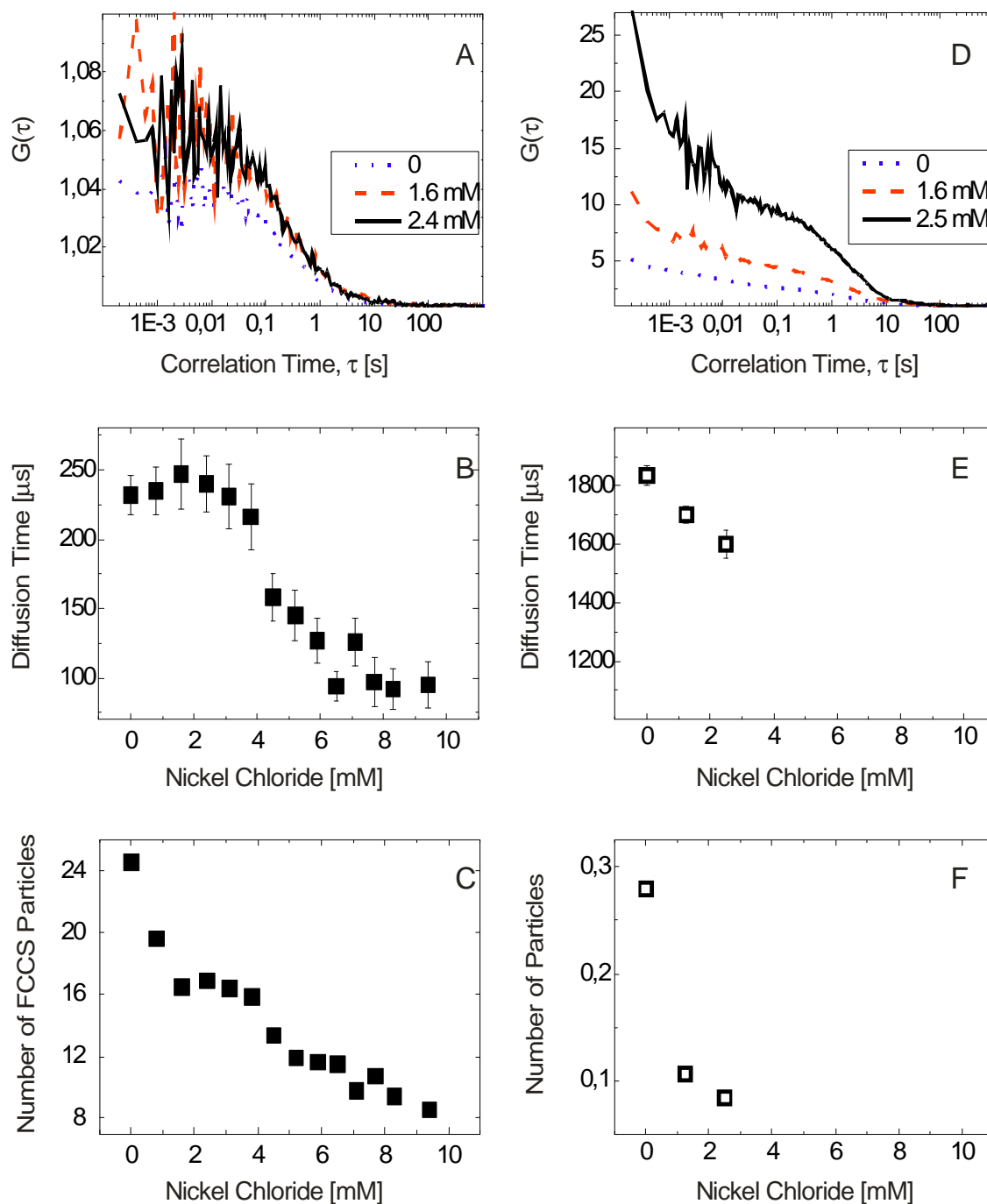


Figure 18. **Dependence of the DNA diffusion time and the numbers of particles determined by FCS and FCCS as a function of Ni^{2+} concentration.** FCCS autocorrelations curves for 36 bp DNA (A), fit to the data (A) yields to the diffusion time (B) and number of particles (C) as a function of Ni^{2+} concentration; FCS autocorrelations curves of 440 $_{\text{Cy5}}$ DNA (D), fit to the data (D) yields to the diffusion time (E) and number of particles (F) as a function of Ni^{2+} concentration.

Similar experiments with 440 bp DNA labeled with Cy5 also show that the addition of Ni^{2+} influences the DNA diffusion time (Figure 18, E). At a Ni^{2+} concentration of 2.4 mM it decreases to 90 % of the diffusion time of the same fragment in the deposition buffer.

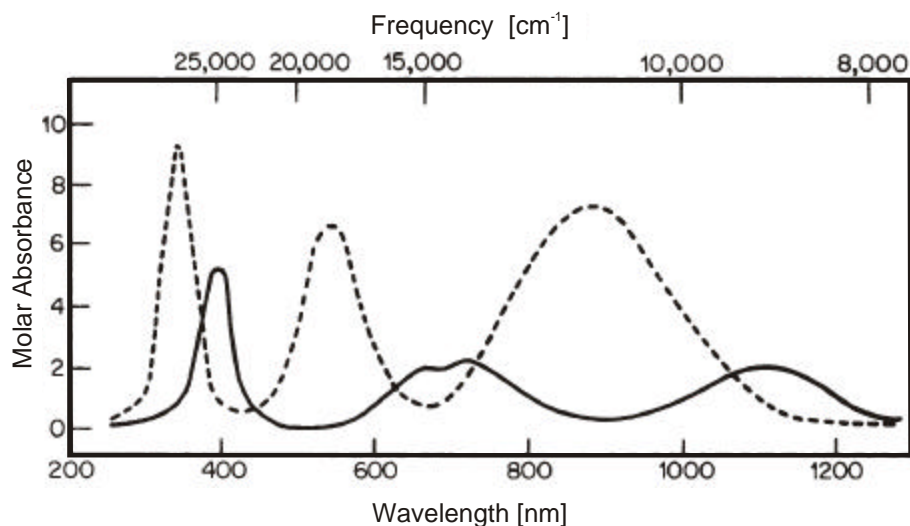


Figure 19. **Absorption spectra of octahedral nickel(II) complexes.** Solid line corresponds to the $[\text{Ni}(\text{H}_2\text{O})_6]^{2+}$ and the dash line to the $[\text{Ni}(\text{en})_3]^{2+}$ (Cotton, 1972).

Moreover, DNA molecules disappear much earlier from the bulk solution (Figure 18, F). Figure 18 F shows that at Ni^{2+} concentration 2.4 mM the number of molecules in the focal volume reduces to less than 2.5 % of its value in bulk solution.

These findings compare well to the result of AFM measurements of an efficient attachment of the DNA molecules at the same Ni^{2+} concentration ($c=2.5$ mM). Comparing our AFM, FCS and FCCS experiments, we conclude that the addition of Ni^{2+} induces an effective sedimentation of the DNA molecules from the bulk solution onto the surfaces. Therefore, for the AFM experiments, not the concentration, but rather the total number of DNA molecules in the DNA solution is the important quantity.

Immobilization of the DNA molecules for the AFM investigation probably occurs during the first drop in the particles number (Figure 18, E). However, Ni^{2+} concentrations larger than 4 nM influence the conformations of the DNA molecules as well. This phenomenon cannot be fully explained by our experiments and needs further investigations.

To exclude a possible influence of the glass surface on the DNA molecules sedimentation when working with rather diluted DNA solution we conducted experiments using silanized glass (2.1). However, usage of untreated or silanized glass surfaces did not show any significant difference.

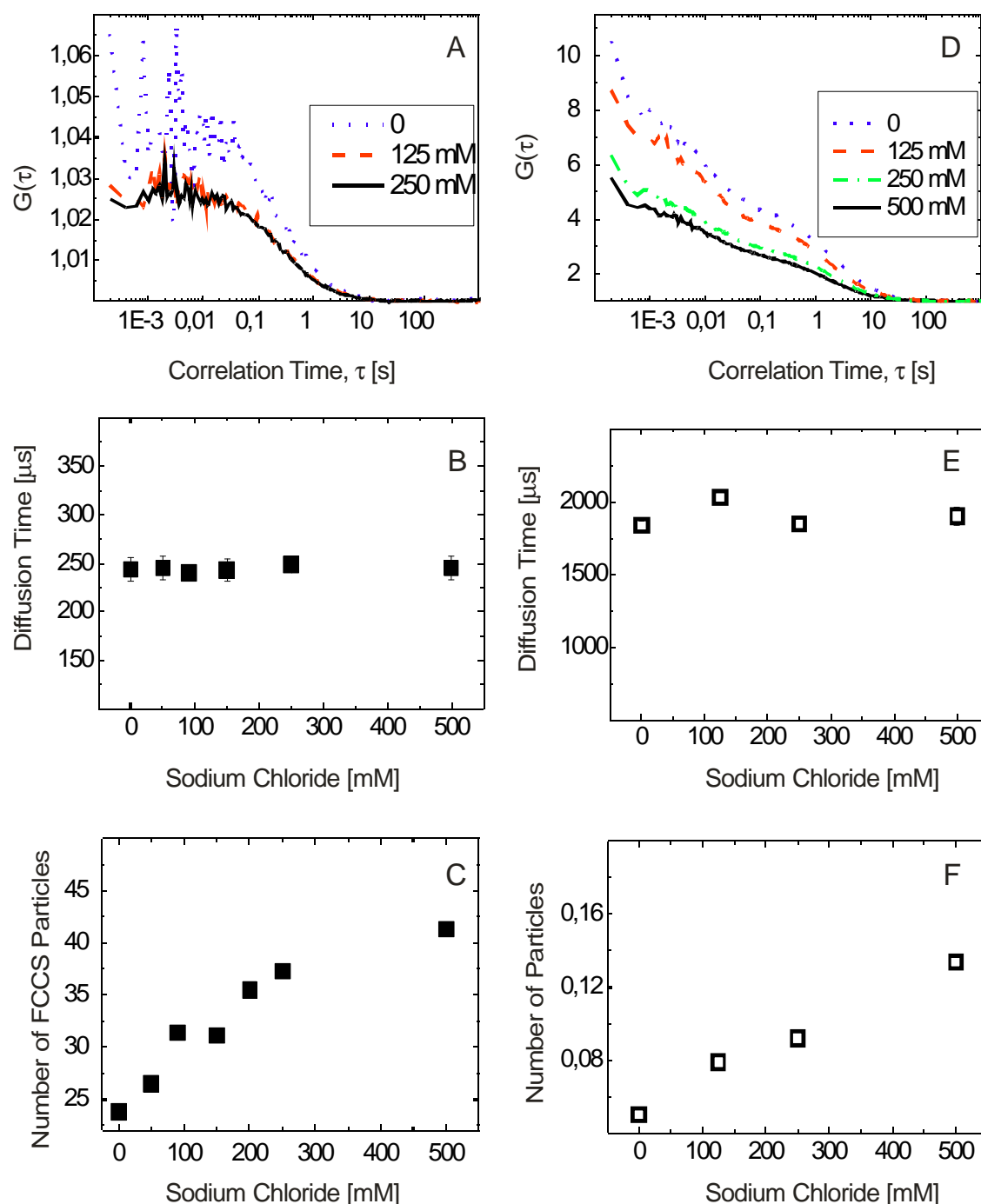


Figure 20. **Dependence of the DNA diffusion time and numbers of particles as a function of the addition of sodium ions studied with FCS and FCCS.** FCCS autocorrelations curves of 36 bp DNA (A), diffusion time (B) and number of particles (C) as a function of the sodium chloride concentration. FCS autocorrelations curves of 440cy5 DNA (D), diffusion time (E) and number of particles (G) as a function of sodium chloride concentration. Zero concentration indicates the usage of pure AFM deposition buffer.

Nevertheless, another explanation of the reduction of the number of DNA molecules in the confocal volume is possible. An absorption spectrum of $[\text{Ni}(\text{H}_2\text{O})_6]^{2+}$ has a peak in a range between 600-800 nm (Figure 19) that overlaps exactly with the emission peak of Cy5 (3.5.3). This fact may reduce detection of the emitted fluorescence photons of the

Cy5. Therefore under high concentration of Ni^{2+} the signal-to-noise ratio gets worse (see cyan autocorrelation curve in Figure 18, A). However, this effect does not exclude the possibility of DNA sedimentation. Definitely, from our preliminary experiments we can not conclude about the mechanism of the Ni^{2+} influence on the DNA hydrodynamic properties.

In similar FCS and FCCS experiments we found a different influence of sodium chloride in comparison to Ni^{2+} (see Figure 18 and Figure 20). For both DNA fragments (440 bp and 36 bp) a concentration of sodium ions larger than 500 mM has still no influence on the diffusion time of the DNA molecules (Figure 20, B and E). However, as it evident from Figure 20 C and F, addition of sodium chloride influences the number of particles for both 440 and 36 bp DNA.

An almost linear increase of the number of DNA particles in the focal volume with increasing sodium ion concentration can be traced using both FCS and FCCS. Such an increase in the number of particles suggests that DNA molecules re-adsorb from the surrounding surfaces (glass, sample chamber) as a consequence of the addition of sodium ions (the presence of the ions increases the solubility of the DNA molecules). This finding is in a good agreement with our attempt to immobilize DNA for AFM measurements in AFM buffer with high sodium chloride concentration (data not shown) and confirms earlier experiments that show that addition of monovalent ions reduces the amount of deposited DNA molecules (Bezanilla, 1995). A reduction of the efficiency of the DNA attachment when Na^+ and K^+ ions are present may also partially explained by the high difference in their hydration enthalpy values (Figure 13), in comparison to Ni^{2+} and Mg^{2+} .

In the present study we managed to improve the immobilization of DNA molecules on a mica surface such that they can be scanned reproducibly with AFM. Our AFM investigation on the immobilization of DNA molecules showed an extreme dependence on the pH value of the AFM deposition buffer (2.2). It proved essential to keep the deposition buffer around $\text{pH} \approx 8$ to accomplish an efficient attachment of the DNA molecules. The lowest pH value at which it was still possible to visualize DNA molecules in 10 mM HEPES was 7.9. In order to study any possible conformational changes of the DNA molecules induced by the presence of $[\text{H}^+]$, we performed a series of the FCS experiments varying the pH value. Since FCS traces the diffusion time of the molecules labeled with fluorophore, we performed control measurements to check if the fluorophore maintains the same properties at different pH.

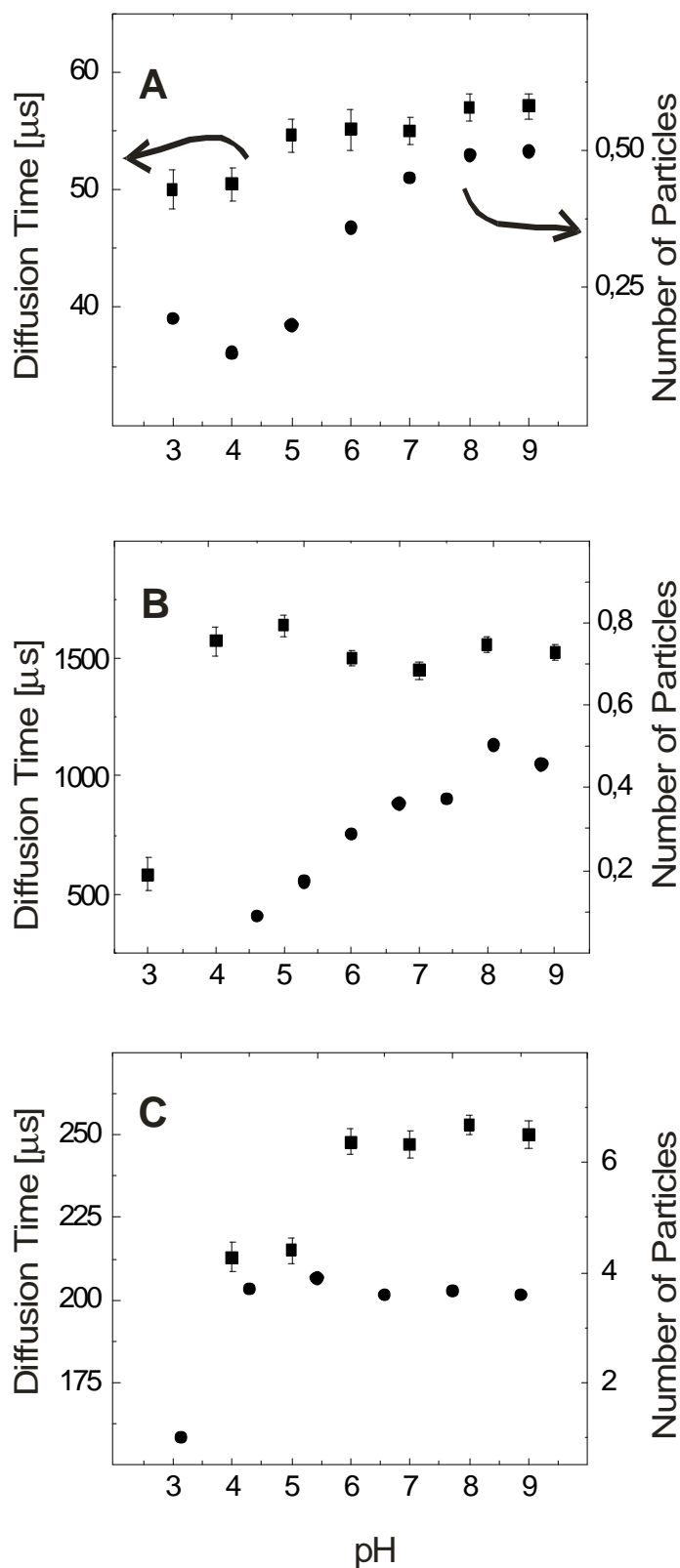


Figure 21. **Influence of the pH value on the hydrodynamic properties of Cy5 and dsDNA studied with FCS and FCCS.** Dependence of the hydrodynamic properties of free Cy5 (A), 440_{Cy5} bp DNA (2.3.2) with the single Cy5 modification (B) and 36 bp (fragment 1 in Table 1) dsDNA (C) on different pH values. ■ - diffusion time [μs], ● number of particles as determined by FCCS. A pH value of 8 indicates pure AFM deposition buffer.

The measurements of the Cy5 show that the number of particles and diffusion time is pH dependent (Figure 21, A). The FCS study of the diffusion time of the 440_{Cy5} fragment (Figure 21, B) shows the same tendency.

However, a difference in quantum efficiency of Cy5 under different pH cannot be excluded. At the same time, different pH values do not significantly influence the values of the diffusion time of 440_{Cy5} DNA measured with FCS (Figure 21, B) and it stays rather stable within the pH range of 4-9.

FCCS measurements of the short 36 bp DNA fragment labeled with two different fluorophores (fragment 1, Table 1) show that within a pH range of 6-9 the DNA diffusion time does not change significantly (Figure 21, C). The importance to keep the pH of the AFM deposition buffer around pH 8 for the DNA molecules immobilization might be explained by the fact that under higher pH conditions the phosphate backbone of the DNA molecules is more expanded, enhancing negative charge of the molecules. This charge may be exploited by the divalent Ni²⁺ or Mg²⁺ to further increase the adsorption of the DNA molecules on the negatively-charged mica surface.

In summary we have developed a protocol to immobilize biomolecules for AFM investigations. Such biomolecules as linear and circular DNA, different types of proteins and DNA-protein complexes can be immobilized for AFM investigation in liquids following that method. In our experiments we showed that time-resolved measurements with AFM are also possible using developed method of the surface immobilization of the biomolecules in liquids. The role of Ni²⁺ and Mg²⁺ the mechanism of the DNA immobilization on the mica surface is discussed. Additionally, influence of the nickel, sodium ions as well as H⁺ on the DNA molecules in bulk solution was studied using FCS and FCCS.

4.2 INVESTIGATION OF INTACT DNA MOLECULES USING AFM

The sizing of DNA molecules is one of the most widely used analytical approaches in biochemistry and molecular biology. Most of the DNA sizing today is performed by gel electrophoresis, where the migration of DNA molecules in a gel induced by an electric field can be used to size DNA molecules. A combination of the appropriate gel type, gel dimensions and applied electric field provides the possibility to examine an extensive range of molecules weights. However, the precision of such techniques is rather limited.

AFM, alternatively, gives the possibility of a real space measurement of the dimensions of single molecules, which are adsorbed to a surface. In the last decade DNA molecules immobilized on the surface were extensively studied by AFM. For instance, the analysis of the DNA contour length, L_{DNA} , measured in propanol shows that in its fully dehydrated state DNA molecules exist in A-form (Hansma, 1993). Shortening of L_{DNA} was also monitored after rinsing of the DNA with 30% ethanol after sample deposition (Fang, 1999) or by imaging of the dried DNA samples (Rivetti C, 2001). Transition of the DNA molecules from B- to A-form was also shown by measuring of L_{DNA} on a cold surface (Feng, 2000). In addition, salt-induced transition of the DNA molecules from B- to Z-form was also detected using AFM (Gonzalez, 1998; Han, 1997; Sheridan, 1999). Especially, the application of AFM to the structural analysis of DNA has advanced and the observation of novel nanostructures such as G-wires was only possible by AFM imaging (Marsh, 1995). Moreover, scanning of DNA molecules in the dehydrated state in propanol (Hansma, 1995) or of DNA immobilized on a supporting cationic lipid bilayer (Mou, 1995) yields very high special resolution of the DNA molecules, which makes the visualization of a single helical pitch possible.

Additional to the apparent L_{DNA} , parameters as the mean-square end-to-end distance, $\langle R^2 \rangle_{2D}$, and the persistence length of the DNA molecules, P_{DNA} , can be detected from the AFM images. The stiffness of the DNA chain is described by its P_{DNA} . Typically the P_{DNA} of polymers like DNA is measured using transient electric birefringence (Mills, 1999), transient electric dichroism (Bradley, 1972; Schellman, 1995), by electrophoretic analysis of the rates of the ligase-catalized cyclization of DNA (Taylor, 1990b) or by mechanical stretching of the dsDNA (Bouchiat, 1999; Bustamante, 1994). An advantage of the determination of the P_{DNA} from the AFM images is that the presence of molecular agglomerates or DNA unhomogeneities can be easily detected. The P_{DNA} measurements of single molecules and even of different regions of a single DNA molecule can be performed. But on the other hand there are some disadvantages of the P_{DNA} evaluation using AFM. To begin with, AFM visualizes only molecules that are immobilized on the surface and can not distinguish between an intrinsic conformation of the DNA molecules and a trapped conformation introduced by the immobilization routine

(discussed in previous chapter). Additionally, because of the large amount of possible molecular structural configurations, a large number of DNA molecules is needed to yield statistically significant $\langle P_{\text{DNA}} \rangle$ values. The P_{DNA} of DNA molecules was intensively studied using AFM and other methods and the values obtained by different methods vary considerably. For the review see (Hansma, 1997).

In this chapter we report on our AFM study of intact DNA molecules of different lengths. They were generated by different methods and purified using different protocols. All measurements described in this chapter were performed using the same immobilization protocol for the DNA molecules immobilization, as described in detail in the previous chapter (4.1).

4.2.1 Measurements of L_{DNA}

Different DNA probes at concentrations of 1-3 nM in AFM deposition buffer (2.2) were immobilized on a mica surface following a common deposition protocol (4.1.1). The DNA fragments were prepared following different methods (2.3.2). A 41_{Hybr} dsDNA fragment was produced by annealing of complementary strands (3.1.1). A 231 bp DNA fragment was produced using two different methods: by the digestion of DNA with restriction endonucleases (2.3.2) and by PCR (3.1.2). 368 bp, 392 bp, 538 bp and 1060 bp DNA fragments (2.3.2) were prepared using PCR (3.1.2). Synthesis of the 440_{Cy5} fragment was accomplished using PCR (3.1.2), where one of the primers carried Cy5 label on its 5'-end (2.3.2).

For quantitative analysis, the AFM images were flattened using Nanoscope software and home-written software 'Look' (A. Knoll, LS Physikalische Chemie II Universität Bayreuth) and no further filtering was applied. For the determination of L_{DNA} we used the software DNACalc6 (3.4.2). Only molecules that were entirely imaged in the chosen scan area were used. Molecules overlapping with others were disregarded.

On Figure 22 we see the typical AFM images of 41_{Hybr} (Figure 22, A), 231_{ARS} (Figure 22, B), 231_{PCR} (Figure 22, C), 368 bp (Figure 22, D), 392 bp (Figure 22, E), 440_{Cy5} (Figure 22, F), 538 bp (Figure 22, G) and 1060 bp (Figure 22, H) DNA fragments. As depicted in Figure 22 A, for the 41 bp DNA fragment under investigation no elongated objects were observed with an expected apparent L_{DNA} of ~13 nm (calculating 0.34 nm/bp, Figure 1). On the AFM images such short dsDNA molecules are looking like globular objects (Figure 22, A) and a contour length can not be determined.

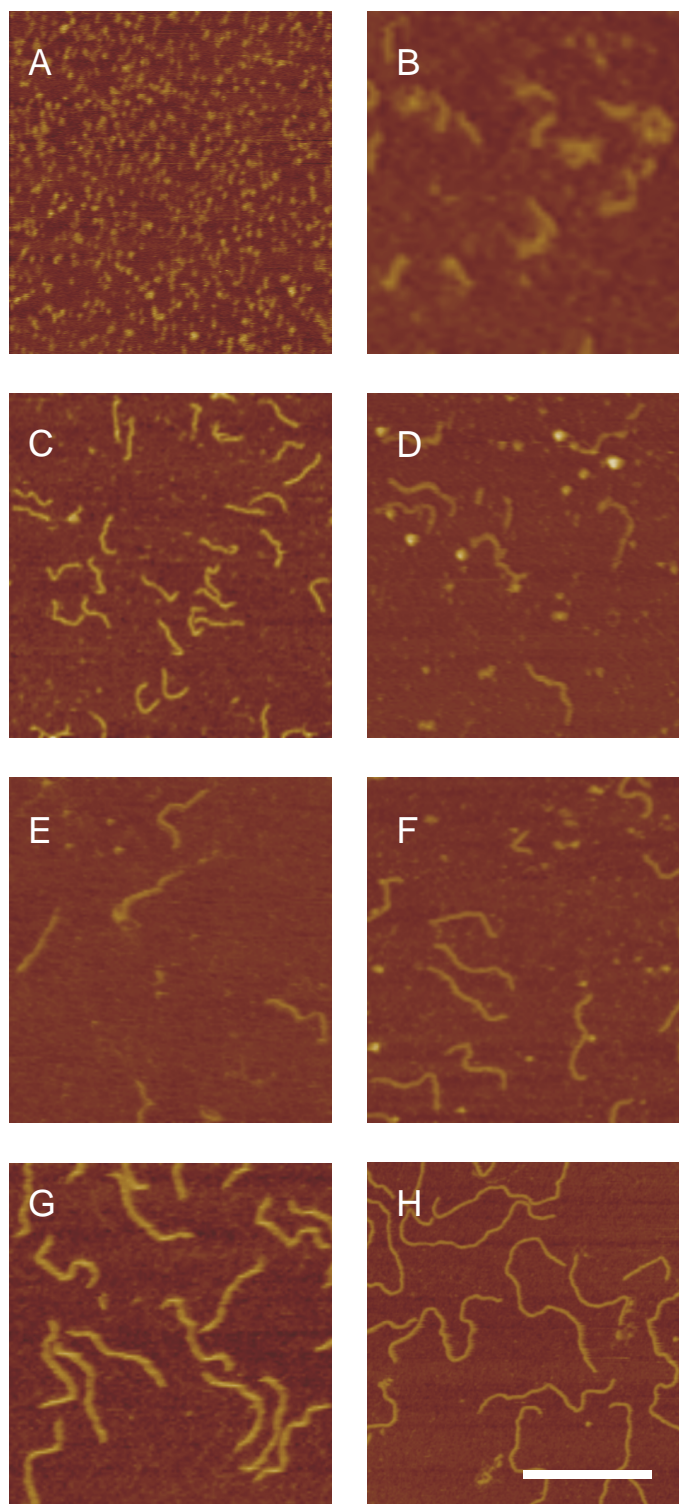


Figure 22. **AFM images of DNA molecules of different length and different preparation and purification routines.** (A) 41 bp DNA; (B) 231_{ARS1} fragment; (C) 231 bp DNA prepared using PCR; (D) 368 bp PCR product purified form agarose gel; (E) 392 bp PCR product purified form agarose gel; (F) 440 bp DNA fragment with Cy5 modification; (G) 538 bp PCR fragment; (H) 1060 bp PCR fragment (scan size 500 nm, bar corresponds to a 200 nm data scale, in **A** z range is 5 nm, in **B-H** - 10 nm).

Evidently, when the dimensions of the molecules are comparable to the size of the scanning tip, we can not distinguish between elongated or globular objects using AFM. The appearance of the 41 bp DNA molecules as globular objects in our AFM images is in a good agreement with similar experiments on 50 bp DNA reported by Hansma *et al.* (Hansma, 1996b).

All others DNA fragments under investigation *do* appear as elongated objects in the AFM images (Figure 22, B-H). L_{DNA} could be directly determined from the corresponding AFM images. For a comparative analysis of the L_{DNA} of the different DNA fragments histograms were generated. Figure 23 presents examples of such histograms for 440_{Cy5} bp, 538 bp and 1060 bp DNA fragments. All these DNA molecules were generated using PCR (3.1.2). The histograms of L_{DNA} for the 440_{Cy5} dsDNA (Figure 23, A) shows a single peak at 141 ± 14 nm. Analysis of the 538 bp L_{DNA} distribution (Figure 23, B) shows that the 538 bp PCR fragment has two fractions: one with a L_{DNA} of 172 ± 19 nm corresponding to the 538 bp DNA fragment and a fraction with a L_{DNA} of ~ 344 nm indicated by the small second peak in the distribution (marked with an arrow in Figure 23, B). The length corresponds to molecules with the double contour length. However, the L_{DNA} distribution of the 1060 bp DNA fragment contains already three fractions of different lengths (Figure 23, C). The most significant fraction with a contour length of 355 ± 39 nm corresponds to the 1060 bp DNA, but the origin of other two fractions (marked with arrows in Figure 23, C) remains unclear. Such impurities in the DNA sample were not visible on the control gel electrophoresis after PCR reaction (3.1.2). For a comparison of the L_{DNA} values of different DNA sequences we have applied Gaussian fit to the peaks in the histogram (see solid lines in the Figure 23) instead of the arithmetic mean L_{DNA} value (1.1). The evaluation of $\langle L_{DNA} \rangle$ is significantly influenced by DNA impurities or limited resolution of the AFM images. Having evaluated the L_{DNA} and the number of base pairs in the corresponding DNA fragments we were able to calculate a value of the DNA helical rise. For the comparison of our experimental data with the theoretically expected, we calculated the L_{DNA} for the DNA fragments based on crystallography (Watson, 1953) and NMR (Ulyanov, 1995) data.

A summary of the structural analysis of all intact DNA molecules from the AFM images is presented in Table 3. An analysis of L_{DNA} of longer (>230 bp) DNA fragments shows that the data obtained using direct sizing of the molecules with AFM are in the good agreement with the theoretically calculated values (Table 3).

The level of precision of the AFM sizing seems reasonable given the potential error introduced by the finite size of the AFM tip. This error is particularly relevant when short molecules are investigated (Figure 24, B).

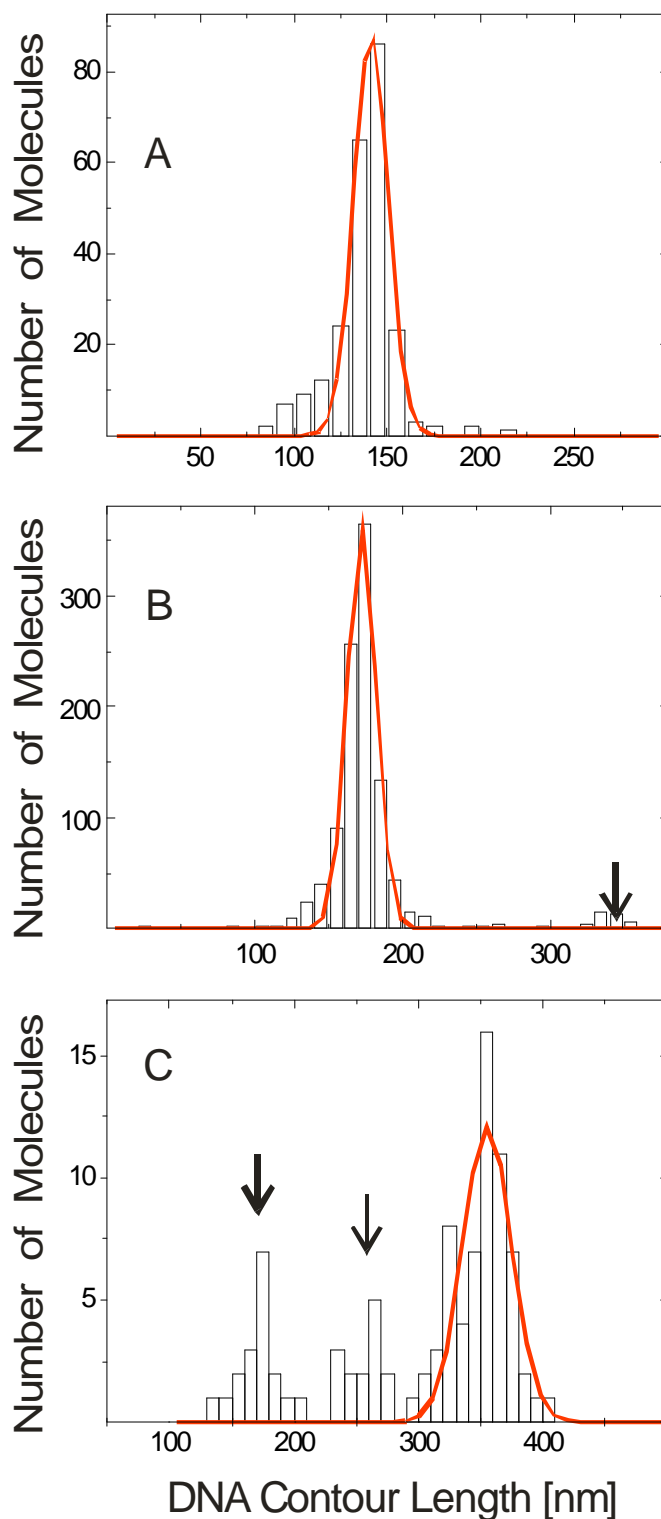


Figure 23. **Contour length distribution of three DNA samples as determined from the AFM images.** Contour length distribution of the 440_{Cy5} bp (A), 538 bp (B) and 1060 bp (C) DNA molecules. Lines correspond to a Gaussian fit of the DNA contour length distribution.

The L_{DNA} values obtained in our measurements are systematically lower than the expected values measured with X-ray assuming B-form DNA (Watson, 1953) and are

closer to the dimensions determined for the B-DNA using NMR (Ulyanov, 1995). The experimental values for the apparent L_{DNA} are about 7% smaller (black squares in Figure 24, A) than theoretical values calculated for a B-DNA with a helical rise of 0.34 nm/bp obtained by X-ray crystallography (solid red line in Figure 24, A) (Watson, 1953) and 3% larger than calculated from a helical rise of 0.318 nm/bp obtained by NMR (solid blue line in Figure 24, A). Smaller L_{DNA} values could be partially explained by the movements of the molecules (Hansma, 1997). Probably, a loose attachment of the DNA molecules induces a terminal detachment of the DNA ends. The analysis of the different DNA fragments shows that the mean DNA helix rise as determined by our AFM experiments is 0.32 ± 0.01 nm/bp. This value is not DNA length dependent and is closer to the value obtained by NMR measurements (Ulyanov, 1995) as to the ones obtained by X-ray crystallography (Watson, 1953).

DNA length, bp	L_{DNA}^* , nm	σ^{**} , nm	Helical rise, nm/bp	L_{NMR}^{***}	$L_{X-ray, nm}^{****}$
231 _{PCR}	75	13	0.33	74	78
231 _{ARS1}	61	12	0.26	74	78
368	110	19	0.30	117	124
392	118	16	0.30	125	132
440 _{Cy5}	141	14	0.32	140	149
538	177	12	0.32	171	181
1060	355	24	0.34	337	358

Table 3. **DNA contour length as determined from the AFM images.** The values of the DNA apparent contour length, L_{DNA} , and the standard deviation from the Gaussian fit of the L_{DNA} distribution. **standard deviation, *** L_{NMR} and **** L_{X-RAY} are calculated values for the expected contour length of DNA molecules with 0.34 nm/bp (Watson, 1953) and 0.318 nm/bp (Ulyanov, 1995) correspondingly.

Interestingly, the deviations introduced by the tip dimensions for both the helical rise and the P_{DNA} is larger for short molecules than for longer DNA (Figure 24, B). The AFM measurements of DNA molecules purified following different purification protocol the purification following spin chromatography (Figure 22, C, F-H) is much more efficient than purification of the DNA from an agarose gel (Figure 22, D, E). Additional improvements in the purity of the DNA samples were achieved by eluting the PCR product (in the last step of the DNA purification) with elution buffer filtered additionally by using 3 kDa filter or eluting of the PCR product directly using AFM deposition buffer.

4.2.2 Determination of $\langle R^2 \rangle_{2D}$ and P_{DNA}

For the determination of the persistence length, P_{DNA} , we analyzed the same AFM images as for the L_{DNA} analysis (Figure 22, B-H). From the AFM images we were able to measure the mean square end-to-end distances $\langle R^2 \rangle_{2D}$ of the DNA molecules. Using both $\langle R^2 \rangle_{2D}$ (Table 4) and L_{DNA} (Table 3) determined in our experiments one can calculate the P_{DNA} of the DNA polymer chain, i.e. the distance over which the orientational correlations along the DNA molecule persist. P_{DNA} is a local feature of the polymer chain that typically correlates with its stiffness.

P_{DNA} was calculated using formula (1.1, equation 1) as described earlier (Rivetti, 1996). In Table 4 the results of the mean square end-to-end distance and P_{DNA} analysis of the seven different DNA fragments are presented.

DNA length, bp	$\langle R^2 \rangle_{2D, nm^2}$	se , nm	$\langle P_{DNA} \rangle$, nm	σ , nm
231 _{PCR}	4128	164	37	9
231 _{ars1}	2907	200	39	13
368	8038	301	40	12
392	8646	700	36	10
440 _{cy5}	11443	333	36	9
538	15371	358	36	8
1060	42931	2000	39	6

Table 4. **Experimental values of mean square end-to-end distance and the persistence length of DNA molecules of different length as determined from AFM images.** se – corresponds to standard error and σ - to standard deviation.

According to Rivetti *et al.* (Rivetti, 1996; Rivetti, 1998) the value of P_{DNA} indicates the state of equilibration of the molecule on the mica surface. With AFM it is inherently impossible to distinguish between the intrinsic conformation of the DNA molecule in solution and conformational changes induced by surface immobilization. From our AFM measurements of the six DNA fragments we find that the P_{DNA} of the DNA fragments measured in our experiment is not L_{DNA} dependent (Figure 24, B) and the mean P_{DNA} of the intact DNA molecules is 38 ± 7 nm. This value can be compared to the results by Rivetti *et al.*, who determined the P_{DNA} of undamaged DNA equilibrated on a surface to 52.3 ± 0.3 nm (Rivetti, 1996).

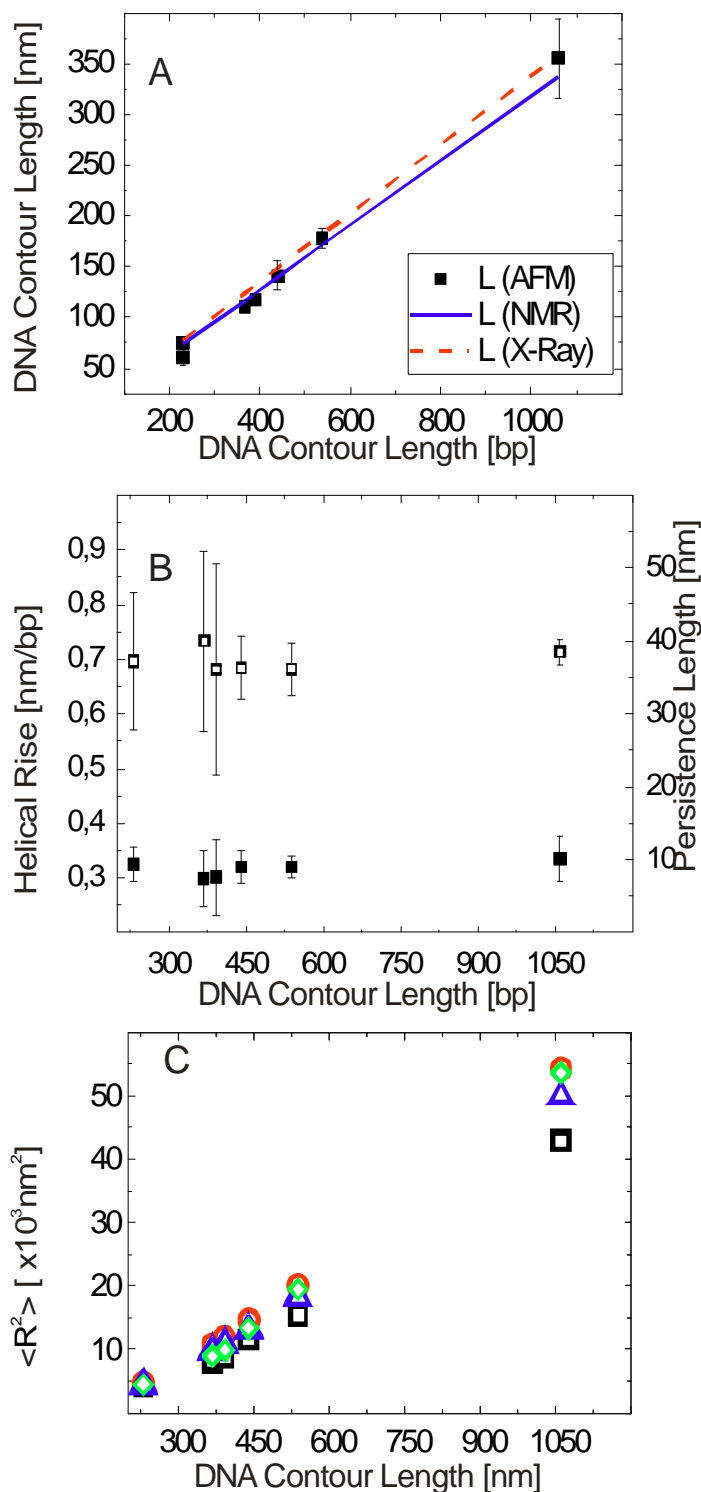


Figure 24. **Comparison of the experimental DNA contour length, mean square end-to-end distances, helical rise and persistence length values with theoretically calculated values.** (A) Red line corresponds to the theoretical DNA contour length where helical rise is 0.34 nm/bp, blue line – to the 0.318 nm/bp. Black circles correspond to the DNA contour length, measured with AFM. (B) Experimental values of the P_{DNA} (empty symbols) and values of the helical rise (filled symbols) as a function of DNA length as determined by AFM. (C) Mean square end-to-end distance as a function of the DNA length. Black squares correspond to the AFM experimental values, red circles - to the calculated L_{DNA} and $\langle R^2 \rangle_{2D}$, where $L=0.34 \text{ nm/bp}$ and $P=53 \text{ nm}$, green squares to experimental L_{DNA} and $P_{\text{DNA}}=53 \text{ nm}$, blue triangles to $L_{\text{DNA}}=0.318$ and $P_{\text{DNA}}=53 \text{ nm}$.

Given their result, one may anticipate that the DNA molecules in our measurements are in an intermediate state of adsorption between trapping and full 2-D equilibrium.

On Figure 24, C we plotted different combinations of the L_{DNA} values versus the mean square end-to-end distances assuming the P_{DNA} to be either 53 nm (Rivetti, 1996) or measured by our experiments - 38 nm. It is evident that our experimental results do not coincide with the theoretically expected. One has to realize, though, that both the particular route of sample preparation (for instance, buffer conditions, temperature) as well as the particular method used for P_{DNA} evaluation can also explain the difference in P_{DNA} . With regard to the former, Bustamante and *coworkers* performed measurements on dried samples, which render a direct comparison to our measurements in a physiological environment questionable. Hansma and *coworkers* measured the P_{DNA} of approximately 500 bp DNA fragments in aqueous buffer on a Ni^{2+} -treated mica surface and found a value of roughly 30 nm (Hansma, 1997), which is in close agreement to our results. However, as stated by the authors of this work, the DNA molecules were only loosely attached to the underlying surface rendering AFM imaging difficult. In the present work, we managed to improve the immobilization of the DNA molecules on the mica surface to an extent that they could be scanned with AFM reproducibly. It proved essential to keep the deposition buffer around $\text{pH} \approx 8$ to realize efficient attachment of the DNA molecules (see previous chapter).

In addition to the matter of sample preparation, a varying content of the deposition buffer and different methods for the P_{DNA} determination make a consistent analysis and comparison of absolute values of the P_{DNA} difficult. In the further scope of this work we used the value of the P_{DNA} obtained in our experiment for the characterization and comparison of the different DNA damage types following the same immobilization protocol and the same method for the P_{DNA} evaluation.

4.2.3 Structural peculiarities of intact DNA molecules

4.2.3.1 *The heights of DNA molecules*

The measured widths of the DNA molecules from the AFM images correlates significantly with the tip radius, which is the so called ‘tip broadening effect’ (Levadny, 1996; Yang, 1993). The heights of the DNA molecules are not tip-radius dependent and can be measured with a high precision using AFM (Hansma, 1988). Assuming that a DNA molecule was a circular cross-section, both the DNA width and the diameter are equal to the DNA height. The first reports about height measurements of DNA molecules from AFM images indicated a diameter of about 0.55 ± 0.15 nm (Rivetti, 1996) and were far from the expected data measured by DNA crystallography.

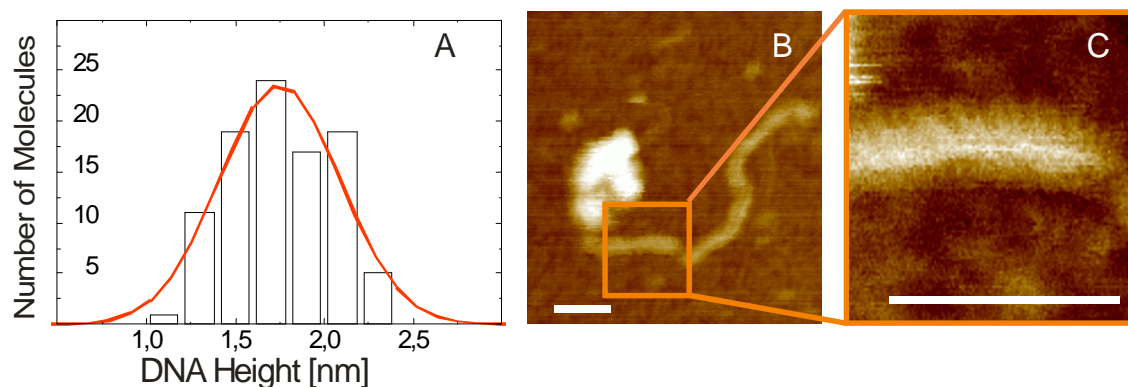


Figure 25. **Determination of the apparent height and DNA double-helix structure from the AFM images.** (A) Distribution of the measured DNA heights. Red line corresponds to a Gaussian fit of the DNA heights distribution. (B) AFM image of the complex of a UV-light damaged DNA with hRPA. (C) Zoom into marked place of the B image. It depicts high resolution AFM image where the details of the double helix could be resolved. Scale bar corresponds to a 20 nm, z data scale, in A is 15 nm and in C 6 nm.

The deviation can be partially explained by the fact that the measurements were accomplished on dried DNA samples (dehydrated DNA molecules) and silicon tips with high cantilever spring constants were used.

We performed measurements of the DNA height using cross section analysis (NanoScope 4.43r8). The average height of the DNA molecules heights was found to be 1.6 ± 0.3 nm (Figure 25, A). This value is in a good agreement with the expected value of 2 nm for the DNA diameter (Figure 1) determined by crystallography measurements (Watson, 1953). As to the broad distribution of the height (Figure 25, A), it could be explained by the fact that sizing of the height values from AFM images of different scan sizes and different scanning parameters was applied. That attributes definitely to a different rate of the tip indentation into the soft sample surface (Knoll, 2003).

It is important to note that such a high value of the DNA height was obtained, when the AFM images we scanned rather ‘soft’ (using the highest possible amplitude setpoint, high gains and a proper driving frequency). Therefore the measured height value can be used to indicate a soft or hard tapping in our AFM measurements.

These values are still lower than the diameter of the hydrated DNA, which is nearly 2.6 nm (Corongiu, 1981). Possibly under the applied scanning parameters the AFM tip is not sensitive to the hydration shell of the DNA molecules.

An application of the cantilevers with high spring constants and unfavorable scanning parameters leads not only to a compression decrease of the apparent DNA heights (Rivetti, 1996), but eliminates the possibility to follow tiny structural changes, e.g. such as caused by small proteins binding to the DNA chain. Varying the set point in AFM

tapping mode operation yields apparent heights of DNA molecules imaged on mica in liquid environment from 0.5 to - 2.2 nm. As it was already shown in (Figure 15) unfavorable scanning parameters can even lead to tip induced movement of the biomolecules (4.1.3). Additionally height measurements of charged biomolecules with AFM in aqueous environment depend on the environment (Rossell, 2003). Therefore we are talking about the apparent heights of DNA molecules in the AFM deposition buffer (2.2) and all further measurement of protein and DNA-protein complex heights were performed under the same conditions.

4.2.3.2 *Double helix*

AFM gives the challenging possibility to observe single biomolecules in their natural environment with a resolution down to a few nanometers. Scientists try to use AFM in order to compare results obtain with, for instance X-ray crystallography, which can only be applied to biomolecules in a crystalline state. AFM allows to analyze the dimensions of single molecules. A significant difficulty in AFM application is the tip broadening effect, which influences the apparent lateral dimension of the objects due to the tip dimensions. Additionally, any movement of the molecules beneath the scanning tip reduces the quality of the AFM imaging (Figure 12, A and Figure 14, F and M). Therefore high quality images of the DNA with AFM can be obtained in propanol. Propanol environment immobilizes the DNA molecules firmly on the surface making a high resolution AFM imaging possible. This renders the single pitch of the DNA helix visible (Hansma, 1995). First reports of high resolution DNA imaging by AFM in aqueous environment with a double helix resolution was reported by Mou *et al.* (Mou, 1995). In their experiment the mobility of the DNA molecules was reduced by immobilization of the DNA molecules on a cationic lipid bilayer. Here we report the first measurements, where the DNA pitch is rendered visible by AFM (Figure 25, C) operating in tapping mode without any additional immobilization of the molecules.

In summary we note that direct sizing of DNA molecules from the AFM images (Figure 22, B-H) shows that the measured values of seven dsDNA fragments yields a mean helical rise of 0.32 ± 0.01 nm/bp and a mean P_{DNA} of 38 ± 7 nm. In further experiments with damaged DNA and DNA-protein complexes we used the same immobilization routine as for the intact DNA. Our AFM measurements also showed that purity of the DNA samples is dependant on its preparation. The separation of the DNA fragments by agarose gel leads to a large scatter of the DNA length and the presence of the globular objects of non-DNA origin. DNA fragments prepared by PCR had the highest purity and were most homogenous in length. The 1060 bp DNA sample generated by PCR contained a rather high impurity of short DNA fragments (up to 30%). These impurities were not visible in the control gel electrophoretic investigations but only in the AFM imaging. Spin column yields the highest level of purity (free from non DNA origin

4.2 Investigation of intact DNA molecules using AFM

contaminations) of DNA samples after PCR. The 538 bp DNA fragments showed the highest purity and narrowest L_{DNA} distribution. Therefore it was often used for further AFM experiments.

4.3 STRUCTURAL AND CONFORMATIONAL MODIFICATIONS INDUCED BY DIFFERENT TYPES OF DNA DAMAGE¹

DNA in living cells is continuously exposed to a broad range of environmental influences of chemical and physical origin. In spite of its highly stable macromolecular structure (Figure 1) DNA is not fully inert. Changes in its primary structure induced by some external environmental factors as well as chemical species within the cell may lead to changes in its secondary structure and as a result may affect the biological function of the DNA (1.2). The fact that similar types of DNA adducts have different biological consequences and that repair proteins recognize chemically non-equivalent damages of the DNA suggest that the adducts influence the secondary structure of the double helix in different ways. In consequence, different effects on the function of the DNA may result.

Conformational changes in the secondary structure of the DNA molecules induced by UV-light (Figure 2) as well as d(GpG) cisplatin intrastrand adduct (Figure 3) have been extensively studied in the past (1.2.1 and 1.2.2). Using gel electrophoretic techniques (Wang, 1991; Wang, 1993), electron microscopy (Husain, 1988), X-ray crystallography (Park, 2002) and NMR (Kim, 1995c; McAteer, 1998) it was shown that the presence of a single CPD (1.2.1) induces an overall bending and unwinding of the DNA double helix. NMR studies demonstrate that 6-4 PP photoproduct induces more significant distortion in DNA than CPD. (Kim, 1995b). However, there are also reports that the presence of a single 6-4 PP did not show any changes in DNA double helix (Mizukoshi, 2001; Spector, 1997). This discrepancy is in contrast to the structure of short DNA duplexes modified with d(GpG) cisplatin intrastrand adduct, in which a shortening of the DNA contour length and a kink in the DNA molecular chain has been observed by several methods (Bellon, 1990; Mizukoshi, 2001; Takahara, 1995; Yang, 1995). Detailed structural information on long DNA molecules containing photoproducts or d(GpG) cisplatin intrastrand modifications is, however, not available.

AFM gives the possibility to study conformational changes of damaged DNA in liquid environment (3.4). The first attempts to study a 260 bp DNA fragment carrying *multiple* cisplatin modifications by AFM have been performed by Onoa *et al.* (Onoa, 1998). They determined a shortening and a compaction of the DNA molecule as well as two strand aggregations as a consequence of the presence of multiple d(GpG) cisplatin intrastrand adducts along the DNA chain. AFM was also successfully applied for the

¹ Parts of this chapter are published in Nucleic Acids Res **30**(12): 2686-2691.

determination of a 100 bp long bubble modification in long DNA molecules (Potaman, 2003).

In this chapter we report the first AFM experiments on long DNA molecules, which carry *multiple* photoproducts at random sites, 368 bp and 392 bp DNA substrates that carry a *single* cisplatin adduct, dsDNA fragment with a defined 6 nt mismatch modification and a dsDNA molecule with a terminal ssDNA tail modification.

4.3.1 UV-light damaged DNA

Before UV-light exposure all DNA solutions were checked for an appropriate purity level using AFM (4.2, Figure 22). In the first set of experiments we used a quartz cuvette for the experiments of the UV-radiation influence onto the DNA molecules. We exposed ~500 μ l of 30 nM DNA solution in a quartz cuvette to a UV-light source (3.3). As UV-light source we used four germicidal lamps at 254 nm (3.3). This wavelength belongs to the UV-C range the intensity of which is very weak in the ambient environment because of its almost complete absorbance by the atmosphere. After an exposition time of 5, 10, 15, 20, and 30 minutes, 30 μ l of the DNA solution were removed, diluted with AFM deposition buffer to a concentration of 1-3 nM and studied with AFM. The DNA molecules were immobilized on mica following the same protocol as for the non damaged DNA (4.1.1). We performed experiments using both 538 bp (2.3.2) and 1060 bp (2.3.2) DNA. Surprisingly neither the 1060 bp DNA (Figure 26, A) nor the 538 bp DNA (data not shown), appear as rod-shaped objects in the AFM images already after 5 minutes of UV exposure (Figure 26, A) in contrast to their structure before UV treatment (4.2, Figure 22, G and H).

The results of an electrophoretic investigation of the same probes of both 1060 bp and 538 bp DNA fragments prior to UV exposure and after UV exposure at different exposition times are presented in Figure 26, B and C respectively. After ethidium bromide staining of the gels it is evident that DNA *is* present in the samples under investigation. In comparison to the undamaged DNA (zero exposition time), the bands broaden and shift upwards, which indicates that the DNA mobility decreases with increasing UV-irradiation time (Figure 26, B and C).

Both, the AFM experiments and the electrophoretic investigation of DNA after UV exposure in a quartz cuvette show (Figure 26) that the DNA undergoes significant structural changes. However, such DNA samples were not suitable for further AFM investigations.

In addition, the exposition of the whole DNA solution volume of ~500 μ l in the quartz cuvette requires a multiple withdrawal of the cuvette from the UV-light source.

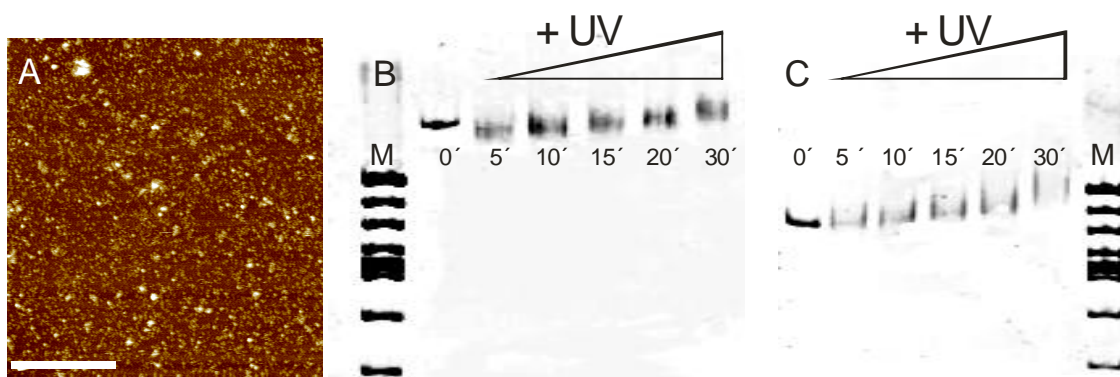


Figure 26. **AFM and gel electrophoretic investigations of the UV-light influence on the DNA molecules in a quartz cuvette.** AFM image of (A) 1060 bp DNA after 5 min exposure to UV-light, scale bar corresponds to 500 nm, z range is 10 nm. Gel electrophoresis of the 1060 bp (B) and 538 bp (C) DNA after exposition to UV-light in the quartz cuvette, M – corresponds to the marker DNA (2.3.3), minutes - to the time of the exposition to the UV-light. In B and C 8% PAGE (3.2.2) with a subsequent ethidium bromide staining (3.2.4) was used.

After each defined time of the UV-light exposition 30 μ l of the DNA solution should be removed from the cuvette (using special syringe adjusted for such small volumes). That definitely interferes with the exact evaluation of the UV-light exposition time due to the numerous displacements of the quartz cuvette from and towards the UV-light source.

One way to avoid this problem is to expose the DNA solutions in UV-light resistant 1.5 μ l Eppendorf tubes with opened lids (3.3). We obtain much better results when DNA solutions of 30 μ l in a concentration of 30 nM were exposed in Eppendorf tubes. A row of these Eppendorf tubes located at equal distance from the UV-light source was exposed to the UV-light source. After different exposition time of 5, 10, 15, 20, 30, 40, and 60 minutes single tubes were withdrawn from the UV-source, the solutions were diluted to the desirable concentration, applied to a mica surface and measured with AFM. The AFM images of the 538 bp DNA molecules being exposed to the UV-light for 15 minutes (Figure 27, A) display the presence of rod-shaped objects that correspond to DNA molecules, which are similar to the images of undamaged DNA before UV-light exposition (Figure 22, G).

Comparison of these two ways to prepare UV-light damaged DNA clearly shows that UV-light irradiation of the DNA solution in a quartz cuvette leads to massive changes in the secondary structure of the DNA. On the other hand, UV-light irradiation of DNA solutions in Eppendorf tubes with open lids provides the possibility to study structural changes of DNA molecules with up to 30 minutes of the UV-light exposure using AFM.

Such discrepancy in DNA damage rate could be explained by the difference between the absorption of UV-light by quartz and plastic.

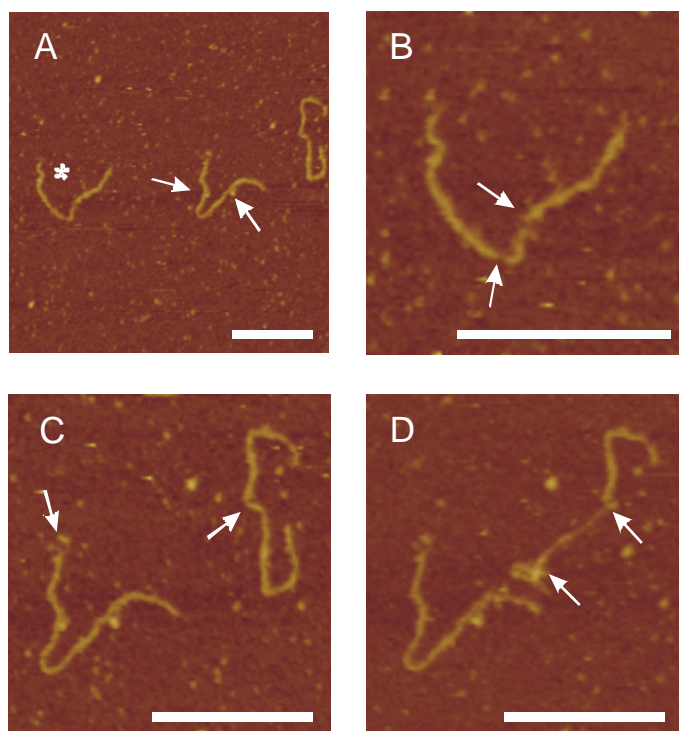


Figure 27. **AFM images of the DNA molecules after 15 minutes of the UV-light exposure in the Eppendorf tubes.** (A) Large scan showing three DNA molecules immobilized on a mica surface, (B) ‘zoom in’ to the left molecule from image A that is marked with an asterisk; (C) ‘zoom in’ the middle and right DNA molecules from (A); (D) the same as in (C), but the following scan, scale bar corresponds to 100 nm, z range is 10 nm.

The walls of the Eppendorf tube fully absorb the irradiation coming from the sides, resulting in effective irradiation that reaches DNA solution equals to the illumination of a single germicide lamp directly above the tube. In the case of the exposition of DNA in the quartz cuvette, solution is illuminated by all four germicide lamps, resulting in fourfold higher efficiency of UV-light irradiation.

Except for the knot-like structures (marked with white arrows in the centre DNA molecule in Figure 27A and Figure 28A) we were not able to observe structural peculiarities introduced by the UV-light irradiation on low resolution AFM images. However, on high resolution AFM images some clear structural differences are visible after exposure of the DNA molecules to UV-light (Figure 27, B-D). For instance, a higher magnification AFM image of the molecule marked by an asterisk in Figure 27 A shows the presence of a ~5 nm long ‘bubble’ on the DNA chain (marked with arrows in Figure 27, B). Such features were never found on undamaged DNA molecules (4.2). Continuous scanning of that structure did not show any significant change in its structure (data not shown).

The most frequent alteration results from a direct adsorption of UV-C light and is a dimerization of the rings of adjacent thymines, forming CPDs or 6-4 PPs (1.2.1). The

presence of such photoproducts can form regions of unpaired bases in dsDNA. Our AFM experiments show that such unpaired regions are not randomly distributed along the DNA chain, which is in a good agreement with the statement that DNA adsorption of the UV-light is sequence dependent and therefore supports the idea about cold and hot spots of the mutagenesis (Parris, 1994).

The high resolution AFM images of the other two DNA molecules depicted in Figure 27 A show the presence of unpaired ends on the left DNA molecule and a sharp kink in the right DNA molecule (marked with arrows at the corresponding positions in Figure 27, C). Moreover, the next scan of the same spot shows significant changes in the structure of the right molecule (Figure 27, D). The structure between the arrows in Figure 27 D has a height of ~ 0.7 nm. The height of the dsDNA measured from the same spot of the same molecule from the previous image (Figure 27, C) was ~ 1.6 nm. The location of the lower part of the right DNA molecule in Figure 27, D has significantly changed in comparison to the previous scan presented in Figure 27, C. In the lower part of the molecule a knot is formed, which was also not present in the previous scan. In the same time, the left DNA molecule in Figure 27 C and D has not changed its conformation. The AFM images of UV-light damaged DNA after 20 minutes of irradiation also depict numerous knot-like structures and sharp kinks in the chain of the 538 bp DNA molecules (see white arrows in Figure 28, A), which are not present prior to the UV-treatment (4.2, Figure 22, G).

Such globular features within the damaged dsDNA chains resemble structures found by Rivetti *et al.* (Rivetti, 1998) of otherwise intact dsDNA molecules with single-stranded gaps. They investigated DNA molecules consisting of two dsDNA fragments connected by single stranded oligonucleotides of various lengths. These molecules form globular features in the ssDNA region similar to the ones found in our experiment. This finding supports the assumption that the globular features along the dsDNA could correspond to the presence of single-stranded regions within the dsDNA after UV-light exposure.

The dynamic AFM measurement (Figure 27, B-D) suggests that the sharp kink in the DNA chain could correspond to a single strand break. The conformational changes of the right DNA molecule shown in Figure 27 C are likely to be induced by the AFM imaging process. In the place of the kink one of the single strands was broken and an instability introduced by the scanning movements of the AFM tip may have led to the changes in its conformation. One end of the broken strand jumps and coils into a knot in the lower part of the DNA molecule and the other end of the broken strand still connects the regions of the complementary intact strand. The formation of the globular object from the ssDNA definitely suggests that under the applied conditions ssDNA regions tend to coil. Formation of the CPDs and 6-4 PPs cannot explain the presence of the

breakage of the molecule into two single strands as a consequence of the UV-light adsorption. The mechanism of single-strand formation due to UV-light treatment might be explained by an indirect influence of the UV light. It is known that water adsorbs UV-light thereby producing radicals (Scharffetter-Kochanek, 2000). When a hydroxyl radical reacts with DNA, a single-strand as well as double strand break may occur (Folkard, 2002; Hieda, 1994; Horiguchi, 2001; Prise, 2000; Wehner, 1995).

From similar images the contour length L_{DNA} and the end-to-end distance $\langle R^2 \rangle_{2D}$ of the 538 bp DNA molecules were determined after UV exposure. After UV irradiation times longer than 30 minutes the determination of the contour length becomes increasingly difficult, because the attached DNA molecules were no longer linear but rather globular in shape (Figure 28, B). AFM images of such DNA samples resemble the ones of the 1060 bp DNA, which have been exposed to the UV-light in the quartz cuvette (Figure 26, A). The development of $\langle R^2 \rangle_{DNA}$, L_{DNA} and on the persistence length P_{DNA} of the 538 bp DNA fragment as a function of UV exposure time is plotted in Figure 28, C-E.

The figure shows that all three characteristic lengths decrease with increasing exposure time (Figure 28, C-E). The systematic decrease of the contour length L_{DNA} as a consequence of the UV-light exposition (Figure 28, C) seems surprisingly on first sight. It may be partially explained by an UV induced destabilization and melting at the termini of the DNA, which is accompanied by the production of single-stranded regions (Figure 27, C). This destabilization may then lead to compaction and length reduction. Additional effects due to a collapse of the DNA molecules carrying a critical density of UV-photoproducts or an influence of the adsorption process cannot be excluded. The decrease of the mean square end-to-end distance with UV exposition indicates an increased elasticity of the DNA molecules as a consequence of the UV-light exposure.

The values for the persistence length P_{DNA} also depend on the UV-exposure time. In comparison to the value of the persistence length for undamaged DNA of 38 ± 7 nm (4.2.2), P_{DNA} gradually reduces as the UV-light exposition time increases. This decrease can be explained by the fact, that after UV-light exposition the DNA molecule undergoes a transition from a 100% dsDNA to a ssDNA-dsDNA construct with increasing fraction of the ssDNA.

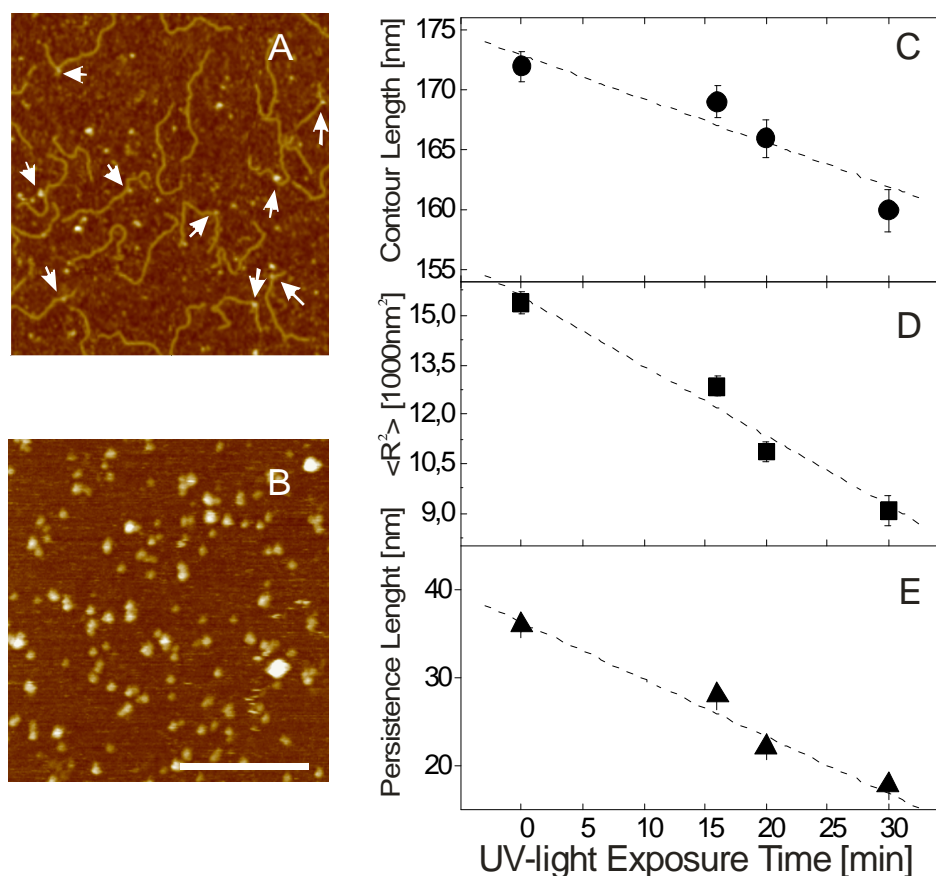


Figure 28. **UV-light influence on the 538 bp DNA exposed to UV-light in Eppendorf tubes.** AFM images of the 538 bp DNA after 20 (A) and 40 (B) min of UV light exposure. Knot-like structures on the DNA molecules appear as a consequence of the UV damage (marked with arrows). In the image of the DNA molecules exposed for 40 min to UV-light (B) rod shaped molecules are not seen (in A and B scale bar corresponds to 250 nm and z range is 10 nm); (C-E) dependence of the DNA contour length, mean square end-to-end distance and persistence length on the UV light exposition time. Circles correspond to the DNA contour length, triangles to the persistence length and squares to the mean square end-to-end distance. In all cases the deposition of the molecules was carried out at in the same way (in AFM deposition buffer, 2.5 mM NiCl₂ and without addition of glutaraldehyde). The lines are linear fits that are used as a guide to the eye (Lysetska, 2002).

Regarding to the experiments performed by Rivetti *et al.* an increase of the single stranded regions in the dsDNA chain was experimentally shown to be responsible for the reduction of both L_{DNA} and P_{DNA} measured with AFM (Rivetti, 1998). It is very difficult to distinguish between the exact positions of the photoproduct even on the high resolution AFM images. Therefore, we calculated the persistence length for the whole DNA molecule, assuming homogeneous elasticity of DNA chain that carries photoproducts.

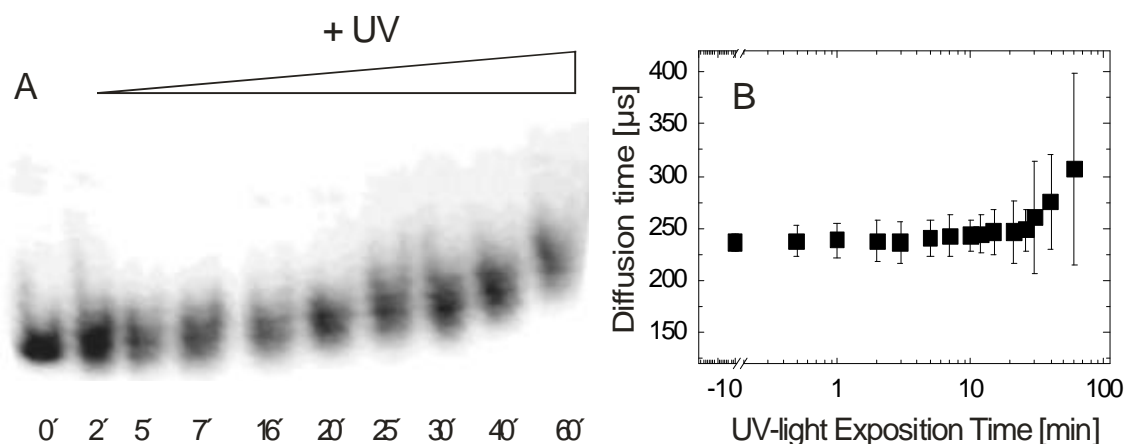


Figure 29. **Effect of the UV-light dose on DNA molecules studied by gel electrophoresis and FCCS.** In comparison to the intact radioactive labeled 538 bp DNA the electrophoretic mobility of the UV-light damaged DNA decreases proportionally to the UV light exposition time (A), In B the diffusion time of a 36 bp DNA fragment as measured with FCCS changes as a consequence of the UV-light exposition time.

Since this is a rather crude assumption, the persistence length in our AFM experiments might be ill defined for this situation. Instead it is better to use the value of the end-to-end distance to characterize the molecular structure.

The AFM measurements show that the presence of unpaired regions and the increase in the number of kinks on the DNA chain increases roughly proportional to the UV light exposure time.

At very high UV dose (UV exposure longer than 30 min) significant damage seems to be produced in the DNA strands, which in turn makes the determination of characteristic lengths of the DNA molecules with AFM impossible. After long exposition to UV-light a critical number of the different damage types, in particular single strand breaks, change the rod shape appearance of the DNA molecules into globular objects in the AFM images (Figure 28, B).

The same 538 bp DNA probes labelled with a radioactive marker (3.1.5) were examined by gel electrophoresis after UV-light treatment in Eppendorf tubes (3.3). Similar to the results for the same molecules exposed to UV-light in a quartz cuvette (Figure 26, C), we find a broadening of the bands and a gradual decrease of the mobility of the DNA molecules as a consequence of the UV irradiation (Figure 29, A). Both effects indicate considerable changes in the shape of the DNA molecules with increasing UV-light dose. This finding is in agreement with the systematic decrease of P_{DNA} and the appearance of kinks and knots in the AFM images of UV damaged DNA. As judged from denaturing gel electrophoresis, there was no significant degradation of the DNA probe under the irradiation conditions applied (Figure 29, A). The number of damaged sites produced by

UV-irradiation is difficult to estimate, since the results are not only influenced by the UV-light doses, but also by the DNA sequence context (Parris, 1994).

To critically test our results obtained with AFM data we studied the diffusion of a 440 bp DNA fragment labeled with Cy5 (3.5.3) using FCS (3.5). The diffusion time of such big molecules is rather high and its residence time in the focus is ~ 2 ms. Because of the bleaching of the Cy5 fluorophore we were not able to follow changes in the DNA molecules introduced by UV-light exposition (data not shown). To decrease the diffusion time and therefore the influence of bleaching, we used a smaller 36 bp DNA fragment (diffusion time is approximately 10 times lower). The molecules were labelled with two fluorophores (fragment I, Table 1) and examined by FCCS. The use of FCCS instead of FCS helps to differentiate the double stranded DNA from the free dye (usually up to 40%) and unhybridized single strands, which might be present in the solution. DNA solutions of equal volume and concentration were exposed to UV-light in Eppendorf tubes with open lids. The samples were withdrawn after 0.5, 1, 2, 3, 5, 7, 10, 12, 15, 21, 26, 30, 40, and 60 minutes and immediately studied by FCCS.

The results obtained are presented in Figure 29, B. They clearly show that the hydrodynamic properties of the DNA are influenced by the UV-light irradiation, too. The mean diffusion time of the 36 bp DNA fragment increases gradually with increasing UV-light exposition time. Both the broadening of the gel bands (Figure 29, A) and the increasing error of the FCCS diffusion time (Figure 29, B) are in good agreement with the AFM result that the UV-exposure introduces a broad variety of structural changes into the dsDNA molecules. We suppose that the formation of the single stranded DNA regions within dsDNA chain due to the UV-light irradiation is the major reason of the reduction of DNA mobility in gel as well as the decrease of its diffusion time measured with FCS.

4.3.2 Bubble DNA

The presence of a few unpaired bases within the DNA chain, a so called ‘bubble’ modification, is a type of DNA damage that can produce a transcriptional frame shift or could cause mutagenesis. Attempts to visualize a bubble modification by AFM have been already performed earlier. In AFM experiments carried out in air by Potaman *et al*, a 100 bp long bubble appeared as 33 ± 5 nm long feature (Potaman, 2003).

In our experiments we were interested to trace the structural changes of a DNA molecule introduced by the presence of a single 6 nt-long mismatch site. The theoretically calculated length of such a bubble is ~ 2.0 nm. Despite this small dimension we were able to visualize the bubble modification (Figure 30, A-D) on a 1000 bp DNA (2.3.4) using AFM.

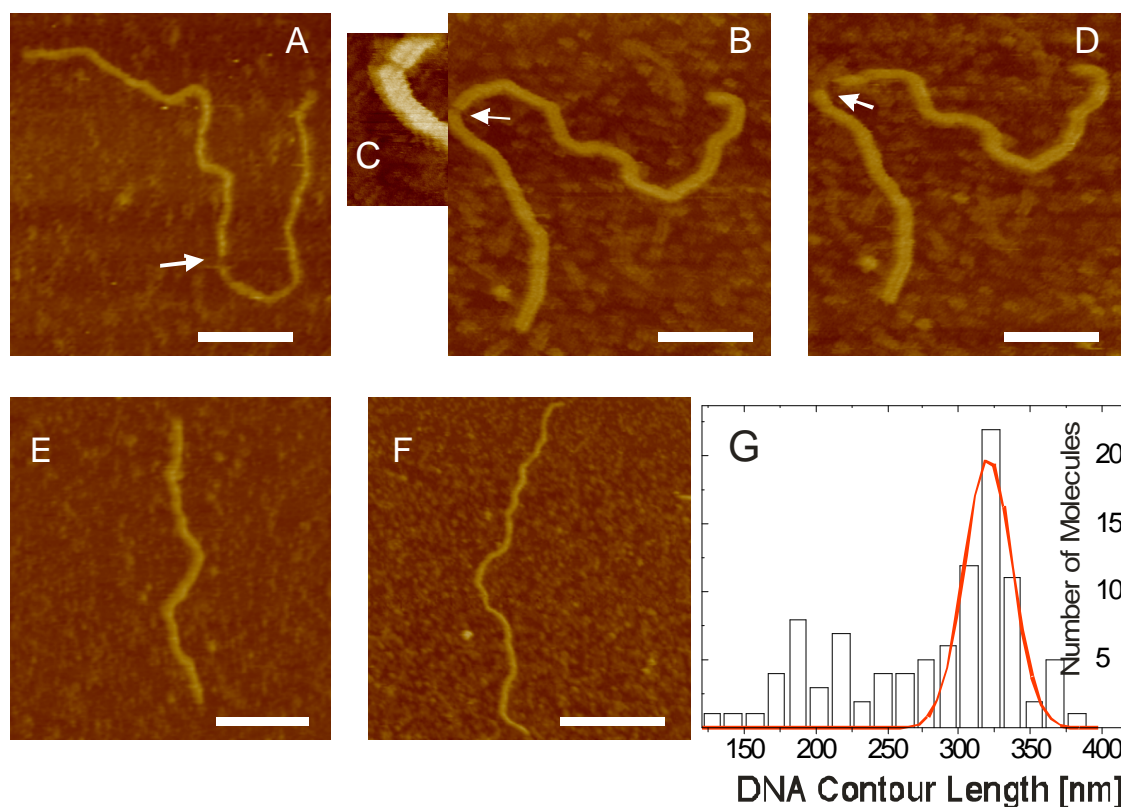


Figure 30. **Investigation of the bubble modified DNA using AFM.** (A) A DNA molecule with a visible mismatch modification site (marked with an arrow); z data scale 10 nm, (B-D) sequence of AFM images of the same DNA molecule as in A (mismatch site is marked with an arrow). (C) zoom into the region of the bubble marked in D with an arrow, scan size 50 nm, z data scale 5 nm, scale bar in A, B and D corresponds to 50 nm, in B and D z range is 10 nm; (E and F) DNA molecules form the same sample but without visible mismatch modification; scale bar corresponds to 100 nm, z range is 10 nm, (G) Frequencies distribution of the molecules' contour length as measured from the AFM images. The red line corresponds to a Gaussian fit to the distribution.

High magnification AFM images show the location of the bubble position within the DNA chain (marked with arrows in Figure 30, A and B). Zooming into the respective part of the DNA molecule (marked with an arrow in Figure 30, B), reveals the details of its structure (Figure 30, C). The apparent length of the bubble is ~ 2.9 nm. Interestingly the bubble dimensions appear much larger on zoomed out image of the same molecule (Figure 30, D). Definitely, the imaging process leads to a further splitting of the DNA strands and enlarges the bubble from 2.9 to 8 nm (see sequence of AFM images in Figure 30, B-D). However, the 'bubble' modification was not visible on all molecules of the same sample (Figure 30, E and F) even at high magnification AFM images (data not shown).

The distribution of the apparent contour length of the DNA molecules modified with the bubble is very wide (Figure 30G). A large fraction of the molecules has a rather short contour length (Figure 30, G). We have not detected the presence of this short DNA

fraction on the control gel electrophoresis (data not shown). To determine an average contour length of 1000 bubble DNA molecules we applied a Gaussian fit to its distribution (marked with a solid red line in Figure 30, G). The measured relevant dimensions of the bubble modified DNA are summarized in Table 5. Note, that the determined contour length is 320 ± 30 nm and corresponds well to B-DNA, but the persistence length is found to decrease from 38 ± 7 nm for undamaged DNA to the 32.8 ± 7.7 nm. Definitely the presence of an only 6 nt long bubble modification in such a long DNA molecule reduces its persistence length by ~15%.

4.3.3 DNA molecules with a single cisplatin modification

It was shown that binding of cisplatin to DNA perturbs the DNA structure, which results in unusual premelting phenomena (Gangulie, 1979), a decrease of the melting temperature (Hermann, 1979; Srivastava, 1978), a decrease of the viscosity (de Pauw-Gillet, 1979; Munchhausen, 1975), an unwinding and shortening (Cohen, 1979; Macquet, 1978; Mong, 1981), changes in electrophoretic motilities of circular DNA (Mong, 1980), changes in UV and CD spectra (Gangulie, 1979; Munchhausen, 1975), and molecular bending (den Hartog, 1985; Mizukoshi, 2001).

The changes in the DNA conformation caused by the binding of cisplatin adduct lead to a significant decrease of the molecular function for cell proliferation. Therefore cisplatin is widely used as an anti-tumor remedy (Rosenberg, 1969). The first attempt to investigate such modified DNA with AFM was performed by Onoa and Moreno (Onoa, 2002). However, the quality of the AFM images reported on therein is rather low and does not allow to trace structural changes introduced by the cisplatin modification of the dsDNA.

In our experiments we used DNA fragments of two different lengths with a single platinum modification that is located approximately in the middle of the DNA molecule. In the Figure 31 A a typical AFM image of 368 bp DNA taken in buffer solution is presented. We could not trace any visible structural changes of the DNA chain due to the presence of the single platinum adduct by AFM. From similar AFM images a direct measurement of the apparent contour length and the end-to-end distance of the DNA molecules was accomplished. The histogram of the DNA contour lengths shows two well separated peaks corresponding to two fragments with distinct contour length (Figure 31, B). The majority of the DNA molecules has a contour length of 112 ± 15 nm, while ~29 % of the molecules have an apparent contour length of 73 ± 25 nm (Figure 31).

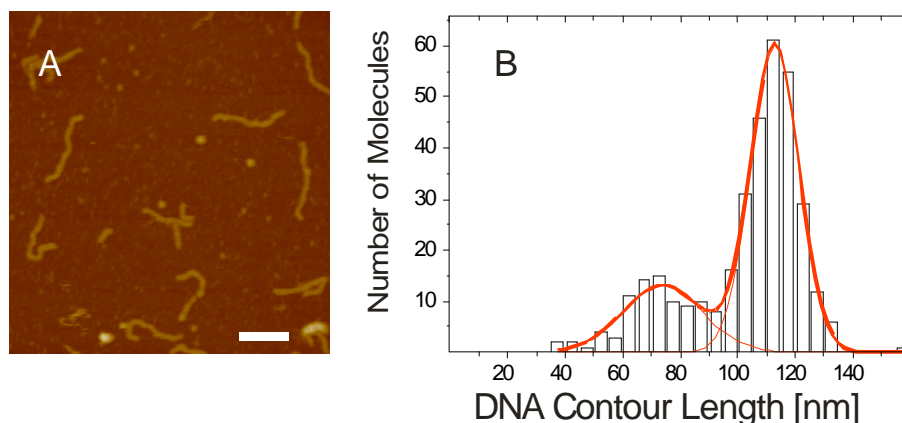


Figure 31. **AFM investigation of DNA molecules modified with a single platinated site.** (A) AFM image of 368 bp DNA molecules modified with a singular pt site and immobilized on mica; scale bar corresponds to 100 nm, z data scale 10 nm; (B) frequencies distribution of the apparent contour length of the 368 bp DNA with Pt site measured from the corresponding AFM images. Solid lines correspond to Gaussian fits of the contour length frequencies distribution.

It is important to note that during the last preparation step of cisplatin modified 368 bp DNA fragment, the molecules were purified from agarose gel (3.2.1) after separation of the DNA molecules in constant electric field according to their molecular mass. Therefore the presence of two fragments of different length should be excluded.

In order to evaluate the persistence length of these two fragments we measured the end-to-end distances of the fragments separately (data not shown). The persistence length of the longer DNA fragment, which corresponds to a 368 bp DNA molecule, is 37.2 ± 2.6 nm.

The same analysis was performed for the 392 bp DNA that carries a single platinum adduct (2.3.4). The histogram of the contour length for this molecule shows a single peak with a maximum at 122 ± 28 nm as determined by a Gaussian fit to the data (data not shown). A summary of the conformational analysis for 368 bp and 392 bp DNA molecules that carry a defined cisplatin adduct measured from AFM images are presented in Table 5.

4.3.4 DNA with a terminal tailed modification

Our attempts to visualize ssDNA were not successful (data not shown), although the resolution obtained with the AFM should not be the limiting factor. Nevertheless, for an investigation of the binding properties of ssDNA binding proteins we tried to construct a DNA substrate with a tailed modification on one of its ends (2.3.4).

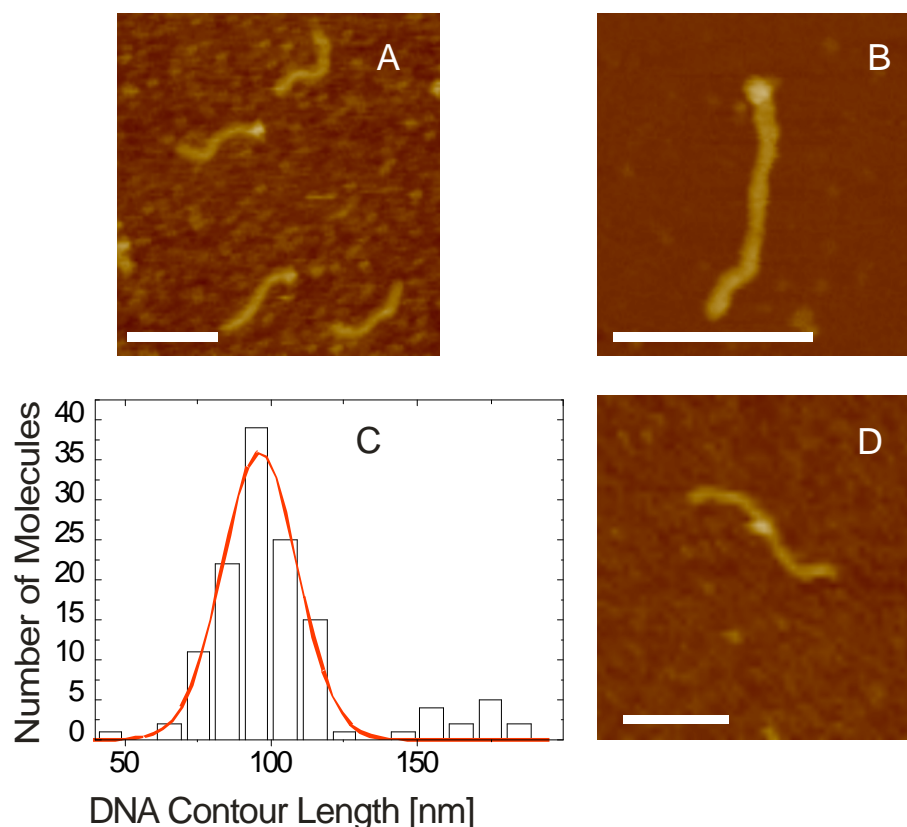


Figure 32. **AFM images of DNA modified with a terminal ssDNA tail.** (A and B) AFM images of the modified DNA immobilized on mica, scanned in buffer; scale bar corresponds to 100 nm, z data scale 10 nm; (C) Frequencies distribution of the contour length of these DNA molecules from the AFM images, solid line correspond to a Gaussian fit of the distribution; (D) AFM image of two molecules forming a single unit, where the ssDNA tails glue together and form a blob in the middle of the unit; scale bar corresponds to the 100 nm, z data scale 10 nm.

In such DNA molecules we know where the ssDNA fragment is located. Typical AFM images of these molecules are presented in Figure 32 A and B. Unfortunately we have not observed the expected structures of a long, ‘relaxed’ ssDNA chain on one end of the double strand. Instead we observe rather big rod shaped objects with a contour length of $\sim 99 \pm 25$ nm, that would correspond to a 290 bp molecule and a globular objects with a height of $\sim 3.0 \pm 0.8$ nm sitting exactly at one end of the dsDNA strands (Figure 32, A and B).

The measured height of the DNA molecules is 1.6 ± 0.3 nm while the blob on the DNA end (marked with an arrow) appears higher. A contour length analysis of these DNA molecules shows the presence of two peaks Figure 32, C. The first one corresponds to a 290 bp DNA molecule while the second corresponds to a DNA molecule with a double number of base pairs.

A detailed view of the structures of double length shows the presence of a globular object in the middle of such a double molecule (Figure 32, D). The terminal regions of

different molecules bind to each other via these ends. According to Rivetti *et al*, the persistence length of the ssDNA is very low, ~ 1.3 nm (Rivetti, 1998). Under the conditions used in our experiments the ssDNA regions of the DNA construct tend to coil.

The results of the evaluation of the dimensions of the DNA molecules from the AFM images are summarized in Table 5. Note, the value of the persistence length for the tailed modified DNA molecules does not change by the presence of the ssDNA region on the molecules' end.

4.3.5 Comparison of the conformational changes induced by different types of DNA damage

A detailed investigation of DNA molecules that carry different types of damage showed the influence of the damage on the appearance of the DNA molecules in AFM images. Comparing all types of DNA damage under consideration the one produced by UV-light introduces the most significant structural changes in the DNA. A summary of the structural analysis of dsDNA after UV-light exposure is presented in Figure 28. The analysis of DNA substrates that carry bubble, platinum adducts and tailed modifications is summarized in Table 5.

DNA modification type	L_{DNA} , nm	$\langle R^2 \rangle_{2D}$, nm ²	P_{DNA} , nm
1000 bp with 6nt 'bubble' modification	320 \pm 30	33439 \pm 23932	33 \pm 8
368 bp with single platinum adduct	114 \pm 15	8416 \pm 4323	37.7 \pm 9
392 Pt with single platinum adduct	122 \pm 14	9327 \pm 4752	38.1 \pm 8
200 bp with 85 nt 'tail' modification	99 \pm 19	6527 \pm 2196	36.3 \pm 9

Table 5. **Measurements of the apparent contour length, the mean end-to-end distance, and the persistence length of the DNA molecules carrying different modifications.**

An exposure of the DNA to UV light introduces different changes to the DNA structure: regions of unpaired DNA of different lengths, sharp kinks, presence of knot like structures, and single strand breaks (Figure 28). Additionally the dynamics of the damage accumulation could be traced with AFM (Figure 29). UV-exposure influences both the apparent contour length L_{DNA} and the persistence length P_{DNA} of the molecules. The structure of the UV light damaged DNA strongly depends on the exposure time. Longer UV-light exposure time introduces increasing DNA damage.

Surprisingly we were able to trace a 6 nt-small bubble modification in the DNA chain using AFM (Figure 30, C). The presence of the bubble modification in the DNA chain reduces its persistence length P_{DNA} , or in other words leads to an increased elasticity of the DNA chain. It is interesting to note that we have observed similar bubble-like structures also for UV-light damaged DNA. Comparison of the AFM images of the DNA from Figure 27 B and Figure 30 A-D shows that UV-light produces bubble-like modification of the DNA, i.e. sites of unpaired bases. A direct measurement of such bubble-structures on the UV-light damaged DNA molecules shows that their length is approximately 5 nm, which corresponds to ~ 14 unpaired base pairs. In comparison to all others types of DNA damage that were under investigation a 6 nt long bubble modification in a 1000 bp DNA fragment reduces its persistence length to 33 ± 8 nm (Table 5). However, the presence of such a bubble does not influence the contour length of the molecule.

On the other hand the investigation of the DNA substrates carrying a single platinum adduct in the DNA chain could not be observed even on the high resolution AFM images. It neither influences the contour length L_{DNA} nor the persistence length P_{DNA} of both the 368 bp and the 392 bp DNA substrates.

For the tailed DNA substrate a globular object at the end of the DNA molecule corresponds to the ssDNA region (Hansma, 1996b). This finding demonstrates that single-stranded regions of the DNA tend to coil under the applied conditions. The same effect may explain the presence of knots on the DNA substrate as a consequence of the UV-light exposure. Any presence of ssDNA regions within the dsDNA chain leads to the decrease of both P_{DNA} and L_{DNA} . A reduction of L_{DNA} in the AFM images caused by the presence and the coiling of ssDNA regions was also detected experimentally by Rivetti *et al.* (Rivetti, 1998). The structural transition due to the presence of the ssDNA regions within dsDNA is in a good agreement with the reduced speed of migration of the damaged dsDNA in gel (Figure 29, A) the increase of the diffusion time as determined by FCCS (Figure 29, B) and the reduced P_{DNA} Figure 28, E) measured with AFM.

4.4 THE ROLE OF XPC-hHR23B AND HUMAN RPA IN THE INITIAL RECOGNITION OF DNA DAMAGE²

DNA integrity is continuously affected by the influence of both external and internal factors (1.2). DNA damage is opposed *in vivo* by the intricate network of DNA repair systems. Among those, one is Nucleotide Excision Repair, *NER*.

NER (1.3.1), is responsible for the removal of deleterious effects of UV-light irradiation as well as of other agents that induce chemical changes in the DNA bases. CPDs and 6-4 PPs (Figure 2) - two major kinds of injuries produced by shortwave UV components of sunlight (1.2.1) - and numerous bulky adducts as cisplatin (1.2.2) are the most relevant lesions subject to *NER* (de Laat, 1999). The mechanism of *NER* consists of several major steps (1.3.1) among which the initial damage recognition of the base damage appears to be an integral component of the enzyme system involved in excision repair.

Human patients deficient in *NER* suffer from *Xeroderma pigmentosum*, *XP*, a hereditary disease characterized by extreme photosensitivity and high predisposition to skin cancer. At the biochemical level, *XP* individuals are impaired in the removal of DNA lesions induced by sunlight (1.3.1). Seven *XP* complementation groups have been identified, representing distinct repair genes *XPA-XPG* (de Boer, 2000; Friedberg, 1995). *XPC* (complexed to *hHR23B*) is the main factor to initiate global genome repair by sensing and binding to various types of DNA lesion (de Laat, 1999).

Human replication protein A, *hRPA* (1.3.2), was also found to have high affinity for damaged dsDNA (Aboussekhra, 1995; Burns, 1996; Clugston, 1992; He, 1995; Lao, 2000; Mu, 1996), which led to the suggestion that it is involved in primary recognition of dsDNA lesions. Interestingly, *hRPA* recognizes a large number of chemically not related lesions as, for instance, UV-light or cisplatin induced distortions in the DNA double helix (1.2.2). Moreover, it has been shown that in both yeast and human DNA repair systems, incision of UV-damaged DNA is absolutely dependent upon *hRPA* (Guzder, 1995; Mu, 1996).

In spite of a large amount of experimental data, the mechanism of recognition of DNA lesions by the repair proteins remains unclear (Batty, 2000b). For *NER* the mechanism of damage recognition must exploit features of damaged DNA other than the chemical nature of the damaged bases, since it removes a variety of lesions that do not share any

² Parts of this chapter are published in *Nucleic Acids Res* **30**(12): 2686-2691.

obvious similarity. One possible explanation is that DNA lesions lead to distortions of the DNA helix with induced thermodynamic instability of the DNA that attracts damage recognition factors (Gunz, 1996).

During the last decades, advances in AFM made it possible to trace conformational peculiarities of DNA-protein complexes (Bustamante, 1999; Guthold, 1999; Kasas, 1997; Pietrasanta, 1999). AFM allows the study of structure-function relationships of the biomolecules avoiding further fixation, contrasting or any additional treatment of the sample (3.4).

In this chapter we present first attempts of AFM investigations of the XPC-HR23B interaction with DNA containing a defined 6 nt bubble modification. Additionally, we report about the first AFM study of the RPA-DNA interaction, where we describe the results of RPA interaction with different DNA molecules: intact molecules, molecules containing a single cisplatin lesion, molecules with a defined 6 nt bubble modification, and UV-light damaged DNA. And at the end of the chapter we report about a first application of the phase imaging mode for the discrimination between DNA and protein molecules in AFM images. All measurements presented here were performed on a MultiMode AFM operated in tapping mode in liquid (3.4.1) following the protocol described in chapter (4.1.1).

4.4.1 XPC-hHR23B binding to bubble modified DNA

The investigation of the architecture of DNA complexes with XPC-hHR23B (1.3.1) is usually restricted by the high aggregation tendency of the protein (Araki, 2001). For our experiment of the XPC-HR23B binding to DNA, which contains a 6 nt bubble lesion (2.3.4), we used a protein that was produced in the group of K. Sugasawa and F. Hanaoka (Japan). In their group a preparation routine has been developed, which yields proteins with a significantly lower aggregation tendency. Since the amount of protein was limited, we performed only preliminary AFM investigations of the XPC-HR23B binding properties to the bubble-modified DNA. For the AFM study, a DNA fragment containing a single 6 nt bubble modification at a concentration of 1 nM, was preincubated with XPC-HR23B for 15 minutes at a concentration ratio of 1:1 in XPC assay buffer (2.2) before it was deposited onto a mica surface (4.1.1). In comparison to the XPC storage buffer (2.2) XPC assay buffer (2.2) did not contain BSA and glycerol. In the AFM images of the damaged DNA with XPC-HR23B we can distinguish between free DNA and elongated objects of different length with significantly higher heights and widths, that gives the impression of DNA molecules fully covered with proteins along the molecules axes Figure 33, A).

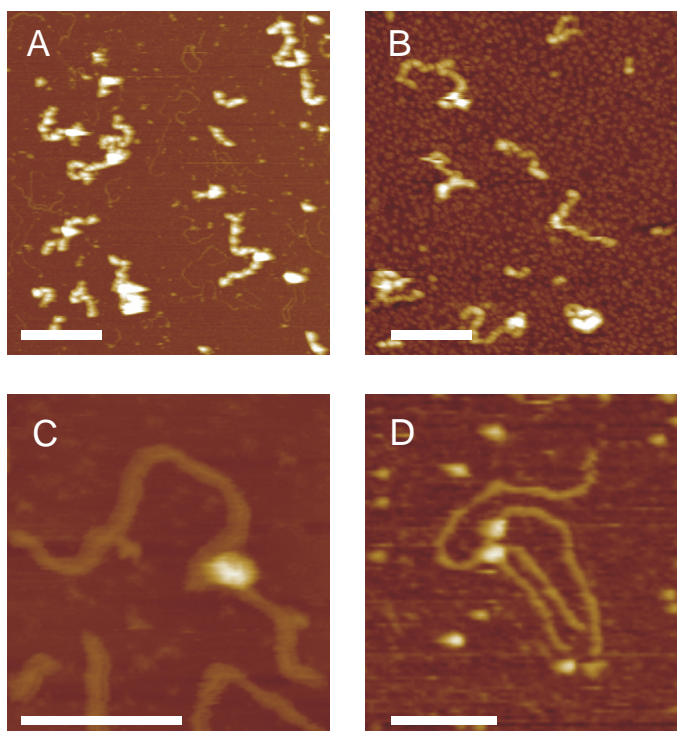


Figure 33. **XPC-HR23B interaction with bubble DNA studied with AFM.** (A) AFM image of the XPC-HR23B complex with bubble modified DNA. Both uncomplexed DNA molecules and thick elongated objects of undefined origin are visible. (B) AFM image of the XPC-HR23B protein without DNA (in A and B z range is 30 nm, scale bar corresponds to 250 nm); (C) Specific binding of the XPC-HR23B to the bubble modification in the DNA molecule (z data scale 20 nm), (D) Complex of two DNA molecules, where XPC-HR23B molecules are sitting on the specifically damaged sites (z range is 10 nm, scale bar in C and D corresponds to 100 nm).

Taking into account a possible XPC-HR23B agglomeration when working with 1 nM concentration of protein we reduced the concentration 10 times. We found that in comparison to hRPA, XPC-HR23B binds with a slightly higher affinity to the 6 nt bubble DNA lesion (Figure 33, C and D).

Because of the small number of AFM images we were not able to perform a statistical evaluation of the DNA contour length after binding to the protein. Nevertheless in the cases of distinct complex formation we do not see any reduction of the contour length due to the binding of the protein. This finding is in good agreement with similar AFM investigation of DNA containing a defined cholesterol lesion (Janicijevic, 2003), where no wrapping or DNA bending was monitored as a consequence of the binding of XPC-hHR23B.

In Figure 33 C we see a bend of the DNA, where the XPC-hHR23B binds to the 6 nt bubble. Recent AFM investigations have demonstrated that the specific binding of XPC-hHR23B to dsDNA containing a defined cholesterol lesion induces changes in the conformation of the DNA (Janicijevic, 2003).

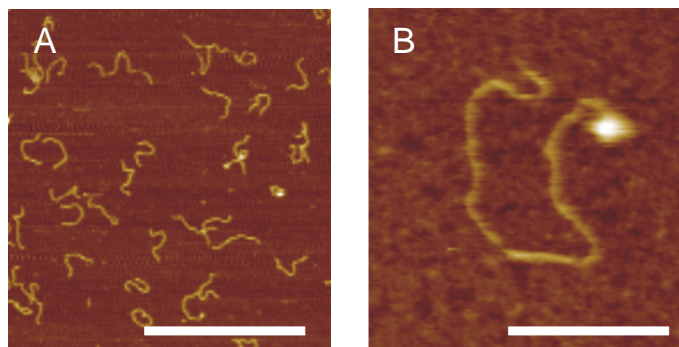


Figure 34. **Interaction of RPA with undamaged DNA.** AFM images do not show distinct complex formation of hRPA with intact DNA (**A**), (5 mM NiCl₂, without glutaraldehyde addition); only random cases of terminal binding were noticed (**B**), (scale bar in **A** corresponds to 500 nm, in **B** – to 50 nm; z range 20 nm, 2.5 mM NiCl₂, 0.1% glutaraldehyde).

Unfortunately, because of the limited number of the AFM images, we cannot draw significant conclusions about the architecture of the DNA-protein complexes.

4.4.2 Complexes of hRPA with intact dsDNA

For AFM measurements undamaged 538 bp DNA (2.3.2) and hRPA (2.4) were preincubated at a concentration ratio of 1:1 or 1:3. We find that reasonable data interpretation of the AFM images becomes difficult at larger excess of protein, because the surface of mica is fully covered with the protein molecules. The preformed complexes were placed on freshly cleaved mica and allowed to equilibrate on the surface for a couple of minutes. Nickel chloride was added to immobilize the molecules on the surface only after this equilibration step (4.1.1) in order not to affect the hRPA-DNA complex structure.

The addition of hRPA to undamaged DNA led to almost no change in the morphology of the DNA (Figure 34, A). Only rare cases of hRPA binding to DNA termini could be observed (Figure 34, B). Moreover, DNA molecules that carry hRPA on their termini do not show any contour length shortening because of the protein binding (data not shown).

In order to exclude a possible influence of the mica surface on the conformation of the DNA-protein complexes (ions, charged surface, etc) we performed a series of experiments where we fixed the conformation of the DNA-protein complexes by glutaraldehyde. 15 minutes after hRPA pre-incubation with 538 bp DNA we added glutaraldehyde (final concentration 0.1% v/v) before deposition of the molecules on mica. 10 minutes after glutaraldehyde fixation a drop of the solution was placed onto mica and after 1 minute of equilibration nickel ions were added (4.1.1). We did not observe any increase in the number of complexes due to the addition of glutaraldehyde.

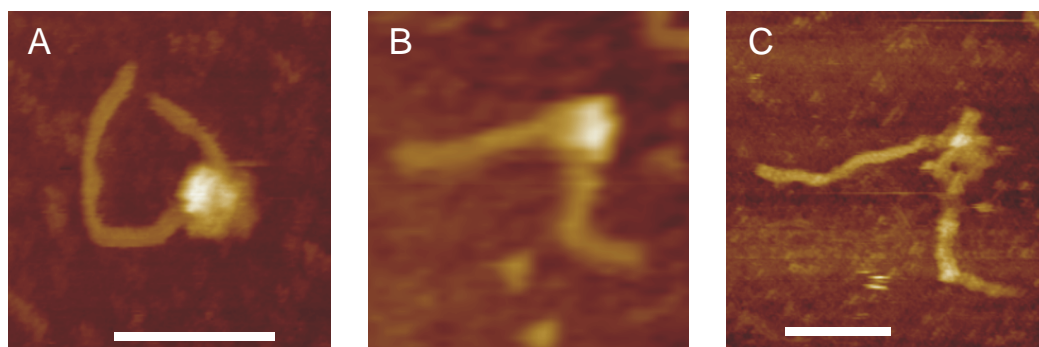


Figure 35. **Interaction of RPA with DNA that contains a single platinum adduct studied with AFM.** (A) AFM image of the complex between RPA and a 398 bp DNA carrying a single cisplatin modification. (B) RPA complexed with a 362 bp DNA with a single cisplatin modification. (C) The same DNA molecules as in B, but the RPA molecule has been removed by the scanning tip (scale bar corresponds to 50 nm, z data scale in A and B is 20 nm, in C – 10 nm).

At higher hRPA concentrations some rare cases of terminal binding of the hRPA to undamaged linear DNA were observed (Figure 34). Since hRPA is known to have a high affinity to single-stranded DNA (Wold, 1997), this finding may be explained by hRPA binding to unpaired nucleotides at the termini of the DNA molecules (Georgaki, 1993). In all our AFM experiments we have never observed binding of hRPA along the chain of dsDNA.

4.4.3 Interaction of hRPA with DNA containing a cisplatin adduct and a 6 nt bubble modification

In our AFM investigations we studied hRPA binding to both 368 bp and 392 bp DNA containing a single cisplatin lesion (2.3.4). For complex formation RPA was mixed with DNA in buffer at a concentration ratio of 1:1. 15 minutes after preincubation at room temperature the DNA-protein complexes were placed onto freshly cleaved mica and imaged by AFM. Within these experiments we did not detect a high affinity of hRPA to the DNA molecules with a single cisplatin lesion. Only rare cases of specific binding of hRPA to the site that carries the cisplatin adduct were monitored. Examples of high resolution AFM images are presented in Figure 35 A and B. It was easily possible to remove the protein from the dsDNA with the scanning AFM tip, which is another indication for a rather weak specific binding of RPA to cisplatin-modified DNA. In Figure 35 C we can see the same DNA molecules as in Figure 35 B, but after removal of the protein. The DNA duplex in Figure 35 C is highly distorted. It can not be excluded that during its residence on the lesion hRPA splits the strands of the DNA in the vicinity of the cisplatin lesion.

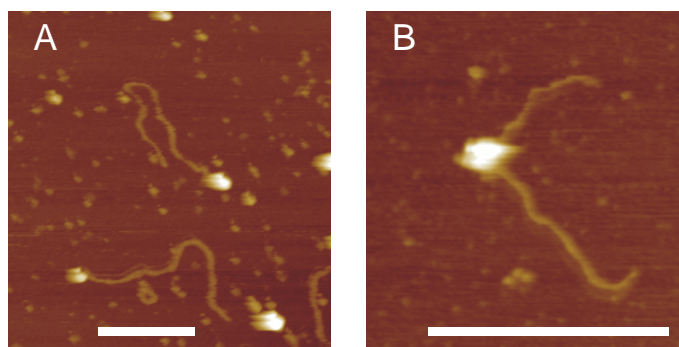


Figure 36. **Interaction of hRPA with DNA containing a single 6 nt bubble modification studied by AFM.** (A) Terminal binding of RPA to the DNA was found to be dominant. (B) A case of the specific binding of the hRPA to the 6 nt bubble modification is visible (scale bar corresponds to the 150 nm, z data range in **A** is 20 nm and in **B** – 10 nm respectively).

Such structural distortion of the DNA double helix were never observed analyzing the structure of cisplatin modified DNA without protein addition (4.2, Figure 22, E). As in the case of unmodified DNA (Figure 34, B) hRPA was found to be bound to the DNA termini rather often (data not shown).

Because of the difficulties in the preparation of the long DNA molecules containing single platinum adducts we were not able to produce a sufficient number of AFM images for statistical evaluation of the DNA contour length. However, in the rare cases of the specific binding of the hRPA to the cisplatin modified DNA we did not notice changes of the DNA contour length as a consequence of the protein binding.

In our AFM investigation hRPA does not exhibit high affinity to bubble modified DNA molecules (2.3.4) either. Terminal binding of the protein has again been found to be preferential (Figure 36, A). These AFM images are very similar to the images of intact DNA and RPA (Figure 34, B). Only rare cases of specific binding of hRPA to the bubble lesion were found (Figure 36, B). Structures similar to those presented in Figure 36 B were never observed in AFM images of bubble modified DNA (2.3.4). Our AFM investigation shows that the presence of a 6 nt bubble in the dsDNA can not be easily recognized by hRPA. The absence of a high affinity of hRPA to DNA substrates that carry a single platinum adduct or a 6 nt bubble modification is in a good agreement with the fluorescence anisotropy measurement reported by Hey *et al.* (Hey, 2001).

4.4.4 Binding of hRPA to UV-light damaged DNA

4.4.4.1 EMSA investigations of hRPA-DNA complexes

The binding of hRPA to UV-damaged DNA was studied both by EMSA and AFM. The EMSA experiments served as a control to verify complex formation. In the EMSA experiments (3.2.3), indicated amounts of hRPA and 1 ng of radioactively labeled DNA

(3.1.5) - after UV-irradiation for different indicated time intervals (3.3) - were incubated in 10 μ l RPA/DNA binding buffer (2.2) for 15 min at room temperature. Samples were loaded on polyacrylamide gels (3.2.2) after addition of the loading buffer without any further treatment of the sample. Electrophoresis was carried out in 0.5xTBE (2.2) as running buffer for 3 h at 10 V/cm and 4°C.

In the set of experiments where DNA with protein were premixed without glutaraldehyde addition we have not seen any complex-formation for both intact and UV-light damaged DNA even under high RPA concentration (Figure 37).

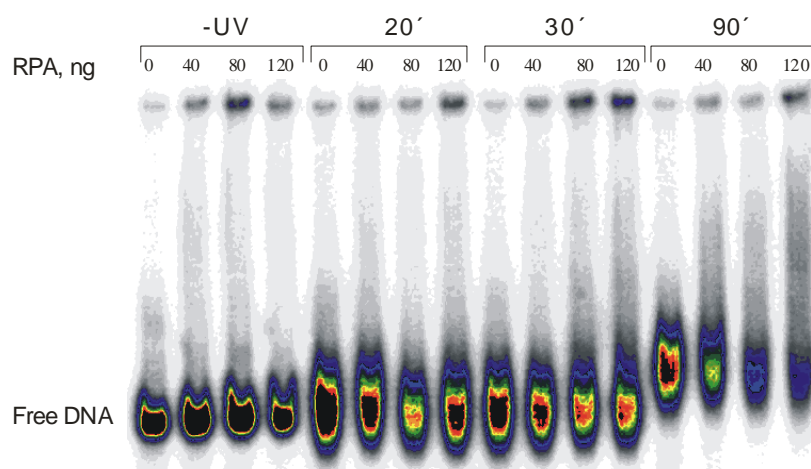


Figure 37. Interaction of RPA with intact and UV-light damaged DNA studied with EMSA. Human RPA was incubated with intact and UV-light damaged radioactively labeled 538 bp DNA without glutaraldehyde addition. The EMSA result does not show the presence of a distinct complex between RPA and DNA prior and after UV-exposure.

Only one band that corresponds to free DNA is clearly visible in Figure 37. We find only the same broadening of the bands and a lower mobility of the DNA molecules as a consequence of the UV-light irradiation as in experiments with UV-light damaged DNA without protein addition (Figure 29, A). The situation is different when after preincubation for 15 minutes glutaraldehyde (final concentration 0.1% w/v) was added and 10 minutes later the samples were loaded onto the gels. Figure 38 shows the binding of RPA to the 538 bp DNA being exposed to UV-light for different irradiation times. Clearly, RPA forms complexes with UV-damaged DNA under these conditions (see lanes 5, 8 and 11 in Figure 38). In the absence of glutaraldehyde no binding of RPA to undamaged DNA or to the UV-damaged DNA could be observed even for long irradiation times (see lanes 6, 9 and 12 in Figure 38). The addition of glutaraldehyde was necessary to stabilize the complexes during electrophoresis.

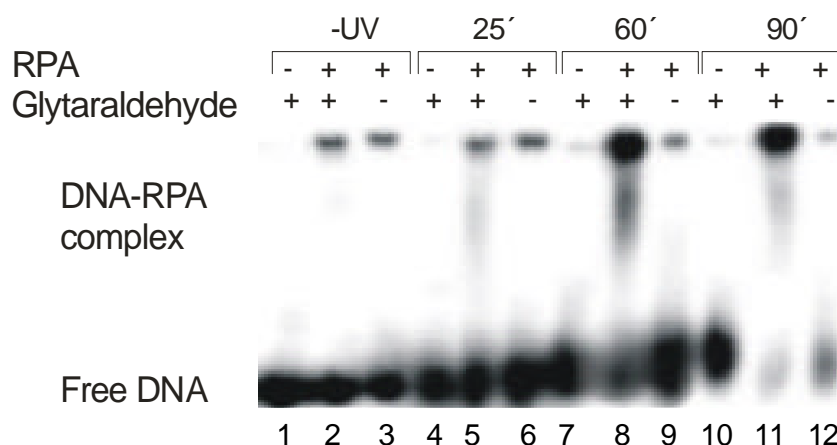


Figure 38. **Binding of hRPA to intact and UV-damaged 538 bp DNA.** RPA was incubated with intact DNA and the DNA (protein to DNA ratio) exposed to UV-light for different times with and without glutaraldehyde addition. Addition of glutaraldehyde leads to the formation of large complexes between RPA and DNA that stay in the loading pockets and are not able to move into the gel (Lysetska, 2002).

Neither the AFM measurements of the undamaged DNA molecules (Figure 34) nor the electrophoretic mobility experiments (Figure 37 and Figure 38) did show complex formation with RPA no matter whether or not glutaraldehyde was added.

4.4.4.2 *Human RPA interaction with UV-light damaged DNA studied with AFM*

For AFM measurements to study the interaction of RPA with UV-light damaged DNA we pre-incubated hRPA with DNA containing photoproducts (3.3, 4.3.1) at a concentration ratio of 1:1 and 1:3. According to our AFM results, the addition of hRPA to intact 538 bp DNA (2.3.2) leads to almost no change in the appearance of the DNA molecules in the AFM images (Figure 34, A). The situation is quite different, though, for UV-damaged DNA.

When hRPA was added to the damaged DNA, globular objects sitting on the rod shaped DNA strands were regularly observed in the AFM images (Figure 39, A-C). The globular objects were visible already at a concentration ratio of 1:1 (Figure 39, D) and appeared to be distributed over the whole length of the DNA, with a slight preference for the termini of the DNA.

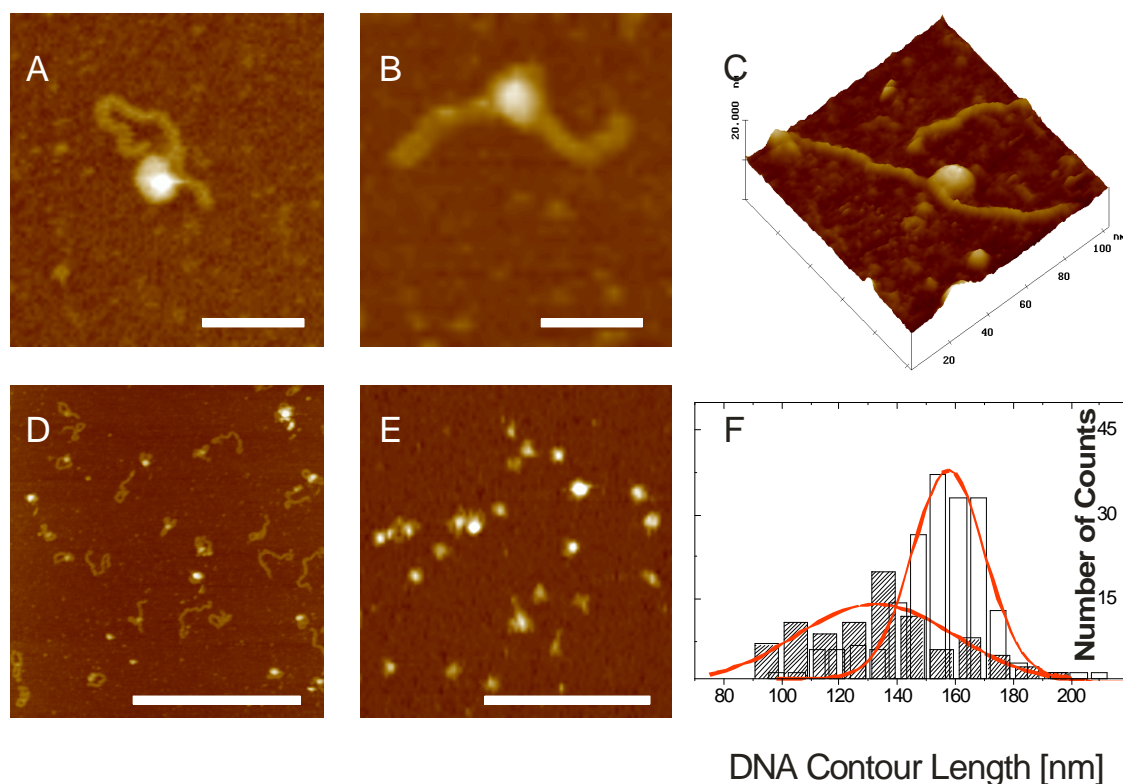


Figure 39. **Interaction of hRPA with DNA after UV treatment.** High resolution AFM shows that UV-damaged DNA shows a shortening of the DNA contour length (**A** and **B**) (2.5 mM NiCl_2 , 0.1% glutaraldehyde, in **A** and **B** scale bar 50 nm, z range 20 nm). The DNA makes a distinct turn around the protein molecule (**C**) (three-dimensional representation of UV-damaged DNA and RPA deposited on mica, 2.5 mM NiCl_2 , 0.1% glutaraldehyde, z range is 20 nm). UV-light damaged (30 min exposition) DNA was incubated with hRPA in the ratio 1:1 (**D**) (5 mM NiCl_2 , without glutaraldehyde, z range 20 nm) and 1:3 (**E**) (5 mM NiCl_2 , without glutaraldehyde, in **D** and **E** scale bar 400 nm, z range 20 nm). (**F**) Contour length distributions evaluated from the AFM images. Empty bars correspond to free DNA molecules exposed to UV light for 30 min and filled bars to the same DNA measured in DNA-RPA complexes. The red lines represent the Gaussian fit of the distribution (Lysetska, 2002).

The DNA molecules formed loop-like structures around globular objects in the majority of the cases. When hRPA was present in threefold excess over DNA, the number of irregular globular particles increased significantly (Figure 39, E) and the number of free DNA molecules reduced to 1:10. In this case, globular complexes are observed the shape of which render the determination of contour length and end to end distances difficult, if not impossible. The observation of globular complexes can be attributed to hRPA binding to UV-damaged sites.

To allow a more rigorous scanning of the complexes by AFM it proved useful to stabilize the complexes by glutaraldehyde. The presence of glutaraldehyde (at the concentrations used for ESMA) did not increase the amount of RPA binding to the undamaged DNA, but merely improved the high resolution imaging with AFM.

Comparison of the DNA contour length between free DNA and DNA in a complex with hRPA can provide information about the DNA part that actually contacts the protein. In Figure 39 D the contour length distributions of free DNA are plotted together with the apparent contour length of DNA in a complex with hRPA. A significant decrease in contour length was observed for complexes where both ends of the DNA probe could be identified in the AFM images (Figure 39, F). The contour length distributions and the mean values of the Gaussian fit depicted in Figure 39 D clearly shows that after complexation, the DNA contour length appeared to be 27.7 ± 7.6 nm shorter in comparison to DNA molecules damaged under identical conditions. The AFM images are in agreement with the notion of DNA wrapping around the protein (Figure 39, A-C). The surface plot of a high resolution AFM image of a DNA-protein complex indicates that the DNA molecules coil themselves around the protein (Figure 39, C).

We note that one (Figure 39, A-C) or more globular objects (Figure 41, A, C) were observed to bind to damaged DNA molecules. While high resolution AFM images show a certain sub-structure of the UV-damaged DNA-RPA complexes, quantitative results on the stoichiometry of the complex could not be achieved, as it is difficult to distinguish between hRPA subunits and separate protein molecules. Based on the measurements of the complexes' size, we do not exclude that complexes are composed of more than one hRPA molecules. It could be explained by hRPA cooperativity in the binding to DNA (Kim, 1994; Kim, 1995a). Most studies on the binding of hRPA to damaged DNA have shown the binding of a single RPA heterotrimer to a damaged site (Hey, 2001) and we therefore assume that these globular objects represent single hRPA molecules bound to a photodamaged region. Furthermore, the AFM experiments have been performed at a hRPA:DNA ratio of 1:1, with each DNA molecule carrying about 10 UV photoproducts. The formation of higher hRPA oligomers is unlikely under these conditions. In many of the complexes, loop-like structures are observed indicating that RPA contacts at least two regions of a damaged DNA molecule. DNA binding sites have been identified both on RPA70 and RPA32 (Iftode, 1999) and the loop-like structures may be due to DNA binding to both of these subunits via the damaged site and via the termini.

4.4.4.3 Model of hRPA binding to intact and UV-light damaged DNA

We were able to follow peculiarities of complex formation between undamaged and damaged DNA molecules and the human replication protein A both by electrophoretic and AFM measurements. In none of our AFM experiments we observed significant amounts of hRPA binding to the intact dsDNA chain. In the rare cases of complex formation, the binding typically occurred at the termini of the DNA molecule (Figure 34, B). This finding can be explained by the partial melting of the termini of the dsDNA producing ssDNA regions. hRPA recognizes ssDNA regions, i.e. binds specifically to

ssDNA. Even with an increase of the UV-light exposure, terminal binding to the DNA was found to be preferential. Our AFM investigations are in a good agreement with electron microscopy investigations, where cooperative binding of the RPA was found to be initiated by the termini of linear dsDNA fragments (Treuner, 1996).

As in the case of hRPA binding to DNA containing a single platinum or 6 nt bubble modification we do not find high affinity of hRPA to the damaged DNA. In these cases terminal binding of the hRPA was preferential and AFM images were similar as in the study of hRPA with intact DNA. Moreover, the binding of hRPA to cisplatin modified DNA was found to be weak and the protein molecules could be easily removed by the scanning movements of the tip. Such weak binding could be explained by participation of only a single or two ssDNA binding domains of the hRPA (1.3.2, Figure 5 A) in the complex formation with such small lesions like a single cisplatin modification or a 6 nt DNA bubble. In addition in these cases the DNA does not wrap around the hRPA protein.

Efficient complex formation between DNA and hRPA was possible only after UV exposure of the DNA, indicating that this process efficiently creates binding sites on the dsDNA. In the majority of cases UV-light damaged DNA formed complexes with hRPA appearing as spherical shapes in the AFM images. In cases where contour length measurements were yet possible after complex formation, we observe a contour length reduction of approximately 30 nm. From AFM measurements we find that a single hRPA molecule has a diameter, D_{RPA} , of ~6-7 nm while the diameter of a DNA chain, D_{DNA} , is about 2 nm. Therefore a 30 nm loss of DNA apparent contour length is in good agreement with the notion that the DNA molecules coil around the hRPA molecule (Figure 40), which would require $L_{coil} = \pi \cdot (D_{RPA} + D_{DNA}) \approx 27$ nm (when D_{RPA} 6.5 and D_{DNA} is 2 nm).

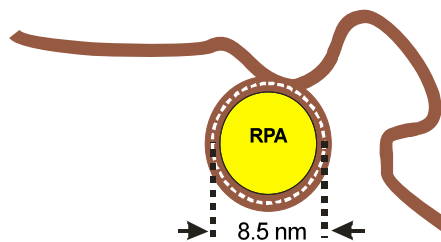


Figure 40. **Model of the hRPA binding to the UV-light damaged DNA.**

Reduction of the DNA contour length by about 30 nm as a consequence of the hRPA binding to the UV-light damaged DNA indicates that a protein-DNA contact spans ~90 bp, that is 3 times more than the detected mode for RPA binding to a 30 nt ssDNA

(Kim, 1992; Kim, 1994). However, such high difference in the number of DNA base pairs participating in the hRPA contact measured by AFM could be explained by the tip broadening effect when measuring length of DNA molecules.

Unfortunately, our AFM experiments do not provide information about the exact position of the hRPA on the chain, i.e. they can not discriminate to what – damaged or undamaged - ssDNA strand the hRPA molecules bind. Recent AFM analysis of the bacterial and eucariotic RNA polymerase also indicate wrapping of the DNA around protein (Rivetti, 2003)

Investigations of the binding of hRPA to UV-damaged DNA are rather difficult because DNA molecules carry multiple damage sites as a consequence of the UV damage. These sites induce DNA coiling around the protein, so DNA/hRPA complexes are looking like globular objects with undefined substructure in the majority of cases. This behaviour makes the evaluation of the stoichiometry of the complexes problematic.

Here we have shown how AFM imaging of hRPA-DNA complexes reveals structural features that cannot be seen with other techniques. Even though the resolution of the microscope does not allow a direct mapping of the trajectory of the DNA within the protein core, a detailed analysis of the DNA contour length suggests that the UV-light damaged DNA wraps around the hRPA in contrast to hRPA complexes with cisplatin and 6 nt bubble modified DNA.

4.4.5 Phase imaging of biomolecules in liquids

AFM records a topography signal, i.e. information about the heights of objects that are immobilized on a surface (3.4). We can distinguish between different types of molecules only by relying on their shape. For instance DNA has a longish structure while the proteins are globular. But when two types of the molecules have similar structure it is difficult to discriminate between them with AFM. If two or more components are under investigation and they have similar shape it becomes difficult to discriminate between them with AFM. Therefore it would be very useful if one could differentiate between different materials.

It has been shown in earlier studies that the phase signal in TappingMode™ atomic force microscopy can be used for a faster and less invasive imaging of biological samples in liquids (Argaman, 1997). The phase signal is known to be quite sensitive to attractive and repulsive forces acting on the tip (Knoll, 2003).

We note that for TappingMode™ phase imaging, it is important to determine the resonance frequency of the cantilever and the phase zero point with the tip located close to the surface.

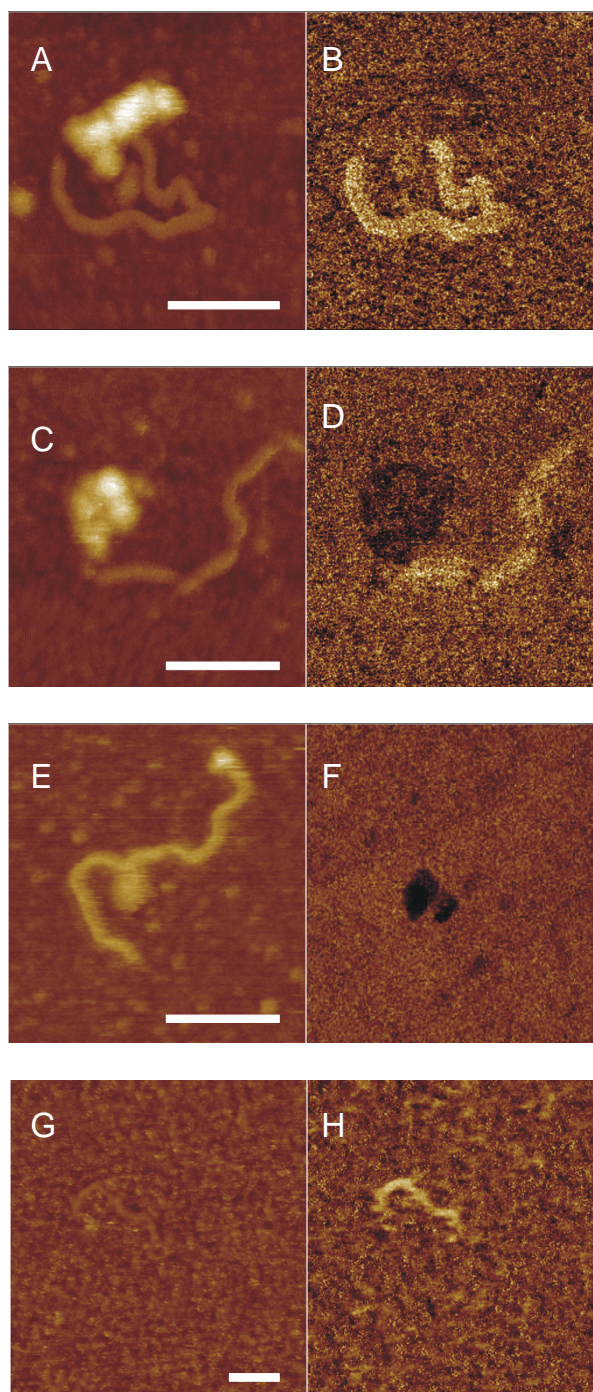


Figure 41. **AFM images of UV-damaged DNA and protein complexes immobilized on mica, scanning in buffer environment.** Human RPA molecules sitting on the split ends of the DNA molecule (**A**: height image, 2.5 mM NiCl₂, 0.1% glutaraldehyde, 15 nm z range; **B**: corresponding to **A** phase image, z range 60°). RPA molecules sitting near the end of the UV-light damaged DNA molecule (**C**) (height image, 2.5 mM NiCl₂, 0.1% glutaraldehyde, z range 15 nm; **D** - corresponding to **C** phase image, z range 60°). AFM image **E** shows two objects of increased height sitting on a single DNA molecule (z range 30 nm). Only one of them is seen in the phase image while the other is not (in **F** z range is 30°). The former most likely represents a protein. Moreover, the phase image indicates wrapping of the DNA around the RPA molecule. In the height image of the UV-damaged DNA with excess of XPA molecules (**G**) we do not see the DNA molecule, but the corresponding phase image clearly shows an elongated object of a higher phase contrast that corresponds to the DNA molecule (**H**) (z range is 30°). In all height images the scale bars correspond to 50 nm.

Therefore we first measured the tip resonance frequency by Fourier transforming the thermal noise spectrum of the tip approximately some 1 μm above the surface. Subsequently, the drive frequency was set to the resonance frequency and the phase zero was adjusted approximately 20 nm above the surface. We have recorded the phase signal along with the height image to differentiate between DNA and proteins. With the procedure outlined above, we observe a well-defined phase contrast between DNA and protein molecules. As an example, Figure 41 A-F shows different height and phase images of single DNA/RPA complexes. DNA exhibits a positive phase shift (i.e. it appears brighter in the phase image) and proteins show a negative phase shift (i.e. they appear darker in the phase image). Depending on the experimental parameters described in chapter 3.4.1, only DNA (Figure 41, B), only RPA (Figure 41, F), or both molecules are visible in the phase image (Figure 41, D). Figure 41 E and F show two objects of increased height along the DNA molecule. While the feature at the upper end of the molecule is not visible in the corresponding phase image (Figure 41, F) and possibly relates to a knot in the molecule, the feature in the center of the DNA most likely represents a protein. Moreover, the phase image indicates wrapping of the DNA around the RPA molecule. The information of the phase images was also helpful when we worked with excess of protein over DNAmolecules. Because of the excess of protein no elongated objects corresponding to DNA molecules are visible. Nevertheless, the corresponding phase image (Figure 41, H) shows the distinct presence of elongated objects of higher phase contrast, enabling the detection of DNA in between the protein matrix (Figure 41, G and H).

4.5 A SINGLE MOLECULE APPROACH TO THE STUDY OF DNA-BINDING PROPERTIES OF ORF80

In contrast to repair proteins (1.3), ORF80 (1.4) is a 9.5 kDa globular protein of undefined physiological role. It was purified and studied in details by Lipps *et al.* (Lipps, 2001). A footprint analysis revealed that ORF80 binds specifically to the dsDNA and recognizes the TTAA-N₇-TTAA motif. Additionally, according to fluorescence titration and gel-shift experiments (Figure 6), it forms large protein-DNA complexes of distinct stoichiometry: a single TTAA motif was found to bind six, while a full binding site (TTAA-N₇-TTAA) was found to bind twelve ORF80 molecules, respectively (Lipps, 2001).

The unique resolution of *in situ* AFM imaging promised to clarify this interesting binding behavior of ORF80 on DNA. Because of its small size ORF80 is rather problematic to visualize with AFM, but the predicted big complexes of up to twelve ORF80 molecules should be visible by AFM. To exclude a possible influence of the mica surface on the stoichiometry of the DNA-protein complexes we additionally studied the ORF80-DNA system in bulk solution using FCS (3.5).

In this chapter we report on our study of the ORF80-DNA binding properties using AFM and FCCS. The immobilization of the protein and the DNA-protein complexes for AFM investigations was accomplished as described earlier (4.1.1).

4.5.1 The binding of ORF80 to dsDNA studied with agarose gel electrophoresis

The binding of ORF80 to 538 bp DNA molecules (2.3.2) containing two full ORF80 binding sites (Figure 7) was studied by agarose gel electrophoresis (3.2.1). To visualize the localization of the DNA in the gel using ethidiumbromide staining (3.2.4), we had to use DNA concentrations higher than the 1-3 nM, which we used for the AFM investigations (4.5.2.2). The electrophoresis experiments served as a control to verify complex formation. ORF80 concentrations of 1 μ M and 0.2 μ M were mixed with DNA solutions at a constant DNA concentration of 6 nM. After incubation for 15 minutes, glutaraldehyde (final concentration 0.1% v/v) and Ni²⁺ ions (in a concentration of 5 mM) were added and 10 minutes later the samples were loaded onto the gels.

We did not observe any changes of the 538 bp DNA mobility upon addition of glutaraldehyde (Figure 42, lane 2) in comparison with pure 538 bp DNA (Figure 42, lane 1).

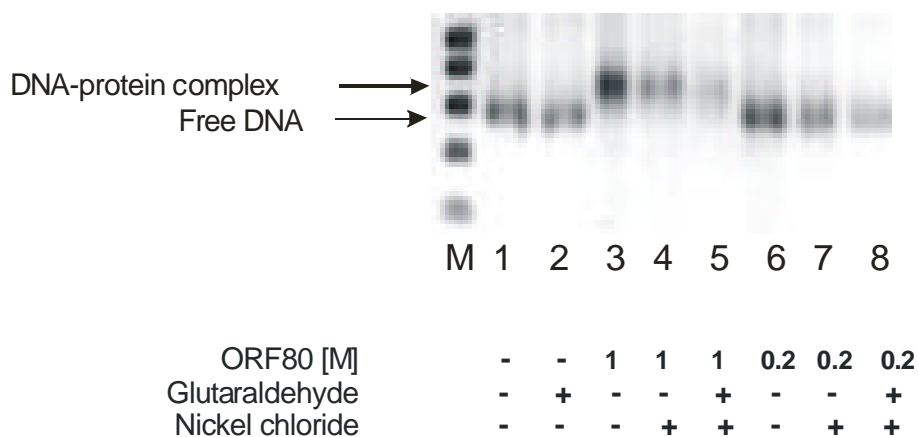


Figure 42. **Dependence of the electrophoretic mobility of the 538 bp DNA molecules in 1% agarose gel on Ni^{2+} , glutaraldehyde, and ORF80 addition respectively.** Addition of Ni^{2+} did not change the DNA mobility (lane 2) in comparison to the intact one (lane 1). However, the mobility of the 538 bp DNA fragment decreases with the addition of 1 μM ORF80 (lane 3). Both nickel chloride (lane 4) or glutaraldehyde (lane 5) addition did not interfere with DNA-ORF80 complex formation (see lane 3). When ORF80 was added to the DNA at lower concentration it was impossible to trace complex formation in the agarose gel no matter whether or not glutaraldehyde and nickel chloride was added (lanes 6-8).

However, the addition of a 160-fold excess of ORF80 to the DNA molecules leads to a small but distinct shift in the DNA mobility in the agarose gel (Figure 42, lanes 3-5) in comparison to the intact DNA (Figure 42, lanes 1 and 2). As we see from Figure 42, an addition of 1 μM of ORF80 to a 6 nM 538 bp DNA solution induces complex formation no matter whether or not nickel or glutaraldehyde addition (Figure 42, lanes 3-5). At lower ORF80 concentration (30 fold protein excess over DNA) we did not detect any shift of the DNA mobility due to complex formation (lanes 6-8 in Figure 42), i.e. the bands do not exhibit any shift relative to the reference band of free DNA (lane 1 in Figure 42).

It should be mentioned here that in the lanes where ORF80 was added at 160-fold excess over DNA we could see big DNA-protein agglomerates that did not even migrate into the gel but stayed in the loading gel pockets (data not shown).

4.5.2 Investigation of the ORF80 DNA binding properties with AFM

4.5.2.1 ORF80 studied with AFM

Since ORF80 carries a positive charge under the buffer conditions used, it could be immobilized on the negatively charged mica surface without counterion addition (4.1.4). Figure 43 A shows a typical AFM image of ORF80.

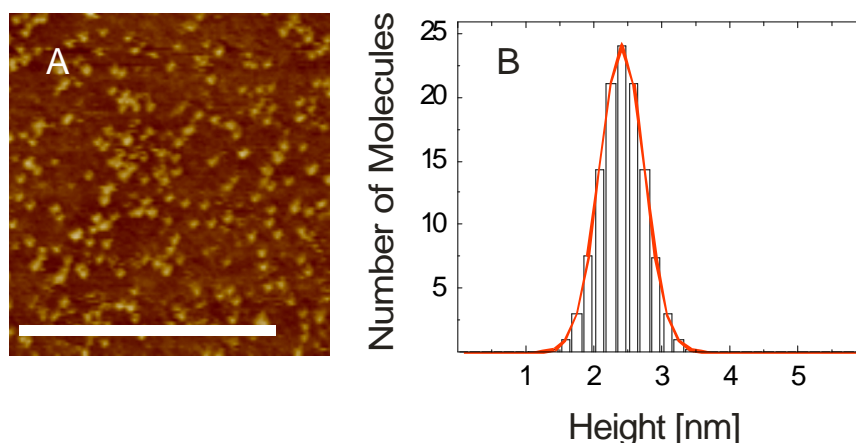


Figure 43. **Determination of the apparent heights of the ORF80 molecules from the AFM images.** (A) An AFM image of ORF80 on the mica surface (the scale bar corresponds to the 400 nm, the z data scale is 10 nm.); (B) Distribution of the height frequencies of the ORF80 molecules measured from AFM images. The solid line corresponds to Gaussian fit to the distribution.

5 μl of a 600 nM ORF80 solution was used for sample preparation. Under these conditions isolated ORF80 molecules adhere to the surface without Ni^{2+} addition, which can further be examined by AFM. From a set of images similar to the one shown in Figure 43 A, one can measure the dimensions of the adsorbed protein. We find a height of 2.4 ± 0.6 nm (Figure 43 B). ORF80 is a protein of molecular weight of 9.5 kDa. Assuming a globular shape and a density of about 1.2 g/cm^3 , one would expect a diameter of about 3 nm for a single ORF80 molecule. This value compares well with the height of 2.4 ± 0.6 nm determined from AFM images of ORF80 in the absence of DNA. To our knowledge ORF80 is the protein with smallest molecular weight that has been visualized with AFM.

4.5.2.2 AFM investigation of ORF80-DNA complexes

For all AFM investigations of the ORF80-DNA interaction we choose the same 538 bp DNA molecules as for the agarose gel electrophoresis (Figure 42), which contain two full binding sites for ORF80 (2.3.2, Figure 7). One binding site is located approximately in the middle of the DNA molecule, while the other is located slightly asymmetrically (at 49.1% and 37.1% of the DNA total contour length, respectively). The binding sites correspond to the pos.496 -510 and pos. 431-445 in the pRN1 plasmid sequence and are separated by 50 bp (see Figure 7). An AFM image of the DNA is presented in Figure 22, G.

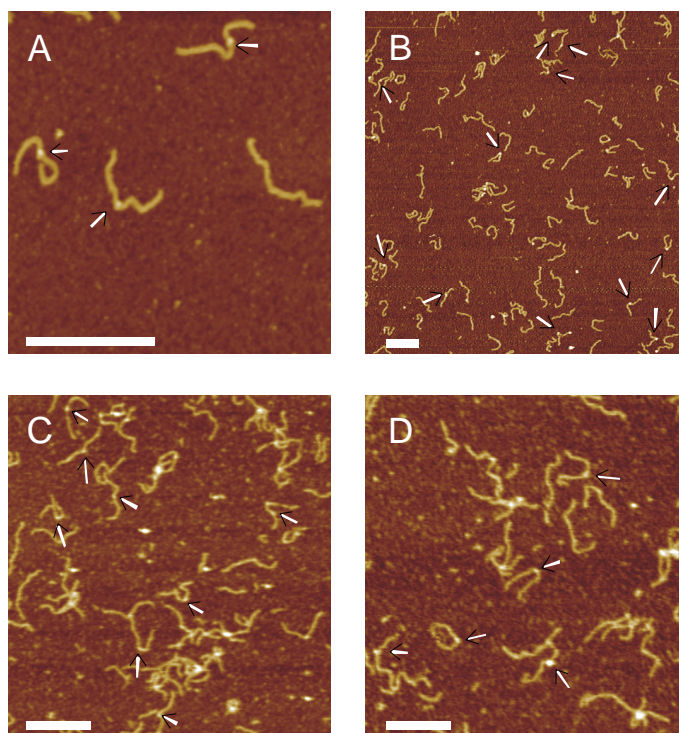


Figure 44. **Dependence of the ORF80 DNA-binding properties on the protein concentration.** (A) 100 nM ORF80 was incubated with 3 nM DNA. Single DNA molecules are visible that carry globular objects; (B) the same as in (A), but larger scan size. (C, D) the same as (B) but 300 nM ORF80 (arrows point to the ORF80-DNA complexes, bar is 200 nm, z range is 10 nm).

The average contour length of the DNA molecules measured from the AFM images is 177 ± 12 nm (Table 3). This value is in agreement with the expected length of ~ 182 nm for a 538 bp long DNA fragment (0.34 nm/bp, Figure 1). The average height of the DNA molecules as measured from the AFM images is 1.6 ± 0.3 nm (4.2.3.1, Figure 25 A).

DNA-protein complexes were obtained by pre-incubation of DNA and ORF80 in defined ratios for 10 minutes. Subsequently, the solution containing the complexes was deposited onto a freshly-cleaved mica surface.

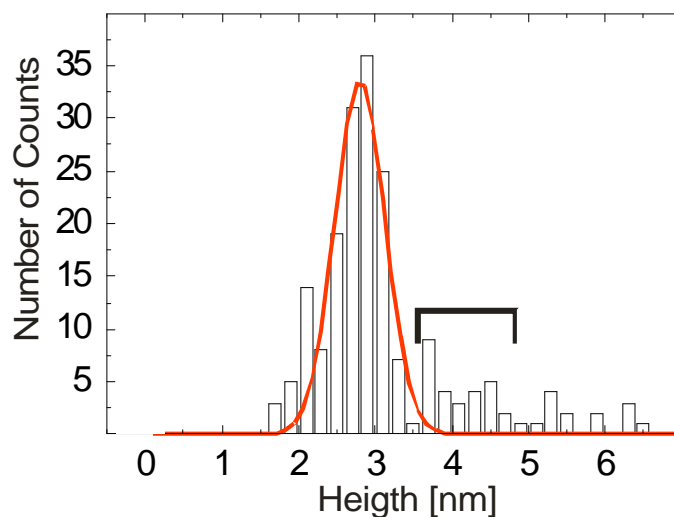


Figure 45. **Dimensions of the ORF80-DNA complexes measured with AFM.** Distribution of the frequencies of the DNA-protein complexes' heights measured from the AFM images. The solid line represents a Gaussian fit to the data.

Immobilization of the molecules in liquids for AFM investigation was performed as described in (4.1). As can be seen in Figure 44 we observe small globular objects bound to the DNA. No such objects were visible on DNA immobilized in the absence of ORF80 (4.2, Figure 22 G). Figure 44 demonstrates that despite of its small size, ORF80 molecules complexed to DNA can be well resolved in the AFM measurements in the liquid environment. To characterize the size of these complexes, we have determined a height histogram (Figure 45). The size of the objects is 2.8 ± 0.7 nm, which is slightly higher than the dimensions of the ORF80 molecules immobilized on mica (Figure 43). Because of the tip broadening effect the widths of the globular objects sitting on DNA can not be determined unambiguously.

ORF80 binds to DNA rather weakly with an apparent dissociation constant of 136 nM (Lipps, 2001). Therefore we assumed that a rather high concentration of ORF80 was required to obtain ORF80-DNA complexes to be observed in the AFM measurements. Indeed, at a protein concentration of 100 nM (approximately 30 fold excess over DNA concentration) only 15% of the DNA molecules are found to be complexed with the protein (Figure 44, A and B). In contrast, at a protein concentration of 300 nM (100 fold protein excess) nearly 80% of DNA molecules are bound to ORF80 (Figure 44, C and D). At this protein concentration we also observe larger aggregates of DNA molecules possibly bound together via ORF80 molecules (Figure 44, C and D).

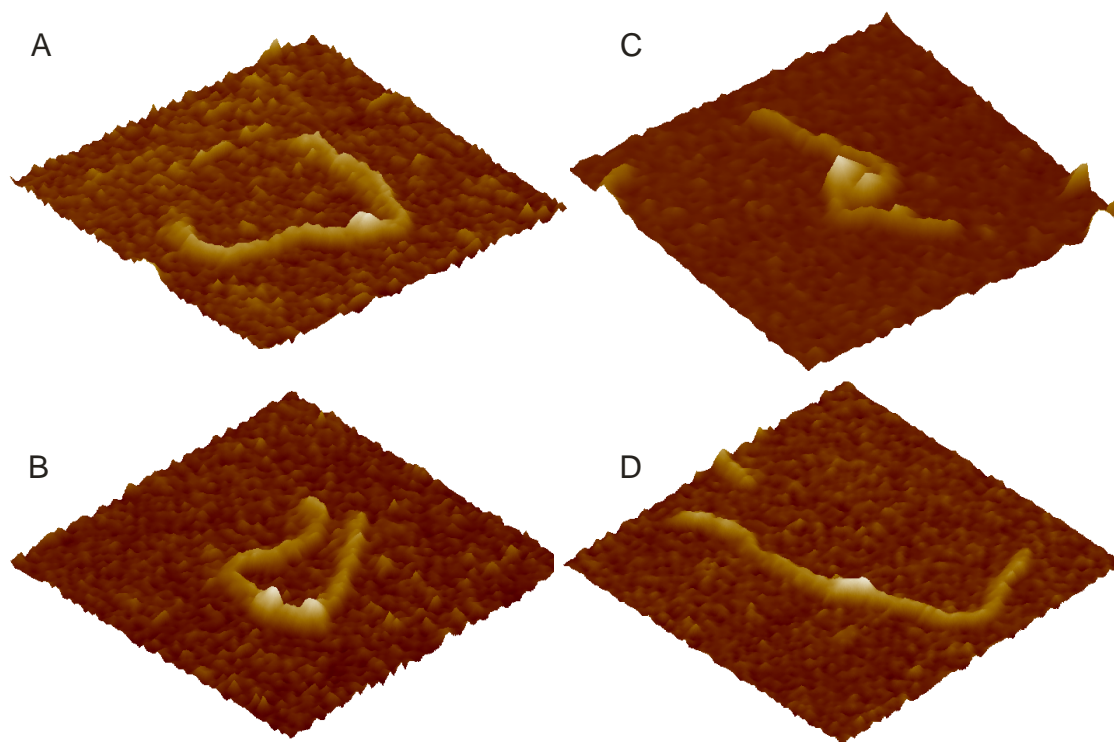


Figure 46. **3-D AFM images of DNA-ORF80 complexes.** The DNA molecules carry one (A) or two (B) globular objects. (C) Surface plot of the DNA that carries two globular objects of different heights. (D) shows a single elongated object sitting on the DNA molecule (lateral data scale is 170x170 nm, z data scale is 10 nm)

Definitely an increase of the ORF80 concentration appears to promote the nonspecific binding. Therefore proteins bound to the ends of the dsDNA are observed (Figure 47 A, B).

4.5.2.3 *Specificity of the ORF80 binding to dsDNA*

Examples of the high-resolution AFM images of ORF80/DNA complexes are shown in Figure 46. We find complexes with a single object (Figure 46, A and D) or with two globular objects along a DNA molecule (Figure 46, B and C). To investigate the specificity of the ORF80 DNA binding we measured the ORF80 positions along the DNA molecules on more than 200 protein-DNA complexes using the DnaCalc6 software (3.4.2). Quantitative analysis clearly shows that the distribution of the ORF80 along DNA molecule is not random (Figure 47, A and B). In Figure 47 A we plot the location of the ORF80 molecules along the DNA molecules for the case when only a single binding site is observed. Figure 47 B presents the data for DNA molecules carrying two globular objects. We find that in case of single ORF80 binding to the DNA (Figure 47, A), the ORF80 molecules are preferentially located near the middle of the DNA molecule, while the asymmetric site is only rarely populated.

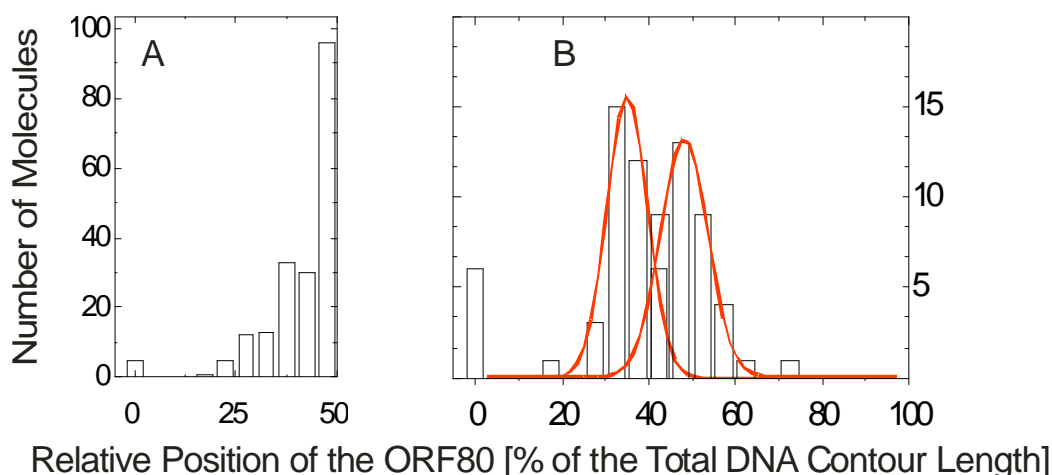


Figure 47. **Distribution of the frequencies of the positions of the ORF80 along DNA molecule.** Analysis of the DNA molecules with a single ORF 80 molecule (A) and with two (B) ORF80 molecules. When a single protein is bound (A) the maxima lies at $48\pm 8\%$ and $37\pm 7\%$ of DNA contour length. When two globular objects are sitting on the DNA (B) one finds protein located at around $35\pm 9\%$ and $48\pm 10\%$ of the DNA contour length. The solid lines correspond to Gaussian fits to the DNA contour frequencies distribution.

For DNA molecules carrying two distinct globular objects the analysis of the position of these objects corresponded to the location of the ORF80 binding sites (Figure 47, B). These experiments clearly show the site-specific binding of ORF80. The large width of the distribution shown in Figure 47 A and B reflects the finite lateral resolution of the technique, which is mainly due to the finite size of the tip.

4.5.2.4 *Stoichiometry of the ORF80-DNA complexes*

While the position of the protein on the DNA exhibits a clear preference to certain sites, it is hardly possible to define the exact number of proteins bound to each binding site (i.e. the stoichiometry of the complexes). Overall, the AFM images indicate a significant heterogeneity of the complexes (Figure 46, C). Cross-sectional analysis of the AFM images shows that the globular objects have an average height of 2.8 ± 0.7 nm (Figure 45) which is only slightly higher than the size of uncomplexed ORF80 (Figure 43) suggesting that these complexes containing one or two ORF80 molecules. Possibly, complexes of lower stoichiometry, in which the DNA is more easily accessible for ionic interactions with the surface coated with nickel ions, are deposited preferentially to the surface.

In particular, we observe complexes with two globular objects of different heights located on the DNA (Figure 46, C) probably corresponding to the binding of a larger number of proteins to a single binding site.

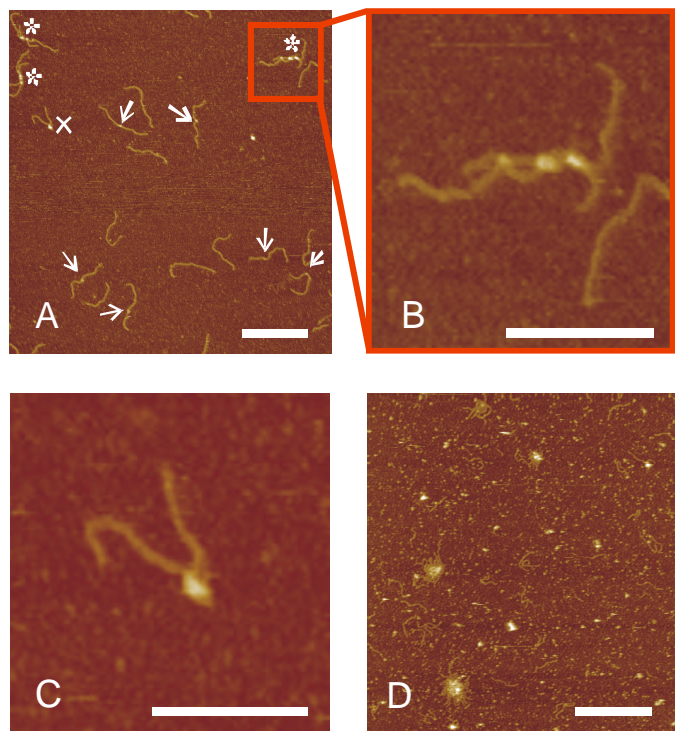


Figure 48. **Interaction of the DNA with ORF80.** At low ORF80 concentration only rare cases of DNA-protein complexes are visible (**A**) The arrows indicate DNA molecules complexed with only one protein molecule. (**B**) One of the complexes is marked in (**A**) with an asterisk. Two DNA molecules can be connected via protein molecules that are located on their specific binding sites. (**C**) Higher magnification of the complex marked in (**A**) with a cross binding sites are glued together, only free ends of length 82 nm and 61 nm are visible (in **A-C** scale bar corresponds to 100 nm). (**D**) Overview of the numerous DNA proteins agglomerates. Higher ORF80 concentrations lead to an increase of the size of the DNA - protein agglomerates. Objects containing different number of the DNA and protein molecules are seen in (**D**) (scale bar corresponds to 400 nm, z scale is 10 nm).

For example, a cross-section taken along the line connecting the centers of the globular objects sitting on the DNA presented in the Figure 46, C shows that the larger object is 4.2 nm high while the smaller object is 3.2 nm high. The height of the DNA molecules in these images amounts to 1.9 nm. Sometimes, rather long objects are observed up to 12 nm in length (Figure 46, D), indicating the formation of large complexes. It is possible that several ORF80 molecules are sitting close to each other on the protein binding sites. Since the expected distance between ORF80 binding sites on the DNA molecule is 22.28 nm (Figure 7), it sometimes appeared difficult to unambiguously distinguish between them with AFM.

In addition, we also observe complexes involving two different DNA strands (complexes marked with an asterisk in Figure 48, A and B). DNA molecules in these agglomerates appear to be connected via proteins bound to the different strands. Only about 1.5% of all DNA molecules are present in such complexes. At yet higher ORF80

concentration large agglomerates involving many DNA molecules are formed. (Figure 48, D).

These agglomerates are of varying shape and dimensions, but from the AFM images it is obvious that they are composed of numerous DNA and protein molecules. The formation of big agglomerates of different size and with a different number of DNA and protein molecules can be explained with both unspecific binding and high agglomeration tendency and increasing unspecific binding of ORF80 to the DNA molecules. At 1 μM protein addition to the DNA we trace the formation of big protein-DNA agglomerates with gel electrophoresis, too (chapter 4.5.1).

A quantitative analysis of the contour length of the DNA molecules (Figure 49) yields no difference between the DNA alone (Figure 23 B, Table 3) and DNA molecules bound to one (Figure 49, A) or two (Figure 49, B) ORF80 molecules. This finding indicates that the DNA molecules do not ‘wrap around’ the proteins.

Only in the rare cases where big globular objects are observed on the DNA (Figure 48, C) the apparent DNA contour length is shorter by approximately 20 nm (marked with arrows in Figure 49, A and B). This shortening may derive from looping out of the DNA between the proteins located on the two different ORF80 binding sites. The height of such objects is up to 4.5 nm (see bracket in Figure 45). Structures as depicted in Figure 48 C probably derive from gluing together the two ORF80 binding sites by protein-protein interactions, reducing the apparent contour length. One can often see a sharp bend in the DNA at the location, where a globular object is located. For example, only short ‘arms’, e.g. of 82 and 61 nm of the DNA molecule are visible in these cases (Figure 48 C).

Taking into account the low ORF80 binding affinity and a possible influence of the mica surface on the complex formation we have made a series of experiments in which preincubated DNA protein complexes were subsequently fixed with glutaraldehyde (final concentration 0.1% v/v). But we do not see any increase in complex formation in our AFM measurements (data not shown).

In summary, the AFM experiments show specific binding of ORF80 to a long DNA molecule exhibiting two ORF80 binding sites. Our AFM measurements allow a crude estimation of the maximal number of protein molecules present in the complexes. At the protein concentrations studied here, we found that one to two ORF80 molecules are bound to specific site.

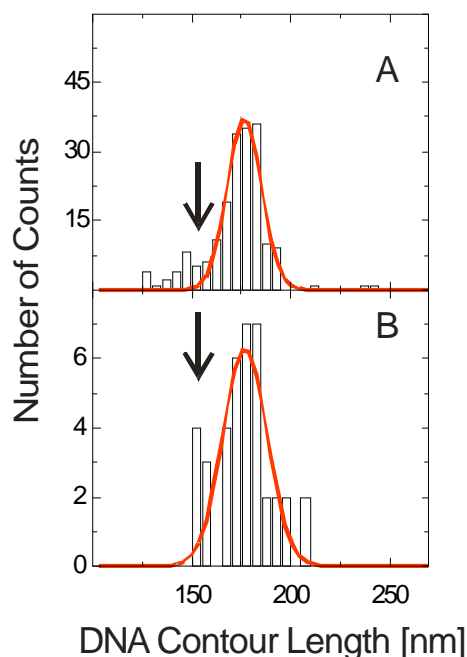


Figure 49. **Analysis of the apparent contour length of the DNA molecules as measured from the AFM images.** Frequency distribution of the apparent contour length of the 538 bp DNA with one globular object sitting on the DNA molecules (**A**). DNA that carries two distinct globular objects (**B**) Lines correspond to a Gaussian fit of the DNA contour frequencies distribution.

We were not able to identify complexes containing large numbers of protein bound to a single DNA molecule, as it was shown by Lipps *et al.* (Lipps, 2001). Having ORF80 in only 30 fold excess over DNA we already see complex formation in our AFM experiments.

Taking into account the low ORF80 binding affinity and a possible influence of the mica surface on the complex formation we have made a series of experiments in which preincubated DNA protein complexes were subsequently fixed with glutaraldehyde (final concentration 0.1% v/v). But we do not see any increase in complex formation in our AFM measurements (data not shown).

In summary, the AFM experiments show specific binding of ORF80 to a long DNA molecule exhibiting two ORF80 binding sites. Our AFM measurements allow a crude estimation of the maximal number of protein molecules present in the complexes. At the protein concentrations studied here, we found that one to two ORF80 molecules are bound to specific site. We were not able to identify complexes containing large numbers of protein bound to a single DNA molecule, as it was shown by Lipps *et al.* (Lipps, 2001). Having ORF80 in only 30 fold excess over DNA we already see complex formation in our AFM experiments. 15 % of the DNA molecules are already present in complexes with ORF80, which is not the case in the electrophoretic measurements

(Figure 42, lanes 6-8). Only at higher access of ORF80 to DNA we see a significant increase of the ORF80 binding to the DNA in both the AFM and the gel electrophoresis experiments. Taking into account our AFM investigations we consider that small shift in DNA electrophoretic mobility (Figure 42, lanes 3-5) corresponds to the binding of not more than two ORF80 proteins to single dsDNA.

4.5.3 FCS investigations of the ORF80 interactions with DNA

In order to critically test the results obtained by AFM imaging, we have performed complementary experiments using FCS (3.5.1). Like AFM, FCS is a single molecule technique that offers the possibility to determine the mobility of single, dye labeled molecules in solution (Schwille, 1997a). It is sensitive to complex formation whenever the latter is accompanied by a significant increase in hydrodynamic volume. Alternatively, the potential reaction partners can be labeled with two different fluorophores and complex formation can be observed by a “cross correlation” experiment fluorescence cross correlation spectroscopy (FCCS) (3.5.1). However, we were not able to obtain dye labeled protein that retained DNA-binding activity. In our experiments we traced the interaction of the ORF80 with DNA probes which were labeled at the 5′ ends with different fluorophores (see Table 1). Application of the FCCS technique helped us to discriminate between double stranded DNA, single stranded DNA, and free dye molecules. In our experiments the concentration of fluorophore-labeled DNA was kept constant at 5 nM. ORF80 was added to achieve the concentrations mentioned below. Measurements were carried out in FCS standard buffer (2.2). At each titration point FCS measurements were repeated at least three times over 300 s each.

4.5.3.1 *ORF80 binding to the 36 bp DNA containing a single TTAA-N₇-TTAA motif*

The diffusion time τ_{Diff} of the 36 bp DNA probe containing one full binding site (see fragment I in Table 1) is $\tau_{\text{Diff}} = 232.9 \pm 3.5 \mu\text{s}$ (Figure 50). Addition of ORF80 (up to a concentration of 60 nM) to the DNA (fragment I, Table 1) labeled with two fluorophores does not significantly influence the diffusion time of the DNA and fluctuations stay rather homogeneous (Figure 51 A, B).

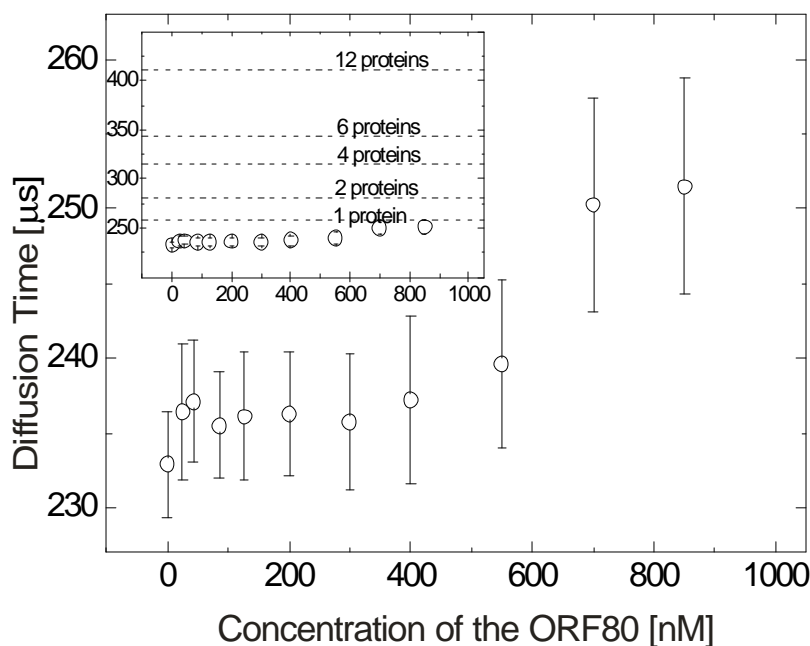


Figure 50. **Dependence of the diffusion time of 36 bp DNA with one full binding site on ORF80 concentration studied with FCCS.** Addition of ORF80 does not significantly influence the diffusion time of DNA, only a slight increase is visible. Addition of more than 850 nM ORF80 makes data processing not possible (see text). Inset shows the same data but on another data scale together with the theoretically calculated diffusion times for the same DNA fragment that would bind one, two, six and twelve ORF80 molecules.

At ORF80 concentrations higher than 60 nM the theoretical correlation function (3.5.2) could not be fitted to the experimental cross correlation function (Figure 51 D). A closer inspection of the raw fluorescence signal revealed large intensity fluctuations, which lasted considerably longer within the confocal volume (Figure 51 C). This observation clearly indicates the presence of large objects which contain many fluorophores (i.e. large fluorescence intensity). Under these conditions a standard analysis of the FCCS signal is not possible. One way around this problem is to perform a large number of FCCS experiments collecting data for relatively short measurement times (typically 10 sec). Spectra containing large fluorescence fluctuations are then excluded from further processing. The remaining correlation functions can subsequently be added (Figure 51 E) and can be fitted (Figure 51, F) by the standard correlation function. When we process the FCCS spectra as described above we see that addition of ORF80 leads to a slight increase of the diffusion time (Figure 50). However, the mass difference between the free dsDNA and potential complexes is not large enough to allow unambiguous discrimination of two separate particle fractions in the FCCS signal. Therefore, the FCCS data were fitted assuming a single fraction of particles of well-defined size.

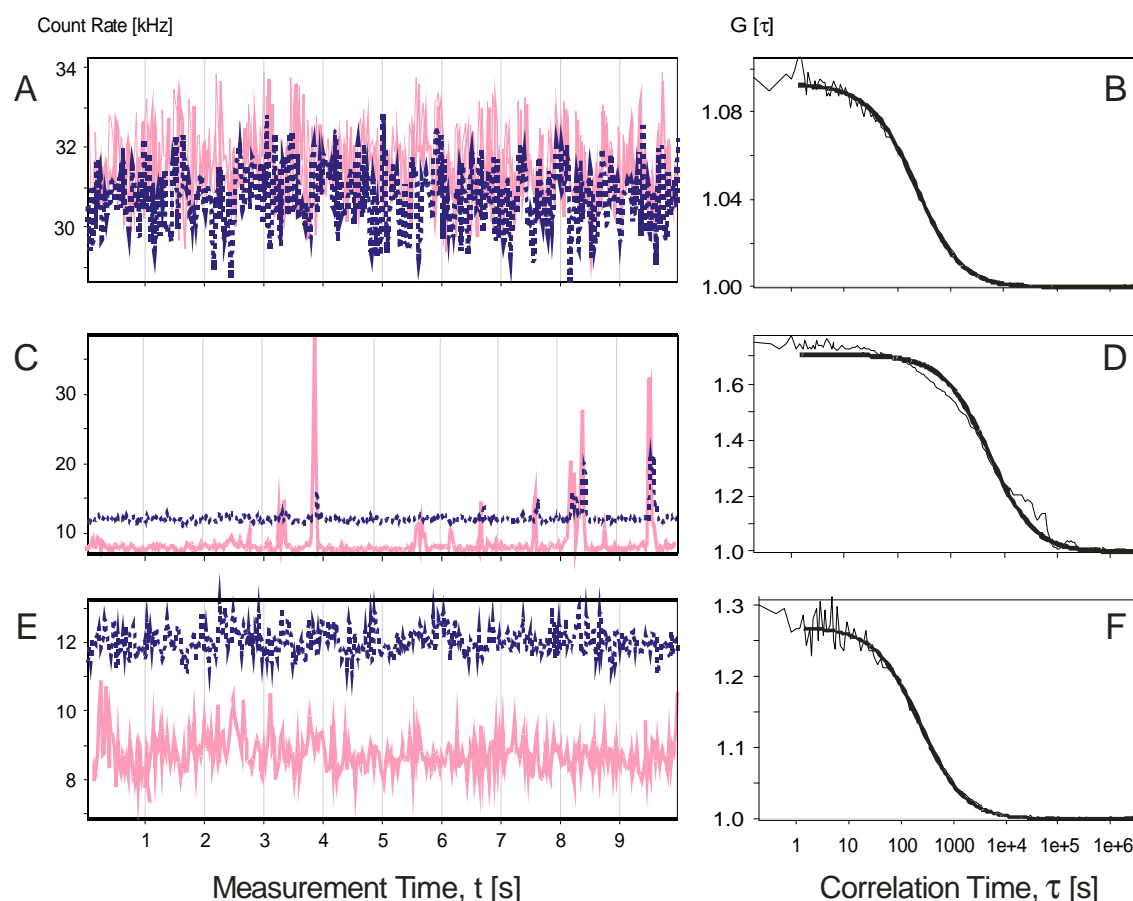


Figure 51. **Investigation of the ORF80 DNA binding properties studied with FCCS.** Fluorescence fluctuations of the 36 bp DNA after addition of the 25 nM ORF80 (A) are rather homogeneous and can be fitted accurately (B). Fluorescence fluctuation after addition of the 850 nM ORF80 (C) could not be fitted (D) with the standard software. (E) The same fluorescence fluctuations as in C but after removal of the large peaks. These data can be fitted (F) by the standard fitting program.

The double stranded 36 bp DNA probe containing two fluorophores (fragment I in Table 1) has a molecular weight of approximately 25 kDa. Binding of an ORF80 dimer of 19 kDa to the DNA probe would increase the mass by a factor of 1.76. This increase in mass is at the limit of FCCS resolution (2001; Meseth, 1999). In our FCCS experiments we observed a slight but reproducible increase in the diffusion time and this increase is clearly protein-dependent. Given the molecular weights of DNA and ORF80, the inset of Figure 50 indicates the expected diffusion times for 100 % DNA molecules bound to one, two, four, six and twelve ORF80 molecules, respectively. Significantly higher stoichiometries would lead to a larger increase in diffusion time (see inset to the Figure 50) which would have been easily detectable. Our FCCS experiments are therefore not compatible with the formation of large protein-DNA complexes as suggested by fluorescence anisotropy measurements (Lipps, 2001). At

higher ORF80 concentrations the formation of larger aggregates with long diffusion times is observed by FCCS too, and these complexes contain multiple DNA molecules.

Comparison of the theoretical data with the experimentally observed increase of the DNA diffusion time leads us to exclude the presence of a significant amount of DNA molecules bound with more than two ORF80 molecules. This finding is in agreement with the AFM observations discussed above (4.5.2.4). So far the results of the FCCS experiments corroborate the AFM results discussed above. At higher ORF80 concentrations, both techniques give evidence for the formation of large agglomerates involving many DNA and ORF80 molecules. In the FCCS experiments, these agglomerates appear as bursts in the fluorescence intensity, resulting from a large number of dye molecules simultaneously passing the excitation volume. The duration of these bursts indicates that agglomerates of large size are formed.

We note that at 100 times lower DNA concentrations (0.05 nM) undisturbed fluctuations were observed on addition of up to 3 nM of ORF80. However, addition of 10 nM ORF80 already led to the appearance of numerous peaks in the fluorescence intensity (like in Figure 51, C) indicative of the formation of large aggregates.

In order to show that different dsDNA (rather than ssDNA) molecules participate in the formation of large aggregates, a mixture of differently labeled 36bp dsDNA (concentration of 0.05 nM) with a single ORF80 binding site each was prepared (1:1 mixture of fragments II and III, Table 1). While no cross correlation was observed for the pure DNA mixture (black line in Figure 52, B), the addition of ORF80 at concentrations above 10 nM again led to the formation of big, polydisperse agglomerates carrying both fluorophores (like in Figure 51 C).

4.5.3.2 Unspecific binding of ORF80 to the ss- and dsDNA

Test experiments using a 36 bp DNA fragment that carries both fluorophores *without* an ORF80 binding site (fragment IV in Table 1) under the same conditions shows no increase of the diffusion time due to the protein addition in comparison to the pure DNA (Figure 52, A). Fluorescent fluctuations stay rather homogeneous up to 60 nM of the protein and can be fitted by the standard correlation function (like in Figure 51, B). Nevertheless, agglomerates appear starting from 60 nM of the protein, too (like in Figure 51, C and D).

A similar experiment was performed using two differently labeled dsDNAs *without* any ORF80 binding site at a concentration of 0.05 nM (1:1 mixture of fragments V and VI in Table 1). Again, below 10 nM ORF80 no cross correlation signal was observed (like in Figure 52, B), while at higher ORF80 concentrations the formation of large agglomerates was found.

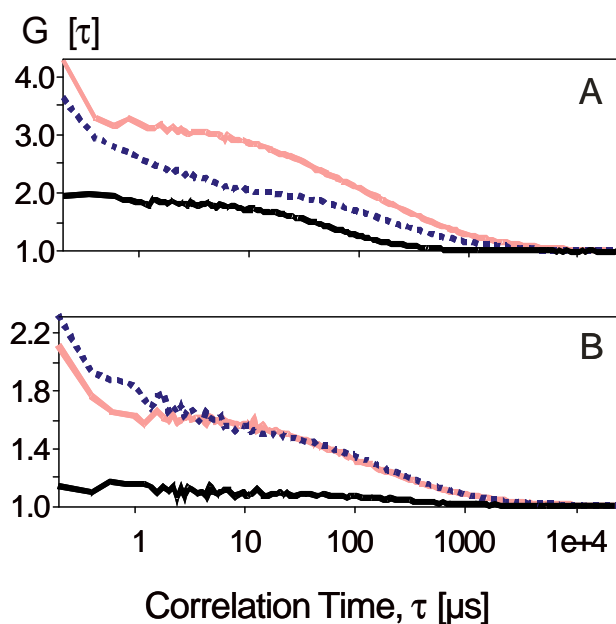


Figure 52. **Investigation of the DNA hydrodynamic properties with FCCS.** (A) 36 bp DNA fragments that carry two fluorophores on each dsDNA (fragment I in Table 1). (B) mixture of DNA molecules where each DNA molecule carries one label (fragments II and III in Table 1).

In order to study unspecific binding of ORF80 to ssDNA we performed a series of experiments using ORF80 and a mixture of the uncomplimentary ssDNA substrates in a concentration of 0.05 nM labeled with different fluorophores (2.3.1). Without protein addition no cross correlation signal was noticed (like in Figure 52, B). The addition of ORF80 induced the appearance of a cross correlation signal indicating that different ssDNA molecules (carrying different fluorophores) are “glued together” by ORF80. At ORF80 concentrations below 30 nM diffusion times of 400-700 μs were obtained. With progress in the measurement the diffusion times of the protein-DNA complexes increased. At higher ORF80 concentrations we only observed single events of very high signal intensity. That result corroborates the data of Lipps *et al.* (Lipps, 2001) where ORF80 was found to bind unspecifically to ssDNA.

In conclusion we note that a comparative study of the ORF80 interaction with dsDNA by FCCS and AFM shows distinct peculiarities of the protein binding to the DNA. The most significant result of our AFM experiments is the direct observation of the specific binding of the ORF80 molecules to the two binding sites on the dsDNA. To our knowledge, protein-DNA complexes with such a small protein have not been studied with AFM before. Under low protein concentration specific binding of the ORF80 dominates. Under these conditions the protein recognizes a specific sequence on the DNA. It forms complexes with DNA that contain about two ORF80 molecules per single TTAA-N₇-TTAA motif. Higher ORF80 concentrations lead to the formation of big protein-DNA agglomerates that contain numerous DNA and protein molecules. The

4.5 A comparative study of the ORF80 DNA-binding properties using AFM and FCS

formation of these agglomerates can be explained both by the unspecific ORF80 binding and its high aggregation properties. Our experiments showed that application of the single molecules techniques are especially important when proteins with high aggregation tendency are under investigation.

5 SUMMARY

The progress in the development of single-molecule techniques enabled the observation of biochemical processes under almost physiological conditions. In the present work we study the architecture of intact and damaged DNA and their interaction with DNA-binding proteins using a combination of atomic force microscopy (AFM) and fluorescence correlation spectroscopy (FCS). AFM in liquids provides topographical real space information about biomolecular structures that are adsorbed at a solid-liquid interface. Thus, the immobilization of the molecules on the solid support is mandatory and represents the most crucial challenge.

In the beginning of this scientific work we therefore focus our efforts on the development of a reproducible protocol for the surface-deposition of different biomolecules, such as linear and circular DNA, different types of proteins and DNA-protein complexes. A major interest was dedicated to the immobilization of DNA molecules onto a mica surface. It was shown that the addition of nickel ions to the AFM deposition buffer at a final concentration of 2.5 mM leads to an efficient immobilization of DNA molecules on a mica surface. An equilibration time of one minute before the application of the nickel ions leads to the highest value of the measured DNA persistence length. It is demonstrated that this deposition protocol also enables the visualization of DNA molecules in motion. The role of Ni^{2+} and Mg^{2+} in the mechanism of DNA immobilization on a mica surface is discussed. Additionally, the influence of Ni^{2+} , Na^+ as well as H^+ on the hydrodynamic properties of DNA molecules in bulk solution is studied using FCS. The developed protocol for the immobilization of DNA and protein molecules is used throughout this work.

The analysis of the apparent contour length of intact DNA molecules of different lengths and under different preparation routines is found to be consistent with its B-DNA conformation. The mean persistence length of the DNA molecules is determined to 38 ± 7 nm. Our AFM measurements demonstrate that the purity of the DNA samples is critically dependent on their preparation. The purification of DNA samples by agarose gel separation leads to a wide distribution of the DNA lengths and to the presence of globular objects of non-DNA origin. DNA fragments prepared by polymerase chain reaction reveal the highest purity and show the highest homogeneity in apparent length. A comparison of the AFM results with gel-electrophoretical results shows that gel electrophoresis is less sensitive to the presence of impurities of DNA origin. An adsorption of DNA on silica-gel particles yields the highest level of purity. The DNA samples are free from contaminations of non DNA origin

As a next step we analyze the architecture of DNA molecules that carry different DNA lesions. In this thesis we report about the first structural study of long DNA molecules that carry UV-light photolesions at random sites. An exposure of DNA to UV light introduces different modifications to the DNA structure: regions of unpaired DNA of different lengths, sharp kinks, the presence of knot like structures and single-strand breaks. In addition, the dynamics of damage accumulation can be traced with AFM. UV-exposure influences both the apparent contour length and the persistence length of the molecules. The structure of UV light damaged DNA strongly depends on the exposure time. Longer UV-light exposure time introduces increasing DNA damage. An FCS study on DNA exposed to UV-light shows that the presence of photoadducts influences the hydrodynamic properties of DNA molecules. The results obtained using both AFM and FCS are compared with gel-electrophoretical experiments.

Additionally, our AFM investigations reveal peculiarities in the conformation of DNA molecules that carry a defined 6 nt bubble and a terminal ssDNA tail modification. However, the presence of a defined cisplatin intrastrand adduct within a long DNA molecule does not show any structural changes in comparison to intact DNA of the same length.

The knowledge of the conformation of intact and damaged DNA molecules in AFM images was further used as a reference for the analysis of their complexes with the proteins involved in the initial DNA damage recognition in nucleotide excision repair. Preliminary experiments on the interaction of XPC-hHR23B with DNA molecules that carry a defined 6 nt modification reveal a higher affinity than human replication protein A (hRPA) to the same substrate. However, the extremely high agglomeration property of this protein prohibited the performance of a statistical analysis of those DNA-protein complexes.

Further, we report about a first AFM study of the hRPA binding properties to intact and damaged DNA. The damage types under investigation were a 6 nt bubble modification, a cisplatin modification as well as lesions induced by UV-light. In our AFM experiment we never find RPA to be bound to the intact dsDNA chain. In complexes with intact DNA human RPA is only found to be bound to the termini of the linear DNA molecules. Human RPA binds with a very low affinity to both DNA containing a 6 nt bubble modification and a single cisplatin modification. Moreover, hRPA showed in this case still a preferential binding to the ends of the linear DNA molecules as seen in the complexes with intact DNA. Because of the low binding strength of hRPA to the cisplatin intrastrand adduct it is easily possible to remove the protein from its DNA complexes by scanning movements of the AFM tip. The images of the DNA molecules after removal of the hRPA proteins show significant distortions of the DNA chain,

namely: the separation of the double strand into single-strands resulting in a large region of unpaired bases. Such structures are never observed in images of DNA carrying a cisplatin lesion before the addition of hRPA. This fact may explain a possible role of hRPA in damage excision.

Our experiments show a rather high affinity of hRPA to UV-light damaged DNA that increases with UV-light exposition time. The formation of complexes of hRPA and UV-light damaged DNA molecules was studied by both EMSA and AFM. When hRPA was added to the damaged DNA, globular objects sitting on the rod shaped DNA strands were regularly observed in the AFM images. A systematic analysis of the apparent contour length of DNA molecules in protein-DNA complexes reveals a reduction of the contour length in comparison to the one of uncomplexed DNA molecules damaged for the same time. Such reduction of 27.7 ± 7.6 nm suggests a wrapping of the DNA molecule around the hRPA protein. Additionally, using the hRPA-DNA system, we show that the application of the phase signal allows to differentiate between components of similar architecture, but different origin within one AFM image.

The last chapter of the thesis is dedicated to the analysis of the DNA-binding properties of ORF80, a novel leuzine protein of unknown physiological role. Our AFM measurements demonstrate that under low protein concentration a specific binding of ORF80 dominates. To the best of our knowledge ORF80 is the smallest protein that was resolved in complexes with DNA by AFM. The single molecule approach in the study of the ORF80 binding properties to DNA with AFM shows that one, at most two ORF80 monomers recognize a specific sequence on the dsDNA. This result is to be seen in contrast to the results obtained earlier using gel electrophoresis and fluorescence titration experiments, which showed stoichiometries of more than twenty ORF80 monomers per single specific binding site. Both AFM and FCS clearly show that higher ORF80 concentrations lead to the formation of big protein-DNA agglomerates that contain numerous DNA and protein molecules. The formation of these agglomerates can be explained both by the unspecific ORF80 binding and its high aggregation properties. Our experiments show that the use of single molecules techniques is especially important when proteins with high aggregation tendency are under investigation. Moreover, the resolution of AFM allows tracing of conformational changes and structural peculiarities of long DNA molecules and their complexes with proteins of different sizes, which is not possible with other techniques.

6 ZUSAMMENFASSUNG

Der Fortschritt in der Entwicklung von Einzelmolekülmethoden machte die Beobachtung biochemischer Prozesse unter quasi-physiologischen Bedingungen möglich. In der vorliegenden Arbeit untersuchen wir intakte und geschädigte Desoxyribonukleinsäure (DNA) und ihre Wechselwirkung mit DNA-bindenden Proteinen mittels einer Kombination von Raster-Kraft-Mikroskopie (AFM) und Fluoreszenz-Korrelations-Spektroskopie (FCS). AFM in Flüssigkeiten liefert eine räumliche, topografische Information über biomolekulare Strukturen, die an einer Fest-Flüssig-Grenzfläche adsorbiert sind. Daher ist für die Abbildung mit AFM die Immobilisierung der Moleküle auf der festen Oberfläche notwendig und beinhaltet eine entscheidende Herausforderung.

Am Anfang dieser Forschungsarbeit haben wir uns daher mit dem Entwicklung eines reproduzierbaren Protokolls zur Immobilisierung verschiedener Molekültypen auseinandergesetzt, wie z.B. linearer and zirkularer DNA, unterschiedlicher Proteine sowie DNA-Protein Komplexen. Das meiste Interesse galt der Immobilisierung von DNA auf einer Klimmeroberfläche. Es wurde gezeigt, dass die Zugabe von Nickel Ionen in einer Endkonzentration von 2.5 mM eine effiziente Immobilisierung der DNA Moleküle auf der Klimmeroberfläche bewirkt. Eine Wartezeit zur Einstellung eines Konformationsgleichgewichts von einer Minute vor der Zugabe von Nickelionen führte zu den größten Werten der gemessenen DNA Persistenzlänge. Es wird gezeigt, dass das entwickelte Protokoll zur Immobilisierung der DNA noch immer die Beobachtung von Bewegungen der DNA Molekülen zulässt. Die Rolle der Ni^{2+} und Mg^{2+} Ionen im Immobilisierungsmechanismus von DNA auf Klimmeroberfläche wird diskutiert. Zusätzlich wurde mittels FCS der Einfluss von Ni^{2+} , Na^+ sowie H^+ auf die hydrodynamischen Eigenschaften von DNA in Lösung untersucht. Das entwickelte Protokoll zur Immobilisierung von DNA und Protein Molekülen wurde für alle weiteren AFM Untersuchungen in dieser Arbeit benutzt.

Die Analyse der Konturlänge intakter DNA Moleküle mit unterschiedlichen Längen und mit unterschiedlichen Methoden präpariert zeigt, dass sich die DNA auf der Oberfläche in der B-DNA Konformation befindet. Eine mittlere Persistenzlänge von 38 ± 7 nm wurde ermittelt. Die AFM Untersuchungen zeigen auch, dass die Sauberkeit der DNA Proben stark von der Methode der Probenpräparation abhängig ist. Die Reinigung der DNA-Proben mittels Agarosegel führt zu einer breiten Verteilung von DNA Längen und der Anwesenheit von globularen Teilchen, die nicht von der DNA stammen. Die DNA Moleküle, die mittels, Polymerase-Kettenreaktion hergestellt

wurden, zeigen die größte Reinheit und die höchste Homogenität in der DNA Konturlänge. Ein Vergleich der AFM Ergebnisse mit Ergebnissen aus Gelelektrophoretischen Messungen zeigt, dass letztere weniger sensitiv auf von DNA abstammenden Unreinheiten ist. Die Reinigung der DNA durch Adsorption an Silicagel-Partikeln liefert die beste Reinheit. Diese DNA Proben sind frei von Unreinheiten, die nicht von DNA stammen.

Zunächst analysieren wir die Architektur von DNA Molekülen, die unterschiedliche DNA Schadenstypen tragen. In dieser Arbeit berichten wir über die erste strukturelle Untersuchung von DNA Molekülen mit unspezifischen UV-Schäden. Die Bestrahlung der DNA mit UV-Licht erzeugt unterschiedliche Modifikationen in der Struktur der DNA: Regionen ungepaarter DNA von unterschiedlicher Länge, scharfe Knicke, die Anwesenheit von Knotenstrukturen und Brüche von Einzelsträngen. Zusätzlich kann die Dynamik der Schadensakkumulation in der DNA mittels AFM nachgewiesen werden. Die Bestrahlung mit UV-Licht beeinflusst sowohl die Konturlänge als auch die Persistenzlänge der Moleküle. Die strukturellen Veränderungen UV-bestrahlter DNA sind von der Belichtungszeit abhängig. Längere Belichtungszeiten führen zu einer Zunahme der DNA Schäden. FCS Experimente an UV-bestrahlter DNA zeigen den Einfluss der Schädigungen auf die hydrodynamischen Eigenschaften der DNA Moleküle. Die Ergebnisse der AFM und FCS Messungen werden mit Gelelektrophoresedaten verglichen.

Zusätzlich zeigen die AFM Messungen Besonderheiten in der Konformation von DNA Molekülen, die eine definierte 6 nt Mismatch-Region oder eine ssDNA Modifikation an einem Molekülende tragen. Jedoch führt die Anwesenheit eines definierten Cisplatin-Addukts in längeren DNA Molekülen zu keinem sichtbaren Einfluss auf die Struktur im Vergleich zur ungeschädigten DNA der gleichen Länge.

Die Kenntnis der Konformation von intakter und geschädigter DNA wurde weiter benutzt als Referenz für die architektonische Analyse von DNA-Komplexen mit Proteinen, die für die anfängliche Schadenserkennung in der Nukleotid-Exzisions-Reparatur (NER) zuständig sind. Einführende AFM Experimente über die Wechselwirkung von XPC-hHR23B mit DNA Molekülen, die eine definierte 6 nt Modifizierung tragen, zeigen eine erhöhte Affinität von XPC in Vergleich zu hRPA zum gleichen Substrat. Jedoch lässt diese hohe Aggregationsneigung des Proteins eine statistische Analyse der Struktur seiner Komplexe mit DNA nicht zu.

Weiter berichten wir über die erste AFM Untersuchung der Bindungseigenschaften des Proteins hRPA zu intakter und geschädigter DNA. Die untersuchten Schädigungen der DNA sind im Detail eine definierte 6 nt Mismatch Modifikation, eine Cisplatin-Modifikation, sowie von UV-Licht verursachter Schaden. In unseren AFM

Experimenten haben wir niemals die Bindung von hRPA zu der intakten DNA-Kette festgestellt. Das humane RPA Protein wurde nur als Komplex an den Molekülen der intakten, linearen DNA Moleküle gefunden. Dieses hRPA bindet mit einer sehr niedrigen Affinität sowohl zu einer 6nt Mismatch Modifikation als auch zu einer definierten Cisplatin-Modifikation. Zusätzlich zeigt RPA in diesem Fall eine präferenzielle Bindung zu den Enden der linearen DNA Moleküle, wie in den Experimenten mit ungeschädigter DNA. Auf Grund der niedrigen Bindungsstärke von hRPA zum Cisplatin-Intrastrang-Addukt war es sehr einfach möglich das Protein von seinem Komplex mit der DNA mittels der Rasterbewegungen der AFM-Spitze zu trennen. Die Abbildungen der DNA Moleküle nach der Entfernung der Protein Moleküle zeigen eine bedeutende Veränderung in der DNA-Kette. Der Doppelstrang wird in Einzelstränge getrennt, und lange Regionen von ungepaarten Basen entstehen. Solche strukturellen Änderungen treten niemals bei DNA Molekülen mit Cisplatin-Schaden vor der hRPA Zugabe auf. Diesen Fakt kann man womöglich mit der Rolle von hRPA in der Schadenexzision erklären.

Unsere Experimente zeigen eine erhöhte Affinität von hRPA zu UV-Licht geschädigter DNA, die mit der UV-Dosis zunimmt. Die Bildung von Komplexen von hRPA und UV-licht geschädigter DNA wurde mittels Bandenretardationsexperimenten und AFM untersucht. Sobald hRPA zu der DNA zugegeben wird, wurden regelmäßig in den AFM Abbildungen globulare Objekte auf den stäbchenförmig erscheinenden DNA Molekülen gefunden. Eine systematische Analyse der Konturlänge der DNA Moleküle in Protein-DNA-Komplexen zeigt eine Verkürzung der Konturlänge im Vergleich zu DNA die unter den gleichen Bedingungen geschädigt wurde. Die Verkürzung von 27.7 ± 7.6 nm weist auf eine Wicklung der DNA um das hRPA Protein hin. Zusätzlich zeigen wir am Beispiel des Modellsystems aus hRPA und UV-Licht-geschädigter DNA, dass das AFM-Phasensignal eine Unterscheidung zwischen Strukturen ähnlicher Architektur, aber unterschiedlicher Herkunft in einer AFM Abbildung ermöglicht.

Das letzte Kapitel dieser Arbeit behandelt die Analyse der DNA-bindenden Eigenschaften von ORF80, ein Protein mit unbekannter physiologischer Funktion. Unsere AFM Untersuchungen zeigen, dass bei niedrigen Konzentrationen eine spezifische Bindung von ORF80 überwiegt. Zu unserer Kenntnis ist ORF80 das kleinste Protein, das mittels AFM in Komplexen mit DNA bisher untersucht wurde. Der Einsatz unserer einzelmolekularen Methoden zeigt, dass maximal zwei ORF80 Moleküle ortsspezifisch zur dsDNA binden. Dieses Ergebnis steht im Gegensatz zu Ergebnis, die vorher mittels Gelelektrophorese und Fluoreszenz-Titrations-Messungen gemacht wurden. Diese Messungen zeigten eine Bindung von mehr als zwanzig ORF80 Molekülen zu einer ortsspezifischen Stelle. Die Kombination von AFM und FCS zeigt deutlich, dass sich unter höheren ORF80 Konzentrationen größere Protein-DNA

Agglomerate ausbilden, die aus mehreren DNA und Protein Molekülen bestehen. Die Bildung solcher Agglomerate bei hohen Protein Konzentrationen kann man sowohl mit der unspezifischen ORF80 Bindung als auch durch seine hohe Agglomerationstendenz erklären. Unsere Experimente zeigen daher eindeutig, dass der Einsatz von Einzelmolekülmethoden ausgesprochen wichtig ist, wenn Proteine mit hohen Agglomerationseigenschaften untersucht werden sollen. Zusätzlich erlaubt die Auflösung des AFMs die Beobachtung von Konformationsveränderungen und strukturellen Besonderheiten von langen DNA Molekülen und ihren Komplexen mit Proteinen von unterschiedlicher Größe, was mit anderen Methoden nicht möglich ist.

7 REFERENCES

- Aboussekhra, A., Biggerstaff, M., Shivji, M. K., Vilpo, J. A., Moncollin, V., Podust, V. N., Proticacute, M., Hubscher, U., Egly, J. M., Wood et, a. (1995). Mammalian DNA nucleotide excision repair reconstituted with purified protein components, *Cell*, **80** (6): 859-868
- Abu-Lail, N. I., Camesano, T. A. (2003). Polysaccharide properties probed with atomic force microscopy, *J Microsc*, **212** (3): 217-238
- Adam, W., Marquardt, S., Saha-Möller, C. R. (1999). Oxidative DNA damage in the photolysis of N-hydroxy-2-pyridone, a specific hydroxyl-radical source, *Photochem Photobiol*, **70** (3): 287-291
- Alberts, B. (2003). DNA replication and recombination, *Nature*, **421** (6921): 431-435
- Araki, M., Masutani, C., Takemura, M., Uchida, A., Sugasawa, K., Kondoh, J., Ohkuma, Y., Hanaoka, F. (2001). Centrosome protein centrin 2/caltractin 1 is part of the xeroderma pigmentosum group C complex that initiates global genome nucleotide excision repair., *J Biol Chem*, **276** (22): 18665-18672
- Argaman, M., Golan, R., Thomson, N. H., Hansma, H. G. (1997). Phase imaging of moving DNA molecules and DNA molecules replicated in the atomic force microscope, *Nucleic Acids Res*, **25** (21): 4379-4384
- Arunkumar, A., Stauffer, M., Bochkareva, E., Bochkarev, A., Chazin, W. (2003). Independent and coordinated functions of replication protein A tandem high affinity single-stranded DNA binding domains, *J Biol Chem.*, **278** (42): 41077-41082
- Bacia, K., Schwille, P. (2003). A dynamic view of cellular processes by in vivo fluorescence auto- and cross-correlation spectroscopy, *Methods*, **29** (1): 74-85
- Barton, J. K., Lippard, S. J. (1980). Heavy metal interactions with nucleic acids, John Wiley and Sons, 31-113
- Batty, D., Raptic'Otrin, V., Levine, A., Wood, R. (2000a). Stable binding of human XPC complex to irradiated DNA confers strong discrimination for damaged sites, *J Mol Biol*, **300** (2): 275-290
- Batty, D. P., Wood, R. D. (2000b). Damage recognition in nucleotide excision repair of DNA, *Gene*, **241** (2): 193-204
- Becker, M. M., Wang, Z. (1989). Origin of ultraviolet damage in DNA, *J Mol Biol*, **210** (3): 429-438
- Beinoraviciute-Kellner, R. (2002). DNA-Bindung des Transkriptionsfaktors ABF1 aus *S.cerevisiae*: Spezifität und Kontaktpunkte, *Dissertation*, Universität Bayreuth
- Bellon, S. F., Lippard, S. J. (1990). Bending studies of DNA site-specifically modified by cisplatin, *trans*-diamminedichloroplatinum(II) and *cis*-[Pt(NH₃)₂(N₃-cytosine)Cl]⁺, *Biophys Chem*, **35** (2-3): 179-188
- Bennink, M. L., Nikova, D. N., van der Werf, K. O., Greve, J. (2003). Dynamic imaging of single DNA-protein interactions using atomic force microscopy, *Analytica Chim Acta*, **479** (1): 3-15
- Benzer, S. (1961). On the topography of the genetic fine structure, *Proc Natl Acad Sci USA*, **47**: 403-416

- Berg, R. J. W. (1994). UV-induced damage in relation to skin cancer induction in hairless mice: implications for molecular dosimetry in man, *Dissertation*, Universiteit Utrecht
- Bessho, T., Sancar, A., Thompson, L. H., Thelen, M. P. (1997). Reconstitution of human excision nuclease with recombinant XPF-ERCC1 complex, *J Biol Chem*, **272** (6): 3833-3837
- Beukers, R., Berens, W. (1960). Isolation and identification of the irradiation product of thymine, *Biochim. Biophys. Acta*, (41): 550-551
- Bezanilla, M., Manne, S., Laney, D. E., Lyubchenko, Y. L., Hansma, H. G. (1995). Adsorption of DNA to mica, silylated mica and minerals: characterisation by atomic force microscopy, *Langmuir*, **11**: 655-659
- Binnig, G., Quate, C. F., Gerber, C. (1986). Atomic force microscope, *Phys Rev Lett*, **56** (9): 930-933
- Blackwell, L. J., Borowiec, J. A. (1994). Human replication protein A binds single-stranded DNA in two distinct complexes, *Mol Cell Biol*, **14** (6): 3993-4001
- Blackwell, L. J., Borowiec, J. A., Masrangelo, I. A. (1996). Single-stranded-DNA binding alters human replication protein A structure and facilitates interaction with DNA-dependent protein kinase, *Mol Cell Biol*, **16** (9): 4798-4807
- Bochkarev, A., Pfuetzner, R. A., Edwards, A. M., Frappier, L. (1997). Structure of the single-stranded-DNA-binding domain of replication protein A bound to DNA, *Nature*, **385** (6612): 176-181
- Bochkarev, A., Bochkareva, E., Frappier, L., Edwards, A. M. (1999). The crystal structure of the complex of replication protein A subunits RPA32 and RPA14 reveals a mechanism for single-stranded DNA binding, *EMBO J*, **18** (16): 4498-4504
- Bochkarev, A., Bochkareva, E. (2004). From RPA to BRCA2: lessons from single-stranded DNA binding by the OB-fold, *Curr Opin Str Biol*, **14** (1): 36-42
- Bochkareva, E., Frappier, L., Edwards, A. M., Bochkarev, A. (1998). The RPA32 subunit of human replication protein A contains a single-stranded DNA-binding domain, *J Biol Chem*, **273** (7): 3932-3936
- Bochkareva, E., Korolev, S., Bochkarev, A. (2000). The role for zinc in replication protein A, *J Biol Chem*, **275** (35): 27332-27338
- Bochkareva, E., Belegu, V., Korolev, S., Bochkarev, A. (2001). Structure of the major single-stranded DNA-binding domain of replication protein A suggests a dynamic mechanism for DNA binding, *EMBO J*, **20** (3): 612-618
- Bochkareva, E., Korolev, S., Lees-Miller, S. P., Bochkarev, A. (2002). Structure of the RPA trimerization core and its role in the multistep DNA-binding mechanism of RPA, *EMBO J*, **21** (7): 1855-1863
- Bockris, J. O. M., Reddy, A., K, N (1977). *Modern Electrochemistry*, Plenum Press, New York
- Bose, S., Davies, R. (1984). The photoreactivity of T-A sequences in oligodeoxyribonucleotides and DNA, *Nucleic Acids Res*, **12** (20): 7903-7914
- Bouchiat, C., Wang, M. D., Allemand, J.-F., Strick, T., Block, S. M., Croquette, V. (1999). Estimating the persistence length of a worm-like chain molecule from force-extension measurements, *Biophys J*, **76** (1): 409
- Bourre, F., Renault, G., Sarasin, A. (1987). Sequence effect on alkali-sensitive sites in UV-irradiated SV40 DNA, *Nucleic Acids Res*, **15** (21): 8861-8875

- Bradley, D. F., Stellwagen, N. C., O'Konski, C. T., Paulson, C. M. (1972). Electric birefringence and dichroism of acridine orange and methylene blue complexes with polynucleotides, *Biopolymers*, **11** (3): 645-652
- Brash, D. E. (1988). UV mutagenic photoproducts in *Escherichia coli* and human cells: a molecular genetics perspective on human skin cancer, *Photochem Photobiol*, **48** (1): 59-66
- Braun, K. A., Lao, Y., He, Z., Ingles, C. J., Wold, M. S. (1997). Role of protein-protein interactions in the function of replication protein A (RPA): RPA modulates the activity of DNA polymerase by multiple mechanisms, *Biochemistry*, **36** (28): 8443-8454
- Brill, S. J., Bastin-Shanower, S. (1998). Identification and characterization of the fourth single-stranded-DNA binding domain of replication protein A, *Mol Cell Biol*, **18** (12): 7225-7234
- Burns, L., Guzder, S., Sung, P., Prakash, S., Prakash, L. (1996). An affinity of human replication protein A for ultraviolet-damaged DNA, *J Biol Chem*, **271** (20): 11607-11610
- Buschta-Hedayat, N., Buterin, T., Hess, M. T., Missura, M., Naegeli, H. (1999). Recognition of nonhybridizing base pairs during nucleotide excision repair of DNA, *Proc Natl Acad Sci USA*, **96** (11): 6090-6095
- Bustamante, C., Vesenka, J., Tang, C. L., Rees, W., Guthold, M., Keller, R. (1992). Circular DNA molecules imaged in air by scanning force microscopy, *Biochemistry*, **31** (1): 22-26
- Bustamante, C., Marko, J. F., Siggia, E. D., Smith, S. (1994). Entropic elasticity of lambda-phage DNA, *Science*, **265** (5178): 1599-600
- Bustamante, C., Rivetti, C., Keller, D. J. (1997). Scanning force microscopy under aqueous solutions, *Curr Opin Struct Biol*, **7** (5): 709-716
- Bustamante, C., Guthold, M., Zhu, X., Yang, G. (1999). Facilitated target location on DNA by individual *Escherichia coli* RNA polymerase molecules observed with the scanning force microscope operating in liquid, *J Biol Chem*, **274** (24): 16665-16668
- Cadet, J., Anselmino, C., Douki, T., Voituriez, L. (1992). Photochemistry of nucleic acids in cells, *Photochem Photobiol*, **15** (4): 277-298
- Cary, R. B., Peterson, S. R., Wang, J., Bear, D. G., Bradbury, E. M., Chen, D. J. (1997). DNA looping by Ku and the DNA-dependent protein kinase, *Proc Natl Acad Sci USA*, **94** (9): 4267-4272
- Chadwick, K. H., Leenhouts, H. P. (1994). On the linearity of the dose-effect relationship of DNA double strand breaks, *I J Rad Biol*, **66** (5): 549-552
- Cherny, D. I., Jovin, T. M. (2001). Electron and Scanning Force Microscopy Studies of Alterations in Supercoiled DNA Tertiary Structure., *J Mol Biol*, **313** (2): 295-307
- Cleaver, J. E., Cortes, F., Karentz, D., Lutze, L. H., Morgan, W. F., Player, A. N., Vuksanovic, L., Mitchell, D. L. (1988). The relative biological importance of cyclobutane and (6-4) pyrimidine-pyrimidone dimer photoproducts in human cells: evidence from a *xeroderma pigmentosum* revertant, *Photochem Photobiol*, **48** (1): 41-49

- Clugston, C., McLaughlin, K., Kenny, M., Brown, R. (1992). Binding of human single-stranded DNA binding protein to DNA damaged by the anticancer drug cis-diamminedichloroplatinum (II). *Cancer Res.*, **52** (22): 6375-9
- Cohen, G. L., Bauer, W. R., Barton, J. K., Lippard, S. J. (1979). Binding of cis- and trans-dichlorodiammineplatinum(II) to DNA: evidence for unwinding and shortening of the double helix, *Science*, **203** (4384): 1014-1016
- Confocor2 (2001). Applications handbook, Advanced Imaging Microscopy, Carl Zeiss
- Corongiu, G., Clementi, E. (1981). Simulations of the solvent structure for macromolecules: solvation model for B-DNA and Na⁺-B-DNA double helix at 300 degrees K, *Ann NY Acad Sci*, **367**: 83-107
- Coste, F., Malinge, J., Serre, L., Shepard, W., Roth, M., Leng, M., Zelwer, C. (1999). Crystal structure of a double-stranded DNA containing a cisplatin interstrand cross-link at 1.63 Å resolution: hydration at the platinated site, *Nucleic Acids Res*, **27** (8): 1837-1846
- Cotton, F. A., Wilkinson, G. (1972). Advanced Inorganic Chemistry, Interscience Publishers
- Dank, N. (1997). Ortspezifische Quervernetzung von Protein-DNA-Komplexen unter Verwendung von 5-Iod-2'- desoxyuridin als Chromophor, *Dissertation*, Universität Bayreuth
- de Boer, J., Hoeijmakers, J. H. J. (2000). Nucleotide excision repair and human syndromes, *Carcinogenesis*, **21** (3): 453-460
- de Laat, W. L., Appeldoorn, E., Jaspers, N. G., Hoeijmakers, J. H. (1998). DNA structural elements required for ERCC1-XPF endonuclease activity, *J Biol Chem*, **273** (14): 7835-7842
- de Laat, W. L., Jaspers, N. G. J., Hoeijmakers, J. H. J. (1999). Molecular mechanism of nucleotide excision repair, *Genes Dev*, **13** (7): 768-785
- de Pauw-Gillet, M. C., Houssier, C., Fredericq, E. (1979). Interaction of DNA and purine nucleosides with cis-dichlorodiammineplatinum(II) and antimitotic activity of the complexes on meristematic root cells, *Chem-Biol Interact*, **25** (1): 87-102
- den Hartog, J., Altona, C., van Boom, J., Marcelis, A., van der Marel, G., Rinkel, L., Wille-Hazeleger, G., Reedijk, J. (1983). Cis-Platinum induced distortions in DNA. Conformational analysis of d(GpCpG) and cis-pt(NH₃)₂[d(GpCpG)], studied by 500-MHz NMR, *Eur J Biochem.*, **134** (3): 134-95
- den Hartog, J. (1985). Cisplatin induced distortions in DNA: structure and conformation of oligonucleotide-platinum adducts, *Dissertation*, Universität Leiden
- Dodonova, N. Y. (1993). Vacuum UV--photophysics and photochemistry of biomolecules, *Photochem Photobiol*, **18** (2-3): 111-121
- Doll, R., Peto, R. (1981). The causes of cancer: quantitative estimates of avoidable risks of cancer in the United States today, *J Natl Cancer Inst.*, **66** (6): 1191-308
- Dong, J., Park, J.-S., Lee, S.-H. (1999). *In vitro* analysis of the zinc-finger motif in human replication protein A, *Biochem J*, **337** (2): 311-317
- Drapkin, R., Reardon, J. T., Ansari, A., Huang, J. C., Zawel, L., Ahn, K., Sancar, A., Reinberg, D. (1994). Dual role of TFIIH in DNA excision repair and in transcription by RNA polymerase II, *Nature*, **368** (6473): 769-772

- Dufrene, Y. F., Lee, G. (2000). Advances in the characterization of supported lipid films with the atomic force microscope, *Biochim Biophys Acta*, **1509** (1-2): 14-41
- Eastman, A. (1985). Interstrand cross-links and sequence specificity in the reaction of *cis*-dichloro(ethylenediamine)platinum(II) with DNA, *Biochemistry*, **24** (19): 5027-32
- Ebel, H., Gunther, T. (1980). Magnesium metabolism: a review, *J Clin Chem Clin Biochem*, **18** (5): 257-270
- Eckerich, C., Fackelmayer, F. O., Knippers, R. (2001). Zinc affects the conformation of nucleoprotein filaments formed by replication protein A (RPA) and long natural DNA molecules, *Biochim Biophys Acta*, **1538** (1): 67-75
- Ehrenberg, M., Rigler, R. (1974). Rotational brownian motion and fluorescence intensify fluctuations, *Chemical Physics*, **4** (3): 390-401
- Elizondo-Riojas, M.-A., Kozelka, J. (2001). Unrestrained 5 ns molecular dynamics simulation of a cisplatin-DNA 1,2-GG adduct provides a rationale for the NMR features and reveals increased conformational flexibility at the platinum binding site1, *J Mol Biol*, **314** (5): 1227-1243
- Evans, E., Moggs, J. G., Hwang, J. R., Egly, J. M., Wood, R. D. (1997). Mechanism of open complex and dual incision formation by human nucleotide excision repair factors, *EMBO J*, **16** (21): 6559-6573
- Fang, Y., Hoh, J. H. (1998). Early intermediates in spermidine-induced DNA condensation on the surface of mica, *J Am Chem Soc*, **120** (35): 8903-8909
- Fang, Y., Spisz, T. S., Hoh, J. H. (1999). Ethanol-induced structural transitions of DNA on mica, *Nucleic Acids Res*, **27** (8): 1943-1949
- Feng, X. Z., Bash, R., Balagurumoorthy, P., Lohr, D., Harrington, R. E., Lindsay, S. M. (2000). Conformational transition in DNA on a cold surface, *Nucleic Acids Res*, **28** (2): 593-596
- Fichtinger-Schepman, A., van der Veer, J., den Hartog, J., Lohman, P., Reedijk, J. (1985). Adducts of the antitumor drug *cis*-diamminedichloroplatinum(II) with DNA: formation, identification, and quantitation, *Biochemistry*, **24** (3): 707-713
- Foldes-Papp, Z., Rigler, R. (2001). Quantitative two-color fluorescence cross-correlation spectroscopy in the analysis of polymerase chain reaction., *Biol Chem*, **382** (3): 473-478
- Folkard, M., Prise, K. M., Turner, C. J., Michael, B. D. (2002). The production of single strand and double strand breaks in DNA in aqueous solution by vacuum UV photons below 10 eV, *Radiat Prot Dosimetry*, **99** (1-4): 147-149
- Friedberg, E., Bardwell, A., Bardwell, L., Feaver, W., Kornberg, R., Svejstrup, J., Tomkinson, A., Wang, Z. (1995). Nucleotide excision repair in the yeast *Saccharomyces cerevisiae*: its relationship to specialized mitotic recombination and RNA polymerase II basal transcription, *Philos Trans R Soc Lond B Biol Sci*, **347** (1319): 63-68
- Gallagher, P. E., Duker, N. J. (1989). Formation of purine photoproducts in a defined human DNA sequence, *Photochem Photobiol*, **49** (5): 599-605
- Gangulie, P. K., Theophanides, T. (1979). Preferential interstrand cross-linking of DNA rich in guanine and cytosine by *cis*-dichlorodiammineplatinum(II), *Eur J Biochem*, **101** (2): 377-83

- Gasparro, F., Fresco, J. (1986). Ultraviolet-induced 8,8-adenine dehydrodimers in oligo- and polynucleotides, *Nucleic Acids Res*, **14** (10): 4239
- Gelasco, A., Lippard, S. (1998). NMR solution structure of a DNA dodecamer duplex containing a *cis*-diammineplatinum(II) d(GpG) intrastrand cross-link, the major adduct of the anticancer drug cisplatin, *Biochemistry*, **37** (26): 9230-9239
- Georgaki, A., Hubscher, U. (1993). DNA unwinding by replication protein A is a property of the 70 kDa subunit and is facilitated by phosphorylation of the 32 kDa subunit, *Nucleic Acids Res*, **21** (16): 3659-3665
- Gomes, X. V., Henricksen, L. A., Wold, M. S. (1996). Proteolytic mapping of human replication protein A: evidence for multiple structural domains and a conformational change upon interaction with single-stranded DNA, *Biochemistry*, **35** (17): 5586-5595
- Gonzalez, V. M., Fuertes, M. A., Perez, J. M., Alonso, C. (1998). Kinetics of the salt-induced B- to Z-DNA transition, *Eur Biophys J*, **27** (4): 417-423
- Grandi, P., Eltsov, M., Nielsen, I., Raska, I. (2001). DNA double-strand breaks induce formation of RP-A/Ku foci on in vitro reconstituted *Xenopus* sperm nuclei, **114**
- Gunz, D., Hess, M., Naegeli, H. (1996). Recognition of DNA adducts by human nucleotide excision repair. Evidence for a thermodynamic probing mechanism, *J Biol Chem*, **271** (41): 25089-25098
- Guthold, M., Bezanilla, M., Erie, D., Jenkins, B., Hansma, H., Bustamante, C. (1994). Following the assembly of RNA polymerase-DNA complexes in aqueous solutions with the scanning force microscope, *Proc Natl Acad Sci USA*, **91** (26): 12927
- Guthold, M., Zhu, X., Rivetti, C., Yang, G., Thomson, N. H., Kasas, S., Hansma, H. G., Smith, B., Hansma, P. K., Bustamante, C. (1999). Direct observation of one-dimensional diffusion and transcription by *Escherichia coli* RNA polymerase, *Biophys J*, **77** (4): 2284-2294
- Guzder, S. N., Habraken, Y., Sung, P., Prakash, L., Prakash, S. (1995). Reconstitution of yeast nucleotide excision repair with purified Rad proteins, replication protein A, and transcription factor TFIIH, *J Biol Chem*, **270** (22): 12973-12976
- Han, W., Landsay, S., Dlakic, M., Harrington, R. E. (1997). Kinked DNA, *Nature*, **386** (6625): 563
- Hansma, H. G., Weisenhorn, A. L., Edmundson, A. B., Gaub, H. E., Hansma, P. K. (1991). Atomic force microscopy: seeing molecules of lipid and immunoglobulin, *Clin Chem*, **37** (9): 1497-1501
- Hansma, H. G., Sinsheimer, R. L., Li, M. Q., Hansma, P. K. (1992a). Atomic force microscopy of single- and double-stranded DNA, *Nucl Acids Res*, **20** (14): 3585-3590
- Hansma, H. G., Vesenka, J., Siegerist, C., Kelderman, G., Morrett, H., Sinsheimer, R. L., Elings, V., Bustamante, C., Hansma, P. K. (1992b). Reproducible imaging and dissection of plasmid DNA under liquid with the atomic force microscope, *Science*, **256** (5060): 1180-1184
- Hansma, H. G., Bezanilla, M., Zenhausern, F., Adrian, M., Sinsheimer, R. L. (1993). Atomic force microscopy of DNA in aqueous solutions, *Nucleic Acids Res*, **21** (3): 505-512

- Hansma, H. G., Laney, D. E., Bezanilla, M., Sinsheimer, R. L., Hansma, P. K. (1995). Applications for atomic force microscopy of DNA, *Biophys J*, **68** (5): 1672-1677
- Hansma, H. G., Laney, D. E. (1996a). DNA binding to mica correlates with cationic radius: assay by atomic force microscopy, *Biophys J*, **70** (4): 1933-1939
- Hansma, H. G., Revenko, I., Kim, K., Laney, D. E. (1996b). Atomic force microscopy of long and short double-stranded, single-stranded and triple-stranded nucleic acids, *Nucleic Acids Res*, **24** (4): 713-720
- Hansma, H. G., Kim, K. J., Laney, D. E., Garcia, R. A., Argaman, M., Allen, M. J., Parsons, S. M. (1997). Properties of biomolecules measured from atomic force microscope images: A review, *J. Struct. Biol.*, **119** (2): 99-108
- Hansma, H. G., Pietrasanta, L. I., Auerbach, I. D., Sorenson, C., Golan, R., Holden, P. A. (2000). Probing biopolymers with the atomic force microscope: A review, *J Biomater Sci*, **11** (7): 675-683
- Hansma, P. K., Elings, V. B., Marti, O., Bracker, C. E. (1988). Scanning tunneling microscopy and atomic force microscopy: application to biology and technology, *Science*, **242** (4876): 209-216
- Hartmann, U. (1991). van der Waals interactions between sharp probes and flat sample surfaces, *Phys Rev B*, **43** (3): 2404-2407
- He, Z., Henricksen, L. A., Wold, M. S., Ingles, C. J. (1995). RPA involvement in the damage-recognition and incision steps of nucleotide excision repair, *Nature*, **374** (6522): 566-569
- Hermann, D., Houssier, C., Guschlbauer, W. (1979). Dissociation of double-stranded poly(I) . poly(C) by *cis*-diammine-dichloro-Pt(II), *Biochim Biophys Acta*, **564**: 456-472
- Hey, T., Lipps, G., Krauss, G. (2001). Binding of XPA and RPA to damaged DNA investigated by fluorescence anisotropy, *Biochemistry*, **40** (9): 2901-10
- Hey, T. (2002a). Das Problem der Erkennung von DNA-Schäden bei der humanen Nukleotid-Exzisions-Reparatur, *Dissertation*, Universität Bayreuth
- Hey, T., Lipps, G., Sugasawa, K., Iwai, S., Hanaoka, F., Krauss, G. (2002b). The XPC-HR23B complex displays high affinity and specificity for damaged DNA in a true-equilibrium fluorescence assay, *Biochemistry*, **41** (21): 6583-6587
- Hieda, K., Suzuki, K., Hirono, T., Suzuki, M., Furusawa, Y. (1994). Single- and double-strand breaks in pBR322 DNA by vacuum-UV from 8.3 to 20.7 eV., *J Radiat Res*, **35** (2): 104-111
- Horiguchi, M., Masumura, K.-i., Ikehata, H., Ono, T., Kanke, Y., Nohmi, T. (2001). Molecular nature of ultraviolet B light-induced deletions in the murine epidermis, *Cancer Res*, **61** (10): 3913
- Horsfall, M. J., Lawrence, C. W. (1994). Accuracy of Replication Past the T-C (6-4) Adduct, *J Mol Biol*, **235** (2): 465-471
- Huang, H., Zhu, L., Reid, B., Drobny, G., Hopkins, P. (1995). Solution structure of a cisplatin-induced DNA interstrand cross-link, *Science*, **270** (5243): 1842-1845
- Huq, F., Peter, M. C. R. (2000). Interaction between NiCl₂, and nucleobases, nucleosides and nucleotides, *J Inorg Biochem*, **78** (3): 217-226
- Husain, I., Griffith, J., Sancar, A. (1988). Thymine dimers bend DNA, *Proc Natl Acad Sci USA*, **85** (8): 2558-62

- Ichihashi, M., Ueda, M., Budiyo, A., Bito, T., Oka, M., Fukunaga, M., Tsuru, K., Horikawa, T. (2003). UV-induced skin damage, *Toxicology*, **189** (1-2): 21-39
- Iftode, C., Daniely, Y., Borowiec, J. A. (1999). Replication protein A: The eukaryotic SSB, *Crit Rev Biochem Mol Biol*, **34** (3): 141-180
- Israelachvili, J. (1997). Intermolecular & Surface Forces, Academic Press, Harcourt Brace & Company, Publishers
- Janicijevic, A., Sugawara, K., Shimizu, Y., Hanaoka, F., Wijgers, N., Djurica, M., Hoeijmakers, J. H. J., Wyman, C. (2003). DNA bending by the human damage recognition complex XPC-HR23B, *DNA Repair*, **2** (3): 325-336
- Jankowski, T., Janka, R. (2001). ConfoCor 2 - The Second Generation of Fluorescence Correlation Microscopies:
- Kasas, S., Thomson, N. H., Smith, B. L., Hansma, H. G., Zhu, X., Guthold, M., Bustamante, C., Kool, E. T., Kashlev, M., Hansma et al. (1997). Escherichia coli RNA polymerase activity observed using atomic force microscopy, *Biochemistry*, **36** (3): 461-468
- Kaspárková, J., Mellish, K., Qu, Y., Brabec, V., Farrell, N. (1996). Site-specific d(GpG) intrastrand cross-links formed by dinuclear platinum complexes. Bending and NMR studies, *Biochemistry*, **35** (51): 16705-16713
- Kawanishi, S., Hiraku, Y., Murata, M., Oikawa, S. (2002). The role of metals in site-specific DNA damage with reference to carcinogenesis, *Free Radical Biol Med*, **32** (9): 822-832
- Keeling, P. J., Klenk, H. P., Singh, R. K., Feeley, O., Schleper, C., Zillig, W., Doolittle, W. F., Sensen, C. W. (1996). Complete nucleotide sequence of the *Sulfolobus islandicus* multicopy plasmid pRN1, *Plasmid*, **35** (2): 141-144
- Keller, D. (1998). Making movies of molecular motions, *Biophys J*, **74** (6): 2743-2744
- Kettling, U., Koltermann, A., Schwille, P., Eigen, M. (1998). Real-time enzyme kinetics monitored by dual-color fluorescence cross-correlation spectroscopy, *Proceedings of the National Academy of Sciences Proc Natl Acad Sci USA*, **95** (4): 1416-1420
- Kim, C., Snyder, R. O., Wold, M. S. (1992). Binding properties of replication protein A from human and yeast cells, *Molec Cell Biol*, **12** (7): 3050-3059
- Kim, C., Paulus, B. F., Wold, M. S. (1994). Interactions of human replication protein A with oligonucleotides, *Biochemistry*, **33** (47): 14197-14206
- Kim, C., Wold, M. S. (1995a). Recombinant human replication protein A binds to polynucleotides with low cooperativity, *Biochemistry*, **34** (6): 2058-2064
- Kim, J. K., Choi, B. S. (1995b). The solution structure of DNA duplex-decamer containing the (6-4) photoproduct of thymidylyl(3'-->5')thymidine by NMR and relaxation matrix refinement, *FEBS Lett*, **228** (3): 849-854
- Kim, J. K., Patel, D., Choi, B. S. (1995c). Contrasting structural impacts induced by cis-syn cyclobutane dimer and (6-4) adduct in DNA duplex decamers: implication in mutagenesis and repair activity, *Photochem Photobiol*, **62** (1): 44-50
- Kim, J. K., Soni, S. D., Arakali, A. V., Wallace, J. C., Alderfer, J. L. (1995d). Solution structure of a nucleic acid photoproduct of deoxyfluorouridylyl-(3'-5')-thymidine monophosphate (d-FpT) determined by NMR and restrained molecular dynamics: structural comparison of two sequence isomer photoadducts (d-U5p5T and d-T5p5U), *Nucleic Acids Res*, **23** (10): 1810-1815

- Kinjo, M., Rigler, R. (1995). Ultrasensitive hybridization analysis using fluorescence correlation spectroscopy, *Nucleic Acids Res*, **23** (10): 1795-1799
- Knoll, A. (2003). Equilibrium and dynamic phase behavior in thin films of cylinder-forming block copolymers, *Dissertation*, Universität Bayreuth
- Kolpashchikov, D. M., Khodyreva, S. N., Khlimankov, D. Y., Wold, M. S., Favre, A., Lavrik, O. I. (2001). Polarity of human replication protein A binding to DNA, *Nucleic Acids Res (Online)*, **29** (2): 373-379
- Kraemer, K. H. (1989). Human model systems for studies of skin cancer, *Prog Clin Biol Res*, **298**: 25-33
- Kusumoto, R., Masutani, C., Sugasawa, K., Iwai, S., Araki, M., Uchida, A., Mizukoshi, T., Hanaoka, F. (2001). Diversity of the damage recognition step in the global genomic nucleotide excision repair *in vitro*, *Mutat Res*, **485** (3): 219-227
- Lal, R., John, S. A. (1994). Biological applications of atomic force microscopy, *The Am J of Physiol*, **266** (1): 1-21
- Lao, Y., Gomes, X. V., Ren, Y., Taylor, J. S., Wold, M. S. (2000). Replication protein A interactions with DNA. III. Molecular basis of recognition of damaged DNA., *Biochemistry*, **39** (5): 850-9
- Lavrik, O. I., Kolpashchikov, D. M., Weissart, K., Nasheuer, H.-P., Khodyreva, S. N., Favre, A. (1999). RPA subunit arrangement near the 3'-end of the primer is modulated by the length of the template strand and cooperative protein interactions, *Nucl Acids Res*, **27** (21): 4235-4240
- Lee, B.-S., Bi, L., Garfinkel, D. J., Bailis, A. M. (2000). Nucleotide excision repair/TFIIH helicases Rad3 and Ssl2 inhibit short- sequence recombination and Ty1 retrotransposition by similar mechanisms, *Mol Cell Biol*, **20** (7): 2436-2445
- Levadny, V., Belaya, M., Pink, D., Jericho, M. (1996). heory of electrostatic effects in soft biological interfaces using atomic force microscopy., *Biophys J*, **70** (4): 1745-45
- Li, L., Elledge, S. J., Peterson, C. A., Bales, E. S., Legerski, R. J. (1994). Specific association between the human DNA repair proteins XPA and ERCC1, *Proc Natl Acad Sci USA*, **91** (11): 5012-5016
- Lippke, J. A., Gordon, L. K., Brash, D. E., Haseltine, W. A. (1981). Distribution of UV light-induced damage in a defined sequence of human DNA: detection of alkaline-sensitive lesions at pyrimidine nucleoside-cytidine sequences, *Proc Natl Acad Sci USA*, **78** (6): 3388-3392
- Lipps, G., Ibanez, P., Stroessenreuther, T., Hekimian, K., Krauss, G. (2001). The protein ORF80 from the acidophilic and thermophilic archaeon *Sulfolobus islandicus* binds highly site-specifically to double-stranded DNA and represents a novel type of basic leucine zipper protein, *Nucleic Acids Res*, **29** (24): 4973-4982
- Lysetska, M., Knoll, A., Boehringer, D., Hey, T., Krauss, G., Krausch, G. (2002). UV light-damaged DNA and its interaction with human replication protein A: an atomic force microscopy study, *Nucleic Acids Res*, **30** (12): 2686-2691
- Lyubchenko, Y. L., Shlyakhtenko, L. S. (1997). Visualization of supercoiled DNA with atomic force microscopy *in situ*, *Proc Natl Acad Sci USA*, **94** (2): 496-501
- Macquet, J. P., Butour, J. L. (1978). Modifications of the DNA secondary structure upon platinum binding: a proposed model, *Biochimie*, **60** (9): 901-914

- Magde, D., Elson, E., Webb, W. W. (1972). Thermodynamic Fluctuations in a Reacting System—Measurement by Fluorescence Correlation Spectroscopy, *Phys Rev Lett*, (29): 705-708
- Magde, D., Elson, E. L., Webb, W. W. (1974). Fluorescence correlation spectroscopy. II. An experimental realization., *Biopolymers*, **13** (1): 29-61
- Malinge, J., Giraud-Panis, M., Leng, M. (1999). Interstrand cross-links of cisplatin induce striking distortions in DNA, *J Inorg Biochem.*, **77** (1-2): 23-9
- Mansy, S., Rosenberg, B., Thomson, A. J. (1973). Binding of *cis*- and *trans*-dichlorodiammineplatinum(II) to nucleosides. I. Location of the binding sites, *J Am Chem Soc*, **95** (5): 1633-1640
- Marsh, T. C., Vesenka, J., Henderson, E. (1995). A new DNA nanostructure, the G-wire, imaged by scanning probe microscopy, *Nucleic Acids Res*, **23** (4): 696-700
- Marti, O., Drake, B., Hansma, P. K. (1987). Atomic force microscopy of liquid-covered surfaces: atomic resolution images, *Appl Phys Lett*, **51** (7): 484-486
- Matsuda, T., Saijo, M., Kuraoka, I., Kobayashi, T., Nakatsu, Y., Nagai, A., Enjoji, T., Masutani, C., Sugasawa, K. (1995). DNA repair protein XPA binds replication protein A, *J Biol Chem*, **270** (8): 4152-4157
- Matsunaga, T., Park, C. H., Bessho, T., Mu, D., Sancar, A. (1996). Replication protein A confers structure-specific endonuclease activities to the XPF-ERCC1 and XPG subunits of human DNA repair excision nuclease, *J Biol Chem*, **271** (19): 11047-11050
- McAteer, K., Jing, Y., Kao, J., Taylor, J.-S., Kennedy, M. A. (1998). Solution-state Structure of a DNA Dodecamer Duplex Containing a *Cis*-Syn Thymine Cyclobutane Dimer, the Major UV Photoproduct of DNA., *J Mol Biol*, **282** (5): 1013-1032
- McIlwraith, M. J., Van Dyck, E., Masson, J.-Y., Stasiak, A. Z., Stasiak, A., West, S. C. (2000). Reconstitution of the strand invasion step of double-strand break repair using human Rad51 Rad52 and RPA proteins1, *J Mol Biol*, **304** (2): 151-164
- McLachlan, G. A., Muller, J. G., Rokita, S. E., Burrows, C. J. (1996). Metal-mediated oxidation of guanines in DNA and RNA: a comparison of cobalt(II), nickel(II) and copper(II) complexes, *Inorg Chim Acta*, **251** (1-2): 193-199
- Medina, M., Schwille, P. (2002). Fluorescence correlation spectroscopy for the detection and study of single molecules in biology, *BioEssays*, **24** (8): 758-764
- Meseth, U., Wohland, T., Rigler, R., Vogel, H. (1999). Resolution of Fluorescence Correlation Measurements, *Biophys J*, **76** (3): 1619-1631
- Mills, J. B., Vacano, E., Hagerman, P. J. (1999). Flexibility of single-stranded DNA: Use of gapped duplex helices to determine the persistence lengths of Poly(dT) and Poly(dA), *J Mol Biol*, **285** (1): 245-257
- Minasov, G., Tereshko, V., Egli, M. (1999). Atomic-resolution Crystal Structures of B - DNA Reveal Specific Influences of Divalent Metal Ions on Conformation and Packing, *J Mol Biol*, **291** (1): 83-99
- Missura, M., Buterin, T., Hindges, R., Hubscher, U., Kasparikova, J., Brabec, V., Naegeli, H. (2001). Double-check probing of DNA bending and unwinding by XPA-RPA: An architectural function in DNA repair, *EMBO J*, **20** (13): 3554-3564

- Mitchell, D., Jen, J., Cleaver, J. (1992). Sequence specificity of cyclobutane pyrimidine dimers in DNA treated with solar (ultraviolet B) radiation, *Nucleic Acids Res*, **20** (2): 225
- Mitchell, D. L., Nairn, R. S. (1989). The biology of the (6-4) photoproduct, *Photochem Photobiol*, **49** (6): 805-819
- Mitsis, P. G., Kowalczykowski, S. C., Lehman, I. R. (1993). A single-stranded DNA binding protein from *Drosophila melanogaster*: characterization of the heterotrimeric protein and its interaction with single-stranded DNA., *Biochemistry*, **32** (19): 5257-5266
- Miura, N., Miyamoto, I., Asahina, H., Satokata, I., Tanaka, K., Okada, Y. (1991). Identification and characterization of xpac protein, the gene product of the human XPAC (*xeroderma pigmentosum* group A complementing) gene, *J Biol Chem*, **266** (29): 19786-19789
- Mizukoshi, T., Kodama, T. S., Fujiwara, Y., Furuno, T., Nakanishi, M., Iwai, S. (2001). Structural study of DNA duplexes containing the (6-4) photoproduct by fluorescence resonance energy transfer, *Nucleic Acids Res*, **29** (24): 4948-4954
- Moldrheim, E., Andersen, B., Froystein, N. A., Sletten, E. (1998). Interaction of manganese(II), cobalt(II) and nickel(II) with DNA oligomers studied by 1H NMR spectroscopy, *Inorg Chim Acta*, **273** (1-2): 41-46
- Mong, S., Huang, C. H., Prestayko, A. W., Crooke, S. T. (1980). Interaction of cis-diamminedichloroplatinum(II) with PM-2 DNA, *Cancer Res*, **40** (9): 3313
- Mong, S., Daskal, Y., Prestayko, A. W., Crooke, S. T. (1981). DNA supercoiling, shortening, and induction of single-strand regions by cis-diamminedichloroplatinum(II), *Cancer. Res.*, **41** (10): 4020-4026
- Monjardet-Bas, V., Bombard, S., Chottard, J. C., Kozelka, J. (2003). GA and AG sequences of DNA react with cisplatin at comparable rates, *Chemistry*, **9** (19): 4739-4745
- Mou, J., Czajkowsky, D. M., Zhang, Y., Shao, Z. (1995). High-resolution atomic-force microscopy of DNA: the pitch of the double helix, *FEBS Lett*, **371** (3): 279-282
- Mu, D., Hsu, D. S., Sancar, A. (1996). Reaction mechanism of human DNA repair excision nuclease, *J Biol Chem*, **271** (14): 8285-8294
- Muller, D. J., Fotiadis, D., Scheuring, S., Muller, S. A., Engel, A. (1999a). Electrostatically balanced subnanometer imaging of biological specimens by atomic force microscope, *Biophys J*, **76** (2): 1101-1111
- Muller, D. J., Anderson, K. (2002). Biomolecular imaging using atomic force microscopy, *Trends Biotech*, **20** (8): 45-49
- Muller, J. G., Kayser, L. A., Paikoff, S. J., Duarte, V., Tang, N., Perez, R. J., Rokita, S. E., Burrows, C. J. (1999b). Formation of DNA adducts using nickel(II) complexes of redox-active ligands: a comparison of salen and peptide complexes, *Coord Chem Rev*, **185-186**: 761-774
- MultiModeTM SPM Instruction Manual (1999). Digital Instruments, Veeco Metrology Group,
- Munchhausen, L. L., Rahn, R. O. (1975). ???, *Biochim. Biophys. Acta*, **414**: 242
- Murakami, M., Hirokawa, H., Hayata, I. (2000a). Analysis of radiation damage of DNA by atomic force microscopy in comparison with agarose gel electrophoresis studies, *J Biochem Biophys Methods*, **44** (1-2): 31-40

- Murakami, M., Hirokawa, H., Hayata, I. (2000b). Analysis of radiation damage of DNA by atomic force microscopy in comparison with agarose gel electrophoresis studies, *Journal of Biochemical and Biophysical Methods*, **44** (1-2): 31-40
- Nocentini, S., Coin, F., Saijo, M., Tanaka, K., Egly, J. M. (1997). DNA damage recognition by XPA protein promotes efficient recruitment of transcription factor II H, *J Biol Chem*, **272** (37): 22991-22994
- Oakley, G. G., Loberg, L. I., Yao, J., Risinger, M. A., Yunker, R. L., Zernik-Kobak, M., Khanna, K. K., Lavin, M. F., Carty, M. P., Dixon, K. (2001). UV-induced hyperphosphorylation of replication protein a depends on DNA replication and expression of ATM protein, *Molec Biol Cell*, **12** (5): 1199-1213
- Oh, E. Y., Grossman, L. (1986). The effect of *Escherichia coli* Uvr protein binding on the topology of supercoiled DNA, *Nucl Acids Res*, **14** (21): 8557-8571
- Onoa, G., Cervantes, G., Moreno, V., Prieto, M. (1998). Study of the interaction of DNA with cisplatin and other Pd(II) and Pt(II) complexes by atomic force microscopy, *Nucl Acids Res*, **26** (6): 1473-1480
- Onoa, G. B., Moreno, V. (2002). Study of the modifications caused by cisplatin, transplatin, and Pd(II) and Pt(II) mepirizole derivatives on pBR322 DNA by atomic force microscopy, *Int J Pharm*, **245** (1-2): 55-65
- Pang, D., Popescu, G., Rodgers, J., Berman, B. L., Dritschilo, A. (1996). Atomic force microscopy investigation of radiation-induced DNA double strand breaks, *Scan Microsc*, **10** (4): 1105-1109; discussion 1109-1110
- Pang, D., Vidic, B., Rodgers, J., Berman, B. L., Dritschilo, A. (1997a). Atomic force microscope imaging of DNA and DNA repair proteins: applications in radiobiological research, *Rad Oncolog Investig*, **5** (4): 163-169
- Pang, D., Yoo, S., Dynan, W. S., Jung, M., Dritschilo, A. (1997b). Ku proteins join DNA fragments as shown by atomic force microscopy, *Cancer Res*, **57** (8): 1412-1415
- Pang, D., Chasovskikh, S., Cohen, J. S., Obcemea, C., Dritschilo, A. (2000). Atomic force microscopy examination of conformations of polynucleotides in response to platinum isomers: Significance of GC content at broken ends, *I J Cancer*, **90** (2): 68-72
- Paquet, F., Perez, C., Leng, M., Lancelot, G., Malinge, J. (1996). NMR solution structure of a DNA decamer containing an interstrand cross-link of the antitumor drug *cis*-diamminedichloroplatinum (II), *J Biomol Struct Dyn*, **14** (1): 67-77
- Park, C. H., Sancar, A. (1994). Formation of a ternary complex by human XPA, ERCC1, and ERCC4(XPF) excision repair proteins, *Proc Natl Acad Sci USA*, **91** (11): 5017-5021
- Park, H., Zhang, K., Ren, Y., Nadji, S., Sinha, N., Taylor, J.-S., Kang, C. (2002). Crystal structure of a DNA decamer containing a *cis-syn* thymine dimer, *Proc Natl Acad Sci USA*, **99** (25): 15965
- Park, J.-S., Wang, M., Park, S.-J., Lee, S.-H. (1999). Zinc finger of replication protein A, a non-DNA binding element, regulates its DNA binding activity through redox, *J Biol Chem*, **274** (41): 29075-29080
- Parris, C. N., Levy, D. D., Jessee, J., Seidman, M. M. (1994). Proximal and distal effects of sequence context on ultraviolet mutational hotspots in a shuttle vector replicated in *Xeroderma* cells, *J Mol Biol*, **236** (2): 491-502

- Patrick, S. M., Turchi, J. J. (1999). Replication protein A (RPA) binding to duplex cisplatin-damaged DNA is mediated through the generation of single-stranded DNA, *J Biol Chem.*, **274** (21): 14972-14978
- Philipova, D., Mullen, J. R., Maniar, H. S., Lu, J., Gu, C., Brill, S. J. (1996). A hierarchy of SSB protomers in replication protein A, *Genes Dev*, **10** (17): 2222-2233
- Pietrasanta, L. I., Thrower, D., Hsieh, W., Rao, S., Stemmann, O., Lechner, J., Carbon, J., Hansma, H. (1999). Probing the *Saccharomyces cerevisiae* centromeric DNA (CEN DNA)-Binding factor 3 (CBF3) kinetochore complex by using atomic force microscopy, *Proc Natl Acad Sci USA*, **96** (7): 3757-3762
- Potaman, V. N., Bissler, J. J., Hashem, V. I., Oussatcheva, E. A., Lu, L., Shlyakhtenko, L. S., Lyubchenko, Y. L., Matsuura, T., Ashizawa, T., Leffak, M. (2003). Unpaired Structures in SCA10 (ATTCT)_n(AGAAT)_n Repeats, *J Mol Biol*, **326** (4): 1095-1111
- Prise, K. M., Folkard, M., Michael, B. D., Vojnovic, B., Brocklehurst, B., Hopkirk, A., Munro, I. H. (2000). Critical energies for SSB and DSB induction in plasmid DNA by low-energy photons: action spectra for strand-break induction in plasmid DNA irradiated in vacuum, *Int J Radiat Biol*:
- Rampino, N. J. (1992). Cisplatin induced alterations in oriented fibers of DNA studied by atomic force microscopy, *Biochem Biophys Res Commun*, **182** (1): 201-207
- Revet, B., Malinge, J. M., Delain, E., Le Bret, M., Leng, M. (1984). Electron microscopic measurement of chain flexibility of poly(dG-dC).poly(dG-dC) modified by *cis*-diamminedichloroplatinum(II), *Nucleic Acids Res*, **12** (22): 8349-8362
- Rippe, K., Guthold, M., von Hippel, P. H., Bustamante, C. (1997). Transcriptional activation via DNA-looping: visualization of intermediates in the activation pathway of *E. coli* RNA polymerase σ 54 holoenzyme by scanning force microscopy, *J Mol Biol*, **270** (2): 125-138
- Rivetti, C., Guthold, M., Bustamante, C. (1996). Scanning force microscopy of DNA deposited onto mica: equilibration versus kinetic trapping studied by statistical polymer chain analysis., *J. Mol. Biol.*, **264** (5): 919-932
- Rivetti, C., Walker, C., Bustamante, C. (1998). Polymer chain statistics and conformational analysis of DNA molecules with bends or sections of different flexibility, *J. Mol. Biol.*, **280** (1): 41-59
- Rivetti, C., Codeluppi, S., Dieci, G., Bustamante, C. (2003). Visualizing RNA Extrusion and DNA Wrapping in Transcription Elongation Complexes of Bacterial and Eukaryotic RNA Polymerases, *J Mol Biol*, **326** (5): 1413-1426
- Rivetti C, C. S. (2001). Accurate length determination of DNA molecules visualized by atomic force microscopy: evidence for a partial B- to A-form transition on mica, *Ultramicroscopy*, **87** (1-2): 55-66
- Rosenberg, B., VanCamp, L., Trosko, J. E., Mansour, V. H. (1969). Platinum compounds: a new class of potent antitumour agents, *Nature*, **222** (191): 385-386
- Rossell, J. P., Allen, S., Davies, M. C., Roberts, C. J., Tendler, S. J. B., Williams, P. M. (2003). Electrostatic interactions observed when imaging proteins with the atomic force microscope, *Ultramicroscopy*, **96** (1): 37-46

- Rycyna, R. E., Alderfer, J. L. (1985). UV irradiation of nucleic acids: formation, purification and solution conformational analysis of the '6-4 lesion' of dTpdT, *Nucleic Acids Res*, **13** (16): 5949-5963
- Saenger, W. (1984). Principles of Nucleic Acid Structure, Springer-Verlag
- Sancar, A. (1996). DNA excision repair, *Ann Rev Biochem*, **65**: 43-81
- Sanchez-Sevilla, A., Thimonier, J., Marilley, M., Rocca-Serra, J., Barbet, J. (2002). Accuracy of AFM measurements of the contour length of DNA fragments adsorbed on mica in air and in aqueous buffer, *Ultramicroscopy*, **92** (3-4): 151-158
- Saris, N.-E. L., Mervaala, E., Karppanen, H., Khawaja, J. A., Lewenstam, A. (2000). Magnesium: An update on physiological, clinical and analytical aspects, *Clinica Chimica Acta*, **294** (1-2): 1-26
- Scharffetter-Kochanek, K., Brenneisen, P., Wenk, J., Herrmann, G., Ma, W., Kuhr, L., Meewes, C., Wlaschek, M. (2000). Photoaging of the skin from phenotype to mechanisms, *Experiment Gerontol*, **35** (3): 307-316
- Schellman, J. A., Harvey, S. C. (1995). Static contributions to the persistence length of DNA and dynamic contributions to DNA curvature, *Biophys Chem*, **55** (1-2): 95-114
- Schubert, F., Zettl, H., Hafner, W., Krauss, G., Krausch, G. (2003). Comparative thermodynamic analysis of DNA--protein interactions using surface plasmon resonance and fluorescence correlation spectroscopy, *Biochemistry*, **42** (34): 10288-94
- Schulz, A., Mucke, N., Langowski, J., Rippe, K. (1998). Scanning force microscopy of *Escherichia coli* RNA polymerase: sigma54 holoenzyme complexes with DNA in buffer and in air, *J Mol Biol*, **283** (4): 821-836
- Schwille, P., Oehlenschlaeger, F., Walter, N. G. (1996). Quantitative hybridization kinetics of DNA probes to RNA in solution followed by diffusional fluorescence correlation analysis, *Biochemistry*, **35** (31): 10182-10193
- Schwille, P., Bieschke, J., Oehlenschlaeger, F. (1997a). Kinetic investigations by fluorescence correlation spectroscopy: the analytical and diagnostic potential of diffusion studies, *Biophys Chem*, **66** (2-3): 211-228
- Schwille, P., Meyer-Almes, F. J., Rigler, R. (1997b). Dual-color fluorescence cross-correlation spectroscopy for multicomponent diffusional analysis in solution, *Biophys J*, **72** (4): 1878-1886
- Setlov, R. B., Carrier, W. L. Pyrimidine dimers in ultraviolet-irradiated DNA's, *J Mol Biol.*, (17): 237-254
- Sheridan, S. D., Benham, C. J., Hatfield, G. W. (1999). Inhibition of DNA supercoiling-dependent transcriptional activation by a distant B-DNA to Z-DNA transition, *J Biol Chem*, **274** (12): 8169-8174
- Shi, Q., Thresher, R., Sancar, A., Griffith, J. (1992). Electron microscopic study of (A)BC excinuclease. DNA is sharply bent in the UvrB-DNA complex, *J Mol Biol.*, **226** (2): 425-32
- Shimamoto, N. (1999). One-dimensional diffusion of proteins along DNA. Its biological and chemical significance revealed by single-molecule measurements, *J Biol Chem.*, **274** (22): 15293-15296

- Shlyakhtenko, L. S., Gall, A. A., Weimer, J. J., Hawn, D. D., Lyubchenko, Y. L. (1999). Atomic force microscopy imaging of DNA covalently immobilized on a functionalized mica substrate, *Biophys J*, **77** (1): 568-576
- Sinha, R., Hader, D. (2002). UV-induced DNA damage and repair: a review, *Photochem Photobiol*, **1** (4): 225-36
- Smith, C. A., Taylor, J. S. (1993). Preparation and characterization of a set of deoxyoligonucleotide 49-mers containing site-specific cis-syn, trans-syn-I, (6-4), and Dewar photoproducts of thymidylyl(3'-->5')-thymidine, *J Biol Chem*, **268** (15): 11143-11151
- Smulson, M. E., Pang, D., Jung, M., Dimtchev, A., Chasovskikh, S., Spoonde, A., Simbulan-Rosenthal, C., Rosenthal, D., Yakovlev, A., A. D. (1998). Irreversible binding of poly(ADP)ribose polymerase cleavage product to DNA ends revealed by atomic force microscopy: possible role in apoptosis, *Cancer Res*, **58** (16): 3495-3498
- Soler-Lopez, M., Malinina, L., Liu, J., Huynh-Dinh, T., Subirana, J. A. (1999). Water and Ions in a High Resolution Structure of B-DNA, *J Biol Chem.*, **274** (34): 23683
- Spector, T., Cheatham, T., Kollman, P. (1997). Unrestrained molecules dynamics of photodamaged DNA in aqueous solution, *J Am Chem Soc*, **119**: 7095-7104
- Spivak, G., Leadon, S. A., Vos, J. M., Meade, S., Hanawalt, P. C., Ganesan, A. K. (1988). Enhanced transforming activity of pSV2 plasmids in human cells depends upon the type of damage introduced into the plasmid, *Mutat. Res.*, **193** (2): 97-108
- Srivastava, R. C., Froehlich, J., Eichhorn, G. L. (1978). ???, *Biochimie*, **60**: 879
- Subirana, J. A., Abrescia, N. G. A. (2000). Extra-helical guanine interactions in DNA, *Biophys Chem*, **86** (2-3): 179-189
- Sugasawa, K., Ng, J. M., Masutani, C., Iwai, S., van der Spek, P. J., Eker, A. P., Hanaoka, F., Bootsma, D., Hoeijmakers, J. H. (1998). *Xeroderma pigmentosum* group C protein complex is the initiator of global genome nucleotide excision repair., *Mol Cell*, **2** (2): 223-232
- Sugasawa, K., Okamoto, T., Shimizu, Y., Masutani, C., Iwai, S., Hanaoka, F. (2001). A multistep damage recognition mechanism for global genomic nucleotide excision repair, *Genes Dev*, **15** (5): 507-521
- Sunderman, J., F. William (1983). Nickel carcinogenesis, *Inorg Chim Acta*, **79**: 307-308
- Takahara, P., Rosenzweig, A., Freiderick, C., Lippard, S. J. (1995). Crystal structure of double-stranded DNA containing the major adduct of the anticancer drug cisplatin, *Nature*, **377**: 649-652
- Taylor, J.-S., Garrett, D., Brockie, I., Svoboda, D., Telser, J. (1990a). ¹H NMR assignment and melting temperature study of cis-syn and trans-syn thymine dimer containing duplexes of d(CGTATTATGC).d(GCATAATACG), *Biochemistry*, **29** (37): 8858-8866
- Taylor, W. H., Hagerman, P. J. (1990b). Application of the method of phage T4 DNA ligase-catalyzed ring-closure to the study of DNA structure. II. NaCl-dependence of DNA flexibility and helical repeat, *J Mol Biol*, **212** (2): 363-376
- Thoma, B. S., Vasquez, K. M. (2003). Critical DNA damage recognition functions of XPC-hHR23B and XPA-RPA in nucleotide excision repair, *Mol Carcinog*, **38** (1): 1-13

- Thomson, N. H., Smith, B. L., Almqvist, N., Schmitt, L., Kashlev, M., Kool, E. T., Hansma, P. K. (1999). Oriented, active *Escherichia coli* RNA polymerase: An atomic force microscope study, *Biophys J*, **76** (2): 1024-1033
- Treuner, K., Ramsperger, U., Knippers, R. (1996). Replication protein A induces the unwinding of long double-stranded DNA regions, *J Mol Biol*, **259** (1): 104-112
- Ulyanov, N., James, T. (1995). Statistical analysis of DNA duplex structural features, *Methods Enzymol*, **261**: 90-120
- van Noort, J., Orsini, F., Eker, A., Wyman, C., De Grooth, B., Greve, J. (1999). DNA bending by photolyase in specific and non-specific complexes studied by atomic force microscopy, *Nucleic Acids Res*, **27** (19): 3875-3880
- van Noort, S. J. T., van der Werf, K. O., Eker, A. P. M., Wyman, C., de Grooth, B. G., van Hulst, N. F., Greve, J. (1998). Direct visualization of dynamic protein-DNA interactions with a dedicated atomic force microscope, *Biophys J*, **74** (6): 2840-2849
- Vasquez, K., Christensen, J., Li, L., Finch, R., Glazer, P. (2002). Human XPA and RPA DNA repair proteins participate in specific recognition of triplex-induced helical distortions, *Proc Natl Acad Sci USA*, **99** (9): 5848-5853
- Vassilyev, D., Kashiwagi, T., Mikami, Y., Ariyoshi, M., Iwai, S., Ohtsuka, E., Morikawa, K. (1995). Atomic model of a pyrimidine dimer excision repair enzyme complexed with a DNA substrate: structural basis for damaged DNA recognition, *Cell*, **83** (5): 773-782
- Verhoeven, E. E., Wyman, C., Moolenaar, G., F, Hoeijmakers, J., H, Goosen, N. (2001). Architecture of nucleotide excision repair complexes: DNA is wrapped by UvrB before and after damage recognition., *EMBO J*, **20** (3): 601-611
- Verhoeven, E. E. A., Wyman, C., Moolenaar, G. F., Goosen, N. (2002). The presence of two UvrB subunits in the UvrAB complex ensures damage detection in both DNA strands, *EMBO J*, **21** (15): 4196-4205
- Volbeda, A., Fontecilla-Camps, J. C., Frey, M. (1996). Novel metal sites in protein structures, *Curr Opin Struct Biol*, **6** (6): 804-812
- Volker, M., Mone, M. J., Karmakar, P., Van Hoffen, A., Schul, W., Vermeulen, W., Hoeijmakers, J. H. J., Van Driel, R., Van Zeeland, A. A., Mullenders, L. H. F. (2001). Sequential assembly of the nucleotide excision repair factors *in vivo*, *Mol Cell*, **8** (1): 213-224
- Wagner, P. (1998). Immobilization strategies for biological scanning probe microscopy, *FEBS Lett*, **430** (1-2): 112-115
- Wakasugi, M., Sancar, A. (1999). Order of assembly of human DNA repair excision nuclease, *J Biol Chem*, **274** (26): 18759-18768
- Wang, C.-I., Taylor, J.-S. (1991). Site-specific effect of thymine dimer formation on dA(n).dT(n) tract bending and its biological implications, *Proc Natl Acad Sci U S A*, **88** (20): 9072-9076
- Wang, C.-I., Taylor, J.-S. (1993). The *trans-syn-I* thymine dimer bends DNA by 22 degrees and unwinds DNA by 15 degrees, *Chem Res Toxicol*, **6** (4): 519-523
- Wang, M., Mahrenholz, A., Lee, S.-H. (2000). RPA stabilizes the XPA-damaged DNA complex through protein-protein interaction, *Biochemistry*, **39** (21): 6433-6439
- Watson, J. D., Crick, F. H. C. (1953). Molecular structure of nucleic acids. A structure for deoxyribose nucleic acid, *Nature*, **171**: 737-738

- Wehner, J., Horneck, G. (1995). Effects of vacuum UV and UVC radiation on dry *E. coli* plasmid pUC19 I. Inactivation, lacZ- mutation induction and strand breaks, *Photochem Photobiol*, **28** (1): 77-85
- Weisenhorn, A. L., Hansma, P. K., Albrecht, T. R., Quate, C. F. (1989). Forces in atomic force microscopy in air and water, *Appl Phys Lett*, **54** (26): 2651-2653
- Wirhth, A., Jung, H. (1972). Single-strand breaks induced in DNA by vacuum-ultraviolet radiation, *Photochem Photobiol*, **15** (4): 325-330
- Wojczewski, C., Stolze, K., Engels, E. (1999). Fluorescent oligonucleotides - versatile tools as probes and primers for DNA and RNA analysis, *Synlett*, **10**: 1667-1678
- Wold, M. S. (1997). Replication protein A: A heterotrimeric, single-stranded DNA-binding protein required for eukaryotic DNA metabolism, *Annu Rev Biochem.*, **66**: 61-92
- Wood, R. D. (1997). Nucleotide excision repair in mammalian cells, *J Biol Chem*, **272** (38): 23465-23468
- Wood, R. D. (1999). DNA damage recognition during nucleotide excision repair in mammalian cells, *Biochimie*, **81** (1-2): 39-44
- Wood, R. D., Araujo, S. J., Ariza, R. R., Batty, D. P., Biggerstaff, M., Evans, E., Gaillard, P.-H., Gunz, D., Koberle, B., Kuraoka, I., Moggs, J. G., Sandall, J. K., Shivji, M. K. K. (2000). DNA damage recognition and nucleotide excision repair in mammalian cells, *Cold Spring Harbor Symposia on Quantitative Biology*, **65**: 173-182
- Yang, D., van Boom, S., Reedijk, J., van Boom, J., Wang, A.-J. (1995). Structural analysis of an interstrand cisplatin-cross-linked octamer DNA duplex by NMR analysis, *Biochemistry*, **34**: 12912-12920
- Yang, J., Shao, Z. (1993). Effect of probe force on the resolution of atomic force microscopy of DNA, *Ultramicroscopy*, **50** (2): 157-170
- You, J., Wang, M., Lee, S. (2003). Biochemical analysis of the damage recognition process in nucleotide excision repair, *J Biol Chem.*, **278** (9): 7476-7485
- Zheng, J., Li, Z., Wu, A., Zhou, H. (2003). AFM studies of DNA structures on mica in the presence of alkaline earth metal ions, *Biophys Chem*, **104** (1): 37-43
- Zienolddiny, S., Svendsrud, D. H., Ryberg, D., Mikalsen, A. B., Haugen, A. (2000). Nickel(II) induces microsatellite mutations in human lung cancer cell lines, *Mutat Res*, **452** (1): 91-100
- Zou, L., Elledge, S. J. (2003). Sensing DNA damage through ATRIP recognition of RPA-ssDNA complexes, *Science*, **300** (5625): 1542-1548

DANKSAGUNG

An erste Stelle bedanke ich mich ganz herzlich bei meinem Doktorvater Prof. Georg Krausch. Besonders für sein Vertrauen in mich, eine Biologin aus der Ukraine, die sich zusammen mit Chemikern und Physikern mit AFM beschäftigen sollte. Ich danke für interessante Fragestellungen, inspirierende Besprechungen und wissenschaftliche Freiheit.

Ich bedanke mich bei Armin Knoll, mit dem ich den ersten Frust über AFM Messungen in Wasser geteilt habe. Für seinen Bungee-Aufbau, der mir die tolle Auflösung erlaubt hat. Ich bedanke mich bei ihm ganz herzlich, da er immer für mich da war in der praktischen Arbeitsführung. Außerdem danke ich ihm für seine sorgfältige sprachliche und sachliche Korrektur dieses Manuskripts.

Bedanken möchte ich mich auch bei den ehemaligen und aktuellen Mitgliedern des Arbeitskreises Krausch: mein herzlicher Dank gilt Nicolaus Rehse, Helmut Hänsel und Dr. Hubert Elbs für eine geduldige Einführung ins ‚AFM business‘; Heiko Zettl für den gemeinsamen Kampf gegen die ‚scientific beauty‘ und seine unendliche Programmierarbeit von zahlreichen Fittingroutinen, die speziell an meine Bedürfnissen angepasst werden sollten. Herzlichen Dank gilt Daniel Boehringer und Imelda Oka – die sich mit viel Fleiß mit AFM in Flüssigkeiten auseinander gesetzt haben. Ich bedanke mich bei Priv. Doz. Dr. Robert Magerle für erste Versuche biologische Proben mittels AFM abzubilden. Ich bedanke mich bei Dr. Mark Geoghean für seine hoffnungslosen Versuche mein Englisch zu verbessern. Ich bedanke mich bei meinen weiteren ehemaligen Kollegen: Dr. L. Tsarkova, Dr. Tracy Chun Wang, Dr. Wolfgang. Häfner, Dr. Andrej Voronov, Carmen Kunert, Olena Shafranska, Andriana Horvat, Frank Schubert, Ute Lippert, Kristin Schmidt, Sabine Ludwigs, Jon Bosco, Markus Hund, Gustav Sauer, Chris Cecco, Panteleimon Pan Panagiotou, Mattias Konrad, Markus Gruber und Stefan Höhn für ihre vielseitige Unterstützung meiner täglichen Arbeit.

Ich bedanke mich ganz besonderes bei Sybille Zimmermann – unserer Super-Sekretärin, die sich ständig um die ästhetische und seelische Gemütlichkeit in der PCII gesorgt hat. Besonderen Dank will ich an unsere ehemalige Sekretärin Christiane Theurer ausrichten, die sich viel Mühe gegeben hat meine Promotionsstelle bei Prof. Georg Krausch zu ermöglichen.

Ich bedanke mich ganz herzlich bei Prof. G. Krauss für interessante Fragestellungen und informative Besprechungen sowie eine gute Kooperation während der ich die Möglichkeit hatte mit seinen Arbeitskreismitgliedern zusammenzuarbeiten. Besonders

DANKSAGUNG

hervorheben möchte ich Dr. Thomas Hey, der sich sehr viel Mühe mit der Präparation und Reinigung von biochemischen Substraten gab. Ich bedanke mich bei Dr. G. Lipps für seine tägliche Unterstützung meiner Arbeit im biochemischen Labor sowie für informative Besprechungen. Außerdem will ich mich bei Han Dong und Rasa Beinoraviciute-Kellner für die Synthese von interessanten DNA Sonden bedanken.

Herzlichen Dank an Prof. Diethelm Kleiner, der mir die gemütliche Stadt Bayreuth mit der großen Universität empfohlen hat.

Besonderer Dank gilt meinem Sohn Alexander und meinen Eltern für ihre stetige Unterstützung während der Promotionszeit.

Außerdem bedanke ich mich auch bei der Frauenbeauftragten für die Anschaffung eines Computers, der es mir ermöglicht hat einen Teil der Arbeit zu Hause zu erledigen, sowie bei der Deutschen Forschungsgemeinschaft (Kr1369/11) für die finanzielle Unterstützung.

ERKLÄRUNG

Die vorliegende Arbeit wurde von mir selbstständig verfasst und ich habe dabei keine anderen als die angegebenen Hilfsmittel und Quellen benutzt. Ferner habe ich nicht versucht, anderweitig mit oder ohne Erfolg eine Dissertation einzureichen oder mich der Doktorprüfung zu unterziehen.

Bayreuth, den 18.03.2004

Marina Lysetska